THE EFFECT OF STRAIN RATE ON THE DYNAMIC MECHANICAL BEHAVIOUR OF CONCRETE

A Thesis Submitted to
The Graduate School of Engineering and Sciences of
Izmir Institute of Technology
in Partial Fulfillment of the Requirements for the Degree of

MASTER OF SCIENCE

in Mechanical Engineering

by
Çetin Erkam UYSAL

July 2018
İZMİR

We approve the thesis of **Çetin Erkam UYSAL**

Examining Committee Members:

Prof. Dr. Alper TAŞDEMİRCİ
Department of Mechanical Engineering, İzmir Institute of Technology

---

Assist. Prof. Dr. Selçuk SAATCI
Department of Civil Engineering, İzmir Institute of Technology

---

Assist. Prof. Dr. Levent AYDIN
Department of Mechanical Engineering, İzmir Katip Çelebi University

04 July 2018

Prof. Dr. Alper TAŞDEMİRCİ
Supervisor, Department of
Mechanical Engineering
İzmir Institute of Technology

Prof. Dr. Mustafa GÜDEN
Co-Supervisor, Department of
Mechanical Engineering
İzmir Institute of Technology

Prof. Dr. Metin TANOĞLU
Head of the Department of
Mechanical Engineering

Prof. Dr. Aysun SOFUOĞLU
Dean of the Graduate School of
Engineering and Sciences

ACKNOWLEDGEMENTS

Firstly, I would like to express my sincere gratitude to my supervisor Prof. Dr. Alper TAŞDEMİRCİ for his guidance, endless patience and support during all steps of this study. I am very grateful for being a member of his research team in Dynamic Testing and Modeling Laboratory. I also thank my co-supervisor Prof. Dr. Mustafa GÜDEN for his valued support and comments.

I would also like to thank The Scientific and Technological Research Council of Turkey (TUBITAK) for the financially supporting 115M534 project. Thanks to my project mates Dr. Mehmet Alper ÇANKAYA and Semih Berk SEVEN for their hard work and collaboration.

Thanks to all labmates in DTM; Emine Fulya AKBULUT, Fırat TÜZGEL, Erkan GÜZEL, Mustafa Kemal SARIKAYA, Mesut BAYHAN and Ali Kıvanç TURAN for their great friendship and association.

Furthermore, I must express my very profound gratitude to my family; my mother Nevire UYSAL and my father Mevlüt UYSAL for their patience, endless care, and love, financial and moral support throughout my education life, my brother A. Yasin UYSAL for his support and constant encouragement.

Lastly, I gratefully thank my beloved girlfriend Meltem YALÇIN for her patience, emotional support, and motivational encouragement.

ABSTRACT

THE EFFECT OF STRAIN RATE ON THE DYNAMIC MECHANICAL BEHAVIOUR OF CONCRETE

The fast-growing population of mankind has brought out household needs and working structures that might be subjected to static and dynamic loads. Impact loads and repetitive dynamic loads can produce an overload on the structures in a very short period that causes relentless casualties and unfortunate property losses. The response of the concrete material on strain rate increase is critical. The dynamic characterization of concrete, lack of adequate and consistent study causes disagreement about strain rate sensitivity of concrete, so a consensus has not been reached. In this study, quasi-static ($3.55x10^{-5}$, $3.23x10^{-4}$, and $2.97x10^{-3}$ s^{-1}) and high strain rate (140-250 s^{-1}) tests were conducted and the effect of strain rate on the mechanical behavior of concrete was investigated both experimental and numerical. A modified Split Hopkinson Pressure Bar test setup was used, by using an EPDM (Ethylene Propylene Diene Monomers) rubber pulse shaper, non-oscillatory results and nearly constant strain rate were reached, and premature failure was prevented. Modeling the test setup was conducted in Ls-Dyna and the Holmquist-Johnson Cook material model parameters were found. A good agreement between experimental and numerical results was reached. The strength enhancements of concrete material, while increasing strain rate was noticed. Using both experimental and numerical studies, the total strength increase is due to inertia effect and strain rate sensitivity effects were observed.

ÖZET

BETONUN DİNAMİK MEKANİK DAVRANIŞI ÜZERİNE ŞEKİL DEĞİŞTİRME HIZININ ETKİSİ

İnsanlığın hızlı büyüyen nüfusu, statik ve dinamik yüklere maruz kalabilecek barınak ve çalışma alanı ihtiyaçlarını ortaya çıkardı. Darbe yükleri ve tekrarlayan dinamik yükler, çok kısa bir sürede yapılarda aşırı yükler yaratabilir ve bu da talihsiz kayıplara ve yüklü mal kayıplarına neden olabilir. Beton malzemenin şekil değiştirme hızı artışı üzerine tepkisi kritiktir. Betonun dinamik karakterizasyonu ile ilgili yeterli ve tutarlı çalışmanın olmaması, betonun gerilme oranı hassasiyeti konusunda anlaşmazlıklar olması dolayısıyla ortak bir fikir birliğine ulaşılamamıştır. Bu çalışmada, yarı statik ($3.55x10^{-5}$, $3.23x10^{-4}$, ve $2.97x10^{-3}$ s^{-1}) ve yüksek şekil değiştirme hızları (140-250 s^{-1}) testleri yapılmış ve şekil değiştirme hızının betonun mekanik davranışına etkisi hem deneysel hem de nümerik olarak incelenmiştir. Modifiye edilmiş Split Hopkinson Basınç Çubuğu test düzeneği kullanılmıştır, EPDM (Ethylene Propylene Diene Monomers) kauçuk malzemeden yapılmış, alan gerilme dalgası şekillendirici kullanılarak, gürültüsüz sonuçlar elde edilmiş ve neredeyse sabit şekil değiştirme hızına ulaşılmış ve prematüre kırılma önlenmiştir. Test düzeneğinin modellenmesi Ls-Dyna' da yapılmış olup Holmquist-Johnson Cook malzeme modeli parametreleri bulunmuştur. Deneysel ve nümerik sonuçlar arasında tutarlılık olduğu saptandı. Beton malzemenin, artan şekil değiştirme hızı ile mukavemetinin de arttığı fark edilmiştir. Deneysel ve nümerik çalışmalar kullanılarak, toplam mukavemet artışının hem atalet etkisinden hem de şekil değiştirme hızı hassasiyeti etkisinden kaynaklanmakta ve bunlara duyarlı olduğu gözlemlenmiştir.

TABLE OF CONTENTS

LIST OF FIGURES

LIST OF TABLES

Table **Page**

CHAPTER 1

INTRODUCTION

1.1 Introduction

The need for shelter has always existed since the beginning of mankind. First, people meet their need for housing in places such as caves, rock shelters that are present in nature. Then, simple branches, reeds, and slurry started to be used. The need for a stable settlement makes the pioneer of new forms of housing and the use of stone and wood starts at this point. The rapidly rising population has brought out more household needs, as well as the fact that the construction process is faster and more economical. The use of concrete has gained importance in this period and has been the most used construction material ever since.

Concrete is being used in various types of structures (roads, bridges, buildings, airports, sewers, canals, dams, nuclear power plants, and subways etc.) that might be subjected to static and dynamic loads acting on them in different directions. For instance, the protective shells of arsenals or shelters are expected to survive the impact loading of an incoming projectile. Roads, bridges, and airport runways must withstand repetitive dynamic loads due to heavy vehicles and aircraft takeoff and landing. Natural hazards; flood, earthquakes, tornadoes, etc. also cause dynamic loading on concrete structures. Extreme loads could produce an overload on the structure which is much greater than the design load in a very short period of time. This may result in resistance to carry these loads or cause severe damage and tremendous casualties and property losses. Naturally, an amount of deformation occurs in the effect of the loads on the concrete. The response of concrete to impact and explosive loading are critical for the effective protection of civilian buildings, defensive structures (shelters, arsenals, kalekol structures, etc.), and destruction of military targets, Figure 1.1. The behavior of concrete under high strain rate loads (impact or blast) is an essential for the design and analysis of these structures.

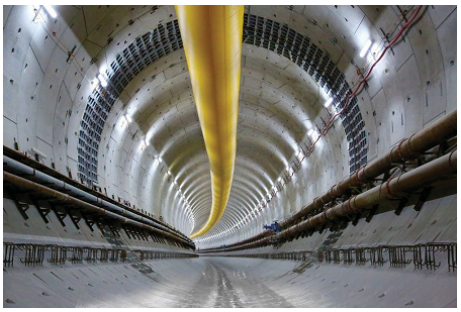

(a)

(b)

(c)

Figure 1.1. a) Avrasya Tunnel (Source: www.ym.com.tr), b) Kalekol (Source: hurriyetdailynews.com), c) Syria Border Wall (Source: www.deezen.com)

1.2 Literature Review

It has become important to analyze this type of loads that the concrete element may encounter during its lifetime. Since concrete shows rate-dependent behavior that its mechanical properties could change depending on strain rate, to observe strain rate effects on the dynamic strength of concrete became a crucial manner.

From Abrams (1917) until today different type of test methods, specimen geometries, strain measurement techniques have been used to test concrete specimens can be seen in Table 1.1. Lever, pneumatic, hydraulic pistons, drop hammer, weight, impact, and SHPB techniques have been used to observe the mechanical behavior of concrete specimens. A critical review was published, by Bischoff & Perry (1991) where a large number of experimental tests were summarized that the compressive behavior of concrete at high strain rates was examined and it is generally accepted that the dynamic compressive strength of the concrete material increases with strain rate, Figure 1.2.

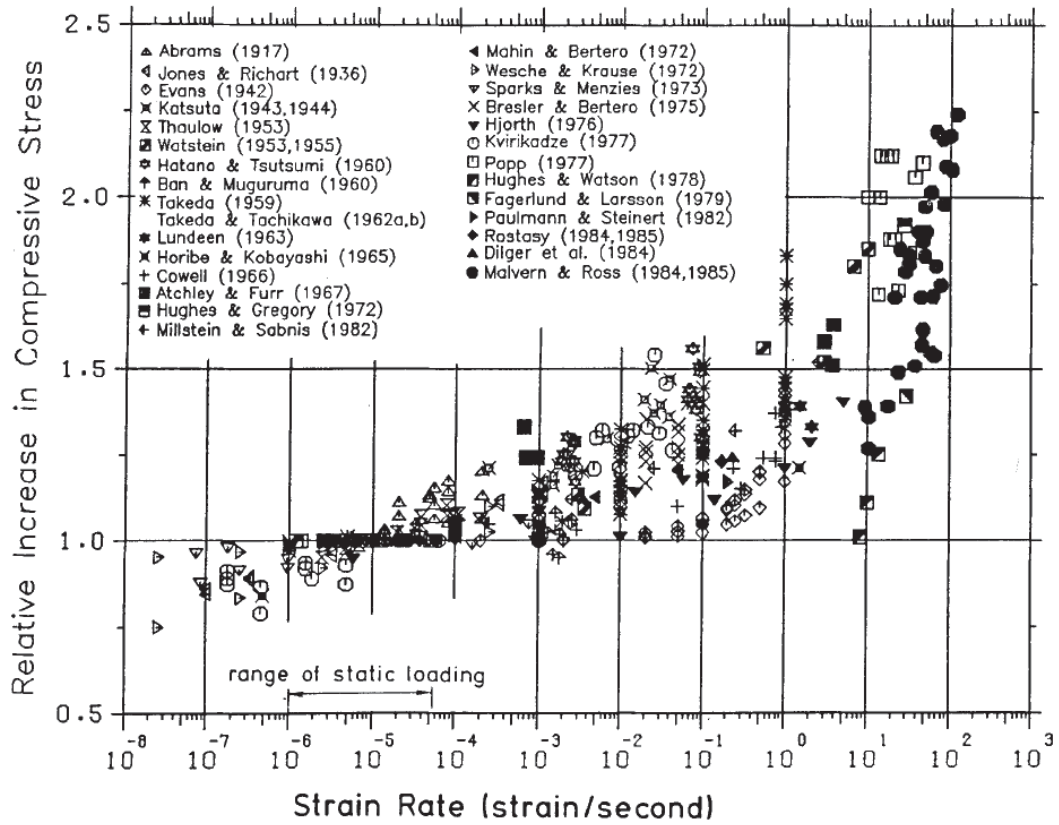

Figure 1.2. Increase in Compressive Stress-Strain Rate from (Bischoff & Perry, 1991)

Dynamic increase factor (DIF) is an important parameter to measure the strain rate effect on the strength of concrete materials and defined as the ratio of the dynamic strength to the quasi-static strength in uniaxial compression. European CEB (European Committee for Concrete) proposed DIF formulas for concrete. Comparative studies on the dynamic strength of concrete should be based on consistent experimental results. An effectual test method should be followed to minimize experimental uncertainties. To study the dynamic behavior of concrete at high strain rates, Split Hopkinson Pressure Bar (SHPB) is a very popular experimental approach. The strain rate sensitivity of concrete has been under investigation for several decades. There is still little agreement on some issues about mechanical behavior of concrete. How should rate sensitivity measurement (in terms of elastic modulus, strength, or strain at maximum stress) be? Does compressive strength was influenced by strain rate or not? Does the strain at maximum stress (increase, decrease, or constant) change because of rate sensitivity behavior?

Malvern, et al. (1985) investigated the effect of aggregate size and type to compression behavior of the concrete at strain rates between 10^0 - 10^2 s^{-1}. Four types of aggregate were selected, three of them have maximum 12.7 mm diameter, and one has a

maximum 9.5 mm diameter size. Studied concretes have w/c (water to cement) ratios varies in 0.24-0.27 and were specified as 96.5 MPa high strength concrete based on a static compression test. Specimen length to diameter ratio (L/D) 1 was selected with a 76.2 mm diameter. In SHPB setup, steel bars were used; 76.2 cm striker, 304.8 cm incident and transmitter bar with a diameter of 76.2 mm. Specimens deformed at a nearly constant strain rate. 2 – 4 times increase in dynamic compressive strength was observed.

Table 1.1. The main pioneer studies that examined the behavior of concrete under various strain rate until 1989, from (Bischoff & Perry, 1991)

Year	**Reference**	**Type of Test**	**Specimen Size (mm)**	**Strain Rate (s^{-1})**
1917	Abrams	Lever	ϕ152 x 305	2×10^{-4}
1959	Takeda and Tachikawa	Pneumatic, hydraulic	ϕ150 x 300	1
1967	Atchley and Furr	Hydraulic, drop test	ϕ152 x 305	3.5
1972	Hughes and Gregory	Drop hammer	244 x 102 x 102	29
1975	Bresler and Bertero	Hydraulic	ϕ152 x 305	0.1
1978	Hughes and Watson	Drop Hammer		13.9
1984	Dilger et al.	Hydraulic	152 x 152 x 610	0.23
1985	Ahmed and Shah	Hydraulic	ϕ76 x 305	3×10^{-2}
1985	Malvern et al.	SHPB	ϕ76 x 76 ϕ76 x 66	59 - 118
1987	Jawed et al.	Hydraulic and SHPB	ϕ6.35 x 9.5 ϕ12.7 x 19.1 ϕ19.05 x 28.6	10^3
1989	Gran et al.	Explosive gas	ϕ150 x 300	0.5 - 10
1989	Ross et al.	SHPB	ϕ51 x 51	20 - 190

Ross et al. (1989) examined the effects of strain rate on the compressive strength of concrete. They used steel bars with a diameter of 51 mm and with 65.2, 365.8, 335.2 cm long striker, incident and transmitter bar on SHPB setup respectively. L/D=1 was selected with w/c ratio was 0.53 and maximum aggregate size was 9.65 mm. Strain rate between 10-10^2 applied to the 60 MPa static compressive strength of concrete specimens and shows rate sensitive behavior and strength increased almost 2 times, Figure 1.3.

Tang et al. (1992) studied two types of high-strength concrete. They conducted 67 tests and chose specimens L/D ratios as 0.5, 1 in SHPB setup. They used 76.2 mm diameter steel bars to test 76.2 mm diameter concrete specimens. Axial and transverse strain values were gathered from strain gages from specimen interface. The dynamic compressive strengths of concrete were reached almost 2 times bigger value of their static compressive strengths at strain rates of 200 s^{-1}.

Tedesco et al. (1998) conducted direct compression and split-tensile tests at quasi-static and dynamic rates from 10^{-7} to 10^3. Dynamic tests were conducted on SHPB setup and 51 mm diameter specimens with length to diameter 1 was selected. It was decided that the samples had a maximum aggregate size of 4 mm. A statistical analysis was performed to obtain strain rate dependency by 60 direct compression and 70 split stress tests. Strain rate dependent constitutive equations were established to modify the quasi-static concrete material model, which was a hypo-elastic model, based on a uniaxial stress-strain relation, Figure 1.3.

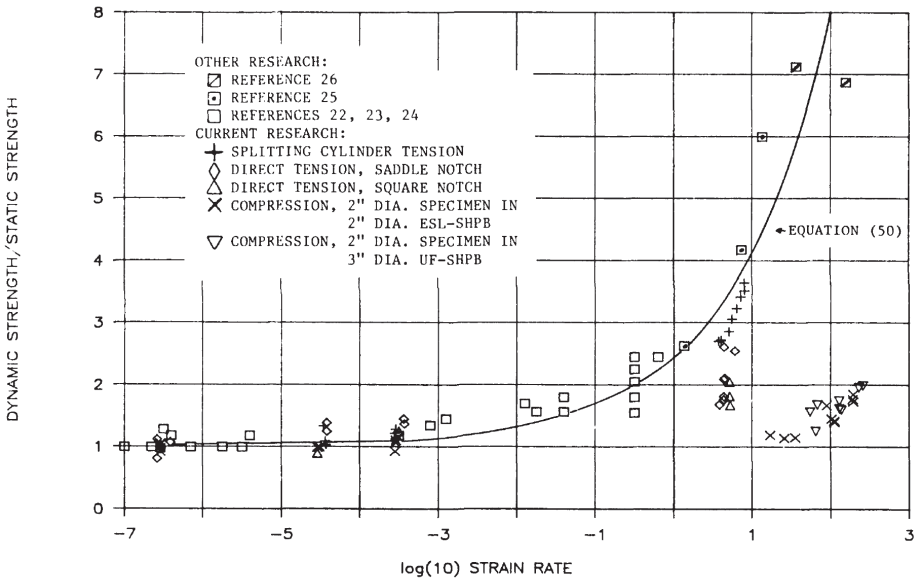

Figure 1.3. Strength Ratio Versus Log (10) of strain rate for tensile and compressive tests of concrete specimens. (C. Allen Ross, 1989)

Gary et al. (1998) made a detailed study by controlling lateral confinement pressures on SHPB setup to study evaluation of radial and lateral pressure effects on both experimental and modeling approach at strain rates between 10-100 s^{-1}. They used a specific device, put the concrete specimen in a cylindrical pressure cell and applied various lateral pressures between 10-50 MPa. 40 mm diameter pressure bars were used and same diameter compressive strength of 65 MPa concrete specimen was tested. Non-constant strain rate was observed at dynamic tests. They created a model which designates behavior of concrete when the damage occurred, allowed inertia and strain rate effects were taken into account.

Grote et al. (2001) examined strain rate dependence of concrete and mortar materials response and high level of hydrostatic pressure cause to change the material at highly dynamic conditions. They focused that how load capacities of material affected by microstructural heterogeneity, loading rate, and hydrostatic pressure. SHPB and plate impact tests were conducted at strain rates between 250 – 1700 s^{-1} with no confining pressure and strain rate 10^4 s^{-1} with confining pressure 1 – 1.5 GPa, respectively. Cylindrical specimens have L/D ratios between 0.31 and 1.55 have tested and no size effect was observed. Almost 3.5 times the quasi-static strength was observed at 1500 s^{-1}. Since different deformation and failure mechanisms in concrete under quasi-static and impact loading, they found out that crack initiation and growth depend the aggregate and mortar within the concrete will affect strength.

X. Chen et al. (2013) studied paste, mortar and concrete specimens to examine the dynamic compressive behavior of materials. 110 cylindrical specimens have L/D ratio 0.5 were tested at high strain rates. Strain rate sensitivity of those materials in terms of stress-strain curves as a function of strain rate, the dynamic increase factor (DIF), elastic modulus, compressive strength, critical strain value, and failure mode were investigated. The compressive strength, critical strain, and elastic modulus increased with increased strain rate, Figure 1.5. Dynamic compressive strength, elastic modulus, and critical strain under dynamic loads (X. Chen et al. 2013). Compressive strength was affected by the strain rate more than elastic modulus and critical strain.

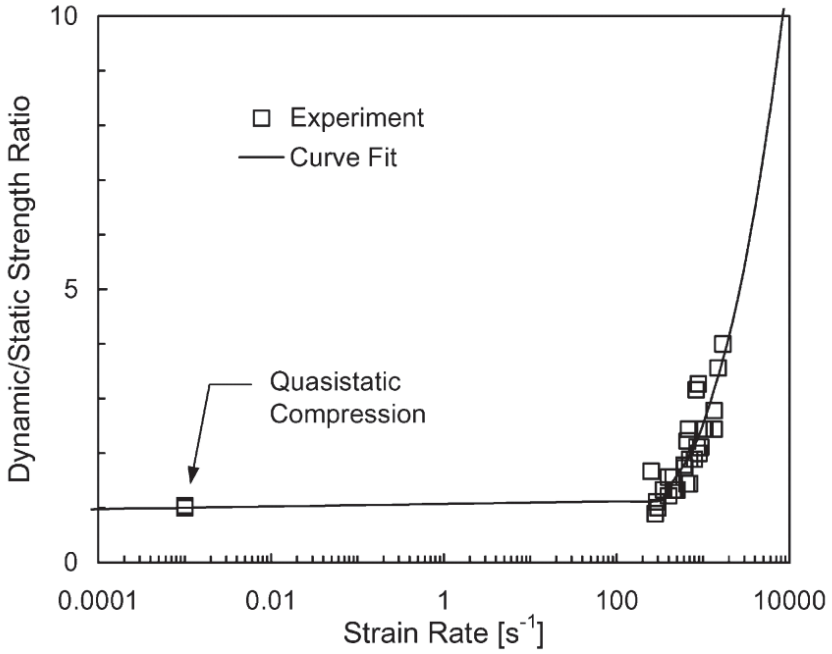

Figure 1.4. Strain-rate dependence of the strength of mortar (Grote et al. 2001)

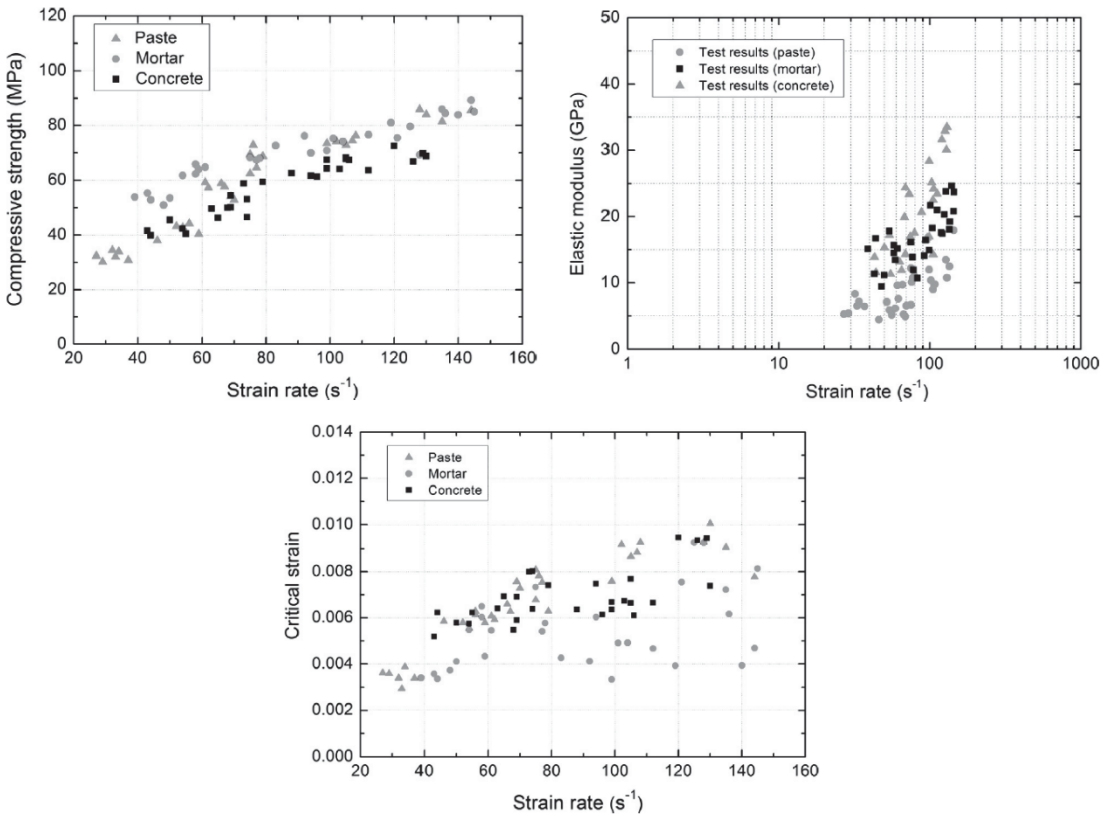

Figure 1.5. Dynamic compressive strength, elastic modulus, and critical strain under dynamic loads (X. Chen et al. 2013)

In SHPB, the is free to move in radial direction that stress waver in the bar is two dimensional naturally. Considering axial quantities, it is considered as approximately

one-dimensional. Due to one dimensional compressive propogation along the bar, the specimen is moved forward that axial kinematic energy is attained, and because of Poisson's effect, there are also some radial kinematic energy is formed. The material acceleration in the radial directions in turn causes inertia-induced stress in the axial direction. (W. W. Chen & Song, 2010)

Semi-infinite cylinder bars show vibrational behavior, elastic wave propagation along this pressure bars have a dispersive nature. Wave dispersions, tend to make waves rise steeply, also cause to oscillations in waves and this may lead to unclear, masked, and/or inaccurate strain and stress curves. Since a valid SHPB test requires a uniform stress distribution along the specimen, to minimize axial and radial inertia effects, the rise time of the incident wave should increase. Rectangular, trapezoidal shaped pulse can be transformed to ramp or half-sinusoidal shape pulse with different methods. Striker bar geometry variations were investigated by Christensen et al. (1972), Frantz et al. (2014), Li et al. (2000), Zhao et al. (2005).

Christensen et al. (1972) made high strain rate tests on nugget sandstone specimens at strain rates 10^2 - 10^3. They used various projectile configurations; conical, cylinder, and combination of truncated-cone and cylinder with the small end of the cone is the impact end to change loading type of incident stress wave. By using conical type projectiles, they achieved to spread-out the incident stress wave and improve the accuracy in the early portion of the stress-strain curve.

Frantz et al. (2014) investigated the wave shaping technique by changing the geometry of the striker bar. The striker bar with a large radius on the impact end can change the rise time of the incident wave. It was emphasized that rise time critically affects the test results. It is suggested that a slow rise minimizes wave dispersions, obtains more uniform strain rate and these lead to reliable measurements.

Li et al. (2000) tested three types of rock: granite, sandstone, and limestone with SHPB apparatus. Since rock and concrete like materials nonhomogeneous and brittle nature, they tested bigger diameter of bars, and this leads to dispersion along the bars. They found out that most effective way of reducing or eliminating the oscillations is to change the shape of the incident wave. By using tapered striker bar, half-sine waveform was attained. Changing the shape of the incident pulse, oscillation was eliminated and more stable strain rate along the loading was obtained as in Figure 1.6.

Zhao et al. (2005) investigated the geometry of striker models by using finite element method, then confirmed research by producing 2 types of non-uniform striker

bar. Since they used large diameter bars to test concrete specimen at strain rates about 10 – 10^2, it was a challenge to obtain stress uniformity in the specimen and to avoid the dispersive effects. Tapered striker bar produced prolonged rise duration of the incident wave. They obtain smoother (incident, reflected, transmitter) waves, constant strain rate, and achieved a reasonably uniform stress in the specimen.

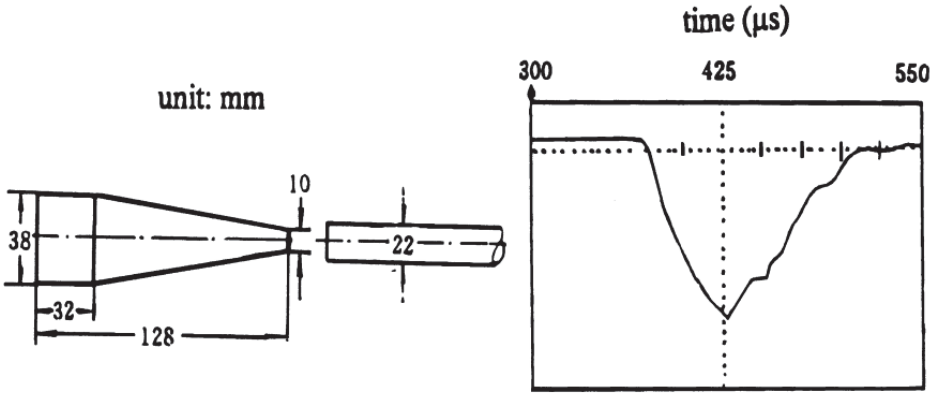

Figure 1.6. Shape and size of strike bar and measured stress waveform (Li et al. 2000)

Some authors used pulse shaper rod or extra specimen; Ellwood et al. (1982), Parry et al. (1995), Gerlach et al. (2011).

Ellwood et al. (1982) added a preloading bar and an extra dummy specimen as a pulse shaper. Ductile materials; aluminum, brass, copper, lead, stainless steel were tested at 100 – 3000 s^{-1} strain rates. They found out that constant strain rate can be attained at high rates, so precise test could be conducted for strain rate sensitive materials.

Gerlach et al. (2011) applied a new method by using a geometrically shaped rod in Split Hopkinson Tension Bar (SHTB) setup. They tested brittle polymeric materials by using this reusable pulse shaper. Authors successfully increased the rise time and reduced wave dispersions.

The most common method is to put a small thin disc (rubber, copper, brass, etc.) between striker and incident bar; Zheng et al. (1999), Frew et al. (2002), W. Li et al. (2009), X. Chen et al. (2013), Su et al. (2014), Yang et al. (2015), Shemirani et al. (2016), Lv et al. (2017).

Zheng et al. (1999), conducted high strain rate tests on the concrete specimen. They inserted 4 mm carton between striker and incident bar to modify stress pulse. They attained triangular shape wave and eliminated dispersion effects.

Frew et al. (2002), performed a research on pulse shaping technique for testing brittle materials. They inserted a thin disk of annealed or hard C11000 copper on impact face of the incident bar. Plastically deformed copper pulse shaper led to half-sinusoidal incident stress pulse. Varying the geometry of the pulse shaper disk, striking velocity and length of the striker bar, dynamic stress equilibrium in the sample and nearly constant strain rate over the test duration were achieved.

X. Chen et al. (2013), studied cement-based materials: cement, mortar, and concrete at high strain rates. Use of thin copper disk as a pulse shaper, they increased rise 3 times and altered rectangular wave into a triangular wave. They achieved to filter out high-frequency components of stress waves and maintain stress equilibrium.

Xia (2013) used different materials as a pulse shaper. A wide variety of incident pulses can be produced by varying the geometry and material of the pulse shaper (rubber, copper, eraser etc.), Figure 1.7. His purpose was to achieve constant strain rate during loading and maintain force equilibrium on the specimen.

Shemirani et al., (2016) conducted both experimental and numerical studies to choose proper pulse shaper dimension in SHPB for the concrete specimen. Rise time altered, and various incident pulses were generated by changing pulse shaper dimensions and striker bar velocity. Constant strain rate condition, minimum dispersion effect, and stress equilibrium in the specimen were obtained by using relatively small diameter and a thin pulse shaper.

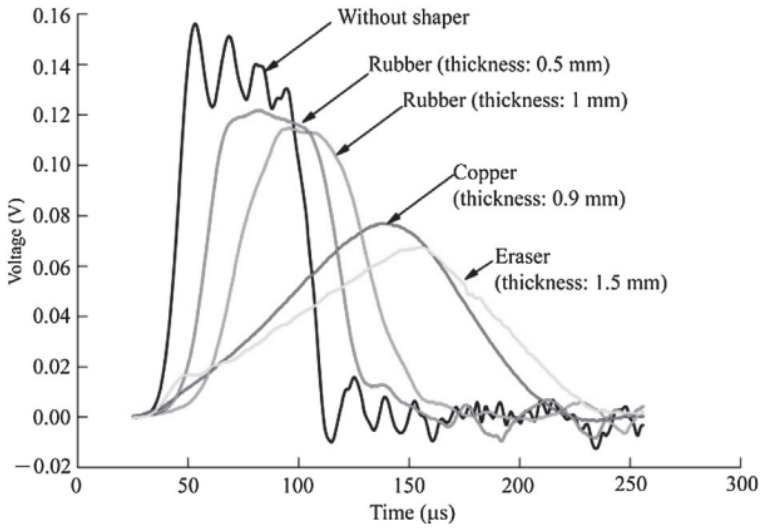

Figure 1.7. Different loading pulses produced by pulse shaping with different materials (Xia, 2013)

1.2.1 SHPB Testing on Brittle Material

As mentioned below, there are some pre-requirements for valid SHPB experiment; stress in the specimen should be in dynamic equilibrium, the specimen should deform homogeneously, and at a constant strain rate. Stress concentrations need to be minimum in both the specimen and bars. Bar end faces must be flat and parallel and remain elastic. To study the dynamic mechanical behavior of ductile materials as metals, these conditions of SHPB testing can be satisfied. When the specimen is a brittle material, there are some challenges in using the SHPB technique to determine material properties; premature failure from non-equilibrated loading and stress concentration, maintaining constant strain rate during testing, and premature failure from early damage accumulation because of short rise time. Accurate measurement of small strains, effective and repeated experiments to get statistical behavior are also hard to satisfy. While testing a ceramic specimen it is also difficult to maintain that bar end faces remain flat and parallel, wave dispersions are unavoidable because of large diameter bar diameter. Accomplishing these conditions to produce valid experimental results, some conditions need to be carefully checked. As a milestone in the high strain rate testing of ceramics, Subhash & Ravichandran, (2000) had undertaken an important study. Considering most of the ceramics shows only elastic strain to failure and the fundamental limitations of the traditional SHPB technique for testing ceramics and the modifications in design and test procedure are discussed in their detailed research. There were some operational principles about traditional Split-Hopkinson Pressure Bar; the duration of the pulse should be almost similar value to the round-trip travel time of the longitudinal wave in the striker bar and the specimen should be chosen to have a lower impedance which means lower density, wave velocity, area of cross-section than the bar material. Some assumptions were made based on a one-dimensional wave analysis.

1. The specimen is under a uniform and uniaxial state of stress during deformation.
2. During the deformation of the specimen, incident and transmitter bars remain elastic during the experiment and end surfaces of the bars remain flat and parallel.
3. As an incident, reflected and transmitter pulses travel along the bar, they undergo minimal dispersion.
4. Because of measuring strain on the surface of the incident and transmitter bars, the stress distribution across the cross-section of the bars is fairly uniform.

While testing metals, it is easy to satisfy these assumptions. But ceramics exhibit different behavior and reveal no more than 1-2 % strains before fracture. To obtain accurate and reliable stress and strain measurements, proper modifications should be made at the testing procedure. In the case of first assumption stress equilibrium in the entire specimen, by choosing duration time of the incident pulse should be longer than the travel time of the longitudinal wave in the specimen that sufficient wave reflections may occur within the specimen. But in the case of ceramics, the specimen can reach the failure before sufficient reflections that stress equilibrium in the specimen was established. The fracture strength data to be valid, it should take at least four transit time to reach stress difference 5% between two end surfaces of the specimen that it is assumed reasonable. While ensuring the second assumption during deformation of the metallic specimen, it is common to use a high strength steel, maraging steel. Because stress levels of ceramics can exceed to the elastic limits of bar material and ceramics are harder than metal, the second assumption might be violating the case that end surfaces of the elastic bars can be exposed to indentation. This cause non-flat and parallel end surfaces elastic bars that stress concentrations, nonhomogeneous deformations, and no uniaxial stress state in the specimen. By sandwiching the specimen between two identical high-strength inserts as seen in Figure 1.8, and placing the whole assembly into the setup, the requirement of impedance matching of bar material and insert material is essential not to change the incident, reflected and transmitter stress waves characteristics that might cause misinterpretation of strain measurement.

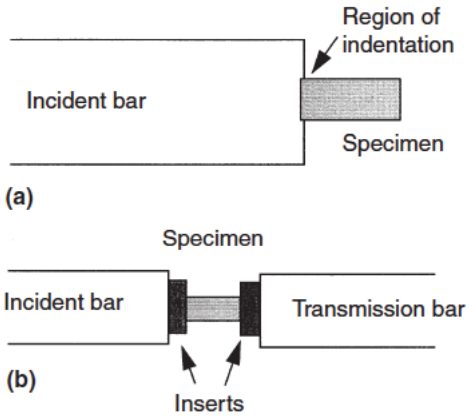

Figure 1.8. a) Shows indentation of bar material, b) Sandwiched specimen between two inserts (Subhash & Ravichandran, 2000)

In the case of third assumption, since the ceramic specimen's deformation is not measured on the specimen itself and using strain gages on the incident and transmitter bar

surfaces at some distance and that might lead to dispersion effects on the propagating pulse, the stress (from transmitter bar and wave) & strain (from incident bar and reflected wave) results might not be true response of the specimen. The amplitude and duration of the pulse changes by the time when it reaches strain gage points that to minimize the dispersion, pulse duration should at least be 10 times larger than the transit time of the longitudinal wave across the diameter of the bar. While the measurement of stress waves gathered from strain gages mounted on the surface of the incident and transmitter bars, to ensure forth assumption, measurement on the surface represents the stress distribution across the cross-section of the steel bars at any instant. The strain gage measurements on the surface are inconsequential if the strain measurement does not represent inside of the bars as seen in Figure 1.9.

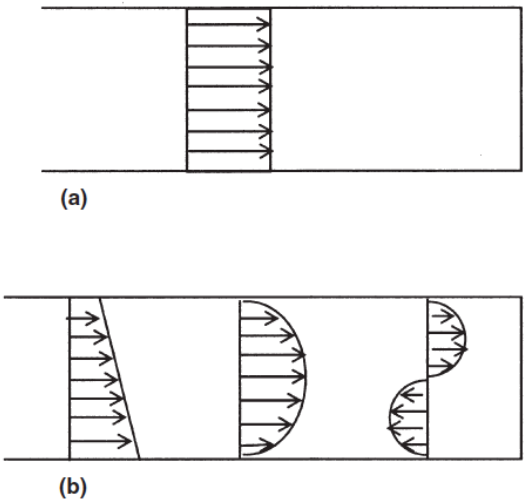

Figure 1.9. a) Uniform b) Nonuniform distribution of stress wave at cross-section of the bars (Subhash & Ravichandran, 2000)

In the SHPB setup, if planar impact between striker and incident bars ensured by alignment of the bars or time window of the incident stress pulse is dispersion eliminated, strain gage measurements from the surface of the bars are representative. Traditionally, a rectangular shaped stress pulse is created in the incident bar by impacting striker bar planar through the incident bar. In the case of metallic specimens, because metals exposed to large plastic strains and rectangular shaped loading pulse imposes a nominally uniform strain rate during the plastic deformation of the metallic materials, rectangular shaped waveform is ideal for metals. In the case of a ceramic specimen, using a rectangular shaped stress pulse is not appropriate. The total energy contained from rectangular pulse is too large for ceramics which experience only elastic strain before failure. Steep stress

increase during the rectangular pulse leads an excessive fragmentation of specimen with nonprobability of recovery of the intact but microcracked specimen. Slopes of the loading of the incident pulse and stress-strain are different because sudden increase imposes a nonuniform strain rate during the elastic deformation of the ceramic specimen. By changing the slope of the incident pulse and matches the elastic response of ceramic specimen is endorsed that pulse shaping allows controlled damage in a ceramic specimen at a constant strain rate because the total energy contained from the ramp pulse over the fracture strength of ceramic is much smaller than the rectangular pulse in the same duration. Subhash & Ravichandran (2000) used a thin metallic disk to generate ramp pulse and by changing the material of the disk, or and velocity and length of the bar they had controlled the rise and fall times of the incident stress pulses.

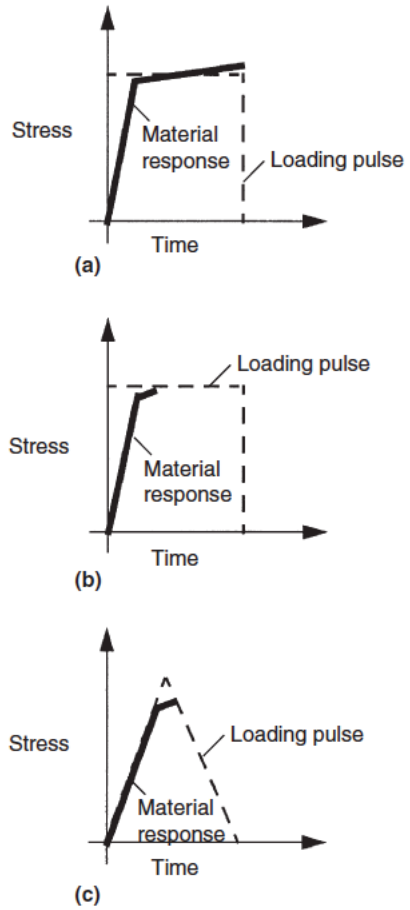

Figure 1.10. Effects of incident pulse shaping on the stress-strain responses. a) Rectangular shaped stress pulse on a metallic specimen. b) Rectangular shaped stress pulse on a ceramic brittle material. c) Ramp-shaped stress pulse on the brittle material. (Subhash & Ravichandran, 2000)

There are some challenges that are listed in using SHPB to determine material properties of the brittle material listed below;

- Premature failure from non-equilibrated loading.
- Maintaining constant strain rate during testing
- Premature failure from early damage accumulation because of short rise time
- Premature failure from stress concentration
- Accurate measurement of small strains
- Repeated experiments to get statistical behavior and the effect of flows
- Effective and controllable methods of dynamic confinement.
- Bar end faces remain flat and parallel.
- Wave dispersions unavoidable because of large bar diameter.

These are especially critical for brittle material testing;

- Pulse Shaping Techniques
- End Friction Effects
- Inertia Effects
- Dispersion Effects

1.3 Objective and Scope of Study

In today's increasingly cheaper housing needs, and in the present chaotic environment of the Middle East, the need for safe accommodation further increases the importance of concrete. In the present case, the mechanical properties of the concrete material become more important, and the work done in this area is even more remarkable. Numerous field studies have been carried out on the concrete material, but it has been observed that the behavior of concrete under dynamic loads is not sufficient. In this study, the strength of concrete under dynamic loads was examined and it was decided to perform this high strain rate tests with Split Hopkinson Pressure Bar Setup. So, an experimental and numerical research was conducted to study the dynamic mechanical behavior of concrete. For this object, firstly concrete material is produced. Then, static and dynamic tests were accomplished to construct finite element model. Finally, numerical studies were performed to validate model and further works studied by using finite element software LS-DYNA. All experimental and numerical studies were conducted at Dynamic Testing and Modelling Laboratory at Izmir Institute of Technology.

CHAPTER 2

MATERIAL AND EXPERIMENTAL STUDY

2.1 Introduction

In this chapter, properties of the concrete material and its manufacturing progress is explained. Then, experimental details, setups, and methodology are introduced. Material model and characterization of concrete are described, lastly.

2.2 Material Identification and Sample Production

"Concrete" is a building material obtained by mixing aggregate, cement, water and, if necessary, some additives. All properties of the concrete are influenced by the features of the cement, aggregate, water, and additives used to form the concrete mixture and the proportions in which they are included in the mixture. Hardened concrete has a high compressive strength. The compressive strength of concrete produced by appropriate materials and suitable methods is close to the compressive strengths of some natural stones. Concrete is a material with a low tensile strength which has heterogeneous and brittle nature. Approximately 75% of the concrete volume is formed by aggregate, which has important contributions to the mechanical properties of concrete. The high strength of the aggregate contributes to the high strength of the concrete. Aggregates; gradation, maximum grain size, water absorption capacity, unit weight, specific gravity properties will affect the concrete properties to be produced. The ratio of "water/cement" used in concrete is also a factor that directly affects the concrete strength. As the water to cement ratio increases, lower strength concretes are obtained. In order to start the calculation of the mixing ratios of the materials forming the concrete, it is necessary to know what quality of concrete is required first (Erdogan, 2013).

In order to complete the experimental static and dynamic studies, a mix design of 130 liters of concrete was calculated. ACI 211.1 code was followed to calculate the concrete mix ingredient proportions. In this context; mixed aggregate size & amount, mixing water weight & air volume, water/cement ratio, cement weight, slump value

should be determined. Since relatively small prism steel molds were used, 150 – 175 mm slump value was selected. 4.75 mm aggregate size is selected that it is suitable for SHPB tests, valid for 1/10 ratio of aggregate size to specimen diameter and represent the concrete material behavior. The concrete strength targeted by tables from ACI 211.1 standards was taken into account and the water/cement ratio was determined as 0.40. The required amount of cement was also determined by this ratio. The prepared mixture is poured into prismatic steel molds. In the static and dynamic characterization tests cylindrical specimens of 45 mm length and 39.5 mm diameter were used, Figure 2.1. Cylindrical specimens were cut off from the prismatic concrete with dimensions of 220 mm x 45 mm x 45 mm with a core drill, Figure 2.1.

(a) (b) (c)

Figure 2.1. (a) Core Drill, (b) Concrete Prism, (c) Concrete Specimen

Front and back surfaces of the concrete samples were polished and both surfaces were made parallel with each other to prevent non-uniform stress distribution and premature fracture.

2.3 Quasi-Static Testing

Quasi-static tests were performed using Shimadzu AG-X universal testing machine at Dynamic Testing and Modelling Laboratory, Izmir Institute of Technology. A testing machine with the capacity of 300 kN was used to made uniaxial compression tests on the concrete specimen, Figure 2.2. Three different strain rates were selected for quasi-static tests and these were 10^{-2}, 10^{-3}, and 10^{-4}. The specimen was located between upper and lower rigid plates that lower plate is fixed, and upper plate moves uniaxial. In static tests, the strain is measured by two different methods. The first one is the video extensometer and the second one is strain gauges glued onto the sample. Due to the brittle

nature of the concrete material, the fracture strain value is quite small. Because of this small strain values, the displacement values of the cross-head measurement cannot be used in strain measurements (machine compliance). Strain rate can be controlled by changing cross head speed in static tests. Desired strain rate will lead to a determination of cross-head velocity, Equation (2.1).

$$v_{cr} = \dot{\varepsilon} \text{ x L} \tag{2.1}$$

Figure 2.2. Shimadzu AG-X Universal Test Machine

In the above equation v_{cr} represents cross head velocity, $\dot{\varepsilon}$ and L represent strain rate and specimen length, respectively. 40 quasi-static tests were performed in this section.

In addition, strain gages are glued on the concrete specimen surface in different orientations for additional measurements directly from the surface of the specimen and additional tests were performed to determine the strain history and Poisson's ratio of the shape change on the sample. For this purpose, three pieces of vertical and two pieces of

horizontal, a total of five strain gage are placed on the lateral surface of the concrete sample as shown in Figure 2.3

Figure 2.3. Strain Gage Glued Concrete Specimen

2.4 High Strain Rate Testing

High strain rate compression tests were performed with compression type of Split Hopkinson Pressure Bar (SHPB) apparatus at Dynamic Testing and Modelling Laboratory, Izmir Institute of Technology.

2.4.1 Background: Split Hopkinson Pressure Bar (SHPB)

The Hopkinson bar experimental technique performed by John Hopkinson in 1872 was developed from the stress wave experiments in the iron wire. His son, Bertram. Hopkinson in 1914, invented a pressure bar to measure stress in a long thin bar. These stresses produced by the impact of the bullets or the detonation of explosives at one end of the bar. Davies in 1948, developed a measurement technique by using electrical condensers instead of short bars to monitor axial and radial strain existing in the pressure

bar. Kolsky made an important modification by adding a pressure bar to the original Hopkinson apparatus in 1949. He sandwiched a specimen between two bars (incident and transmitter) and obtained dynamic strain-stress response of the material. Split-bar system has been widely used and has been referred as Kolsky bar as well. Krafft et al. (1954) firstly adopted strain gage technique on the pressure bars to measure strain. He also used a projectile (striker bar) to generate stress waves and to make repeatable experiments. Lindholm (1964) presented an updated version of Kolsky bar system for valid dynamic characterization that combines previous modifications. This design became popular among laboratories around the world. Follansbee (1995), (Nemat-Nasser et al. (1991), Gray (2000), Subhash and Ravichandran (2000), Gama et al. (2004) made modifications along instrumentation to gain more accurate data and improved SHPB setup.

2.4.2 SHPB Theory and Apparatus

Split Hopkinson Pressure Bar (SHPB) apparatus consist of a gas gun, three elastic pressure bars (striker, incident, and transmitter) and a specimen that two bars (incident, transmitter) sandwiched the specimen between them, Figure 2.4. The gas gun filled up with a predetermined pressure. The striker bar velocity thereby strain rate is proportional to the pressurized gas. Sudden gas release into the barrel from gas gun leads the striker bar to attain an initial motion. Striker bar with a certain velocity hits the incident bar, a compressive stress wave is produced at the impact end of the incident bar. Then, stress waves move along the incident bar, which is called “incident wave”. When this wave reaches incident bar/specimen interface, the wave partially transmitted into the specimen, then transmitter bar as a compressive wave, called “transmitter wave”, while the rest partially reflected back to incident bar as a tensile wave, called “reflected wave” according to the impedance mismatch between specimen and bar material.

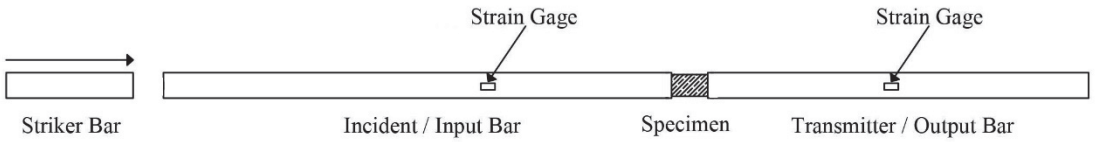

Figure 2.4. A typical configuration of SHBP

The generated wave propagates through incident and transmitter bars and incident, reflected, and transmitter waves are measured by strain gages bonded on the surface of bars as strain pulses. 2 set gages are used for each bar. Strain gages have full bridge connection that acquired voltage signals recorded and displayed via a 4-channel digital oscilloscope which is connected to the strain gage conditioner.

SHPB principles are based on one-dimensional elastic wave propagation in long bars. The magnitude of stress or strain amplitude of the incident pulse, σ or ε created along the incident bar is direct functions of (ρ_B) mass density of striker bar, (C_B) elastic wave speed of the striker bar, and (V_{SB}) velocity of striker bar, Equation (2.2), Equation (2.3). Striker bar usually has the same material and cross section as incident and transmitter bars. Loading duration of incident stress wave, T in Figure 2.5. is produced in a SHPB experiment is determined by (L_{SB}) length of striker bar and elastic wave speed, Equation (2.4), where E is the elastic modulus of the striker bar material. Elastic wave speed can calculate by Equation (2.5). Varying the length and impact velocity of the striker bar, different incident stress waves, their magnitude or loading period, σ or T can be attained to reach targeted strain rate, Figure 2.5.

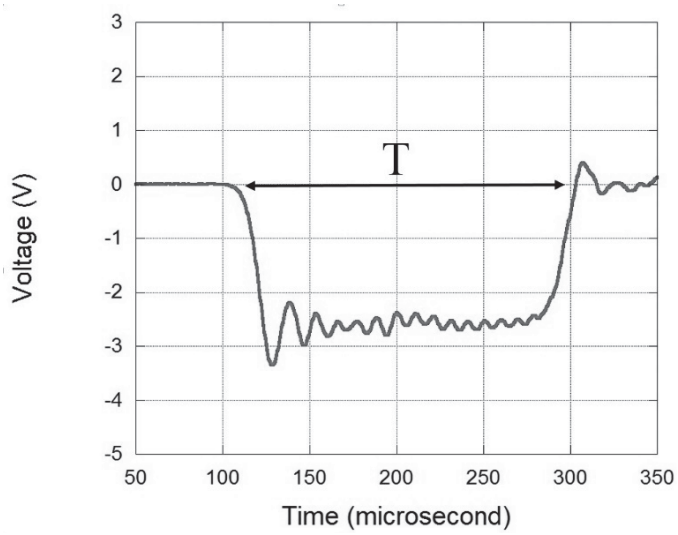

Figure 2.5. Loading duration of the incident wave

$$\sigma = \frac{1}{2}\rho_B C_B V_{SB} \tag{2.2}$$

$$\varepsilon = \frac{1}{2}\frac{V_{SB}}{C_B} \tag{2.3}$$

$$\mathrm{T} = \frac{2\mathrm{L_{SB}}}{\mathrm{C_B}} \tag{2.4}$$

$$C_B = \sqrt{\frac{E_B}{\rho_B}} \tag{2.5}$$

SHPB apparatus used in this study consist of Aluminum 7075-T6 bars, a 200 mm long striker bar, a 1990 mm incident bar and 1550 mm transmitter bar, all with the same diameter of 40.02 mm and strain gage points are 775 mm away from bar/specimen interfaces for both incident and transmitter bar, Figure 2.6. Mechanical properties of bars are given in Table 2.1.

Figure 2.6. SHPB test setup in DTM Laboratory

Table 2.1. Mechanical Properties of Alumınum 7075-T6

Material	*Elastic Modulus, E (GPa)*	*Density, ρ (kg/m3)*	*Poisson's Ratio, ν*
Aluminum 7075-T6	71.7 GPa	2810	0.3

Strain pulses, attained from particular strain gage, $\varepsilon_i, \varepsilon_r$ incident and reflected strain pulses gathered from incident bar gage, whereas ε_t transmitter strain pulse is from transmitter bar gage, as V(t), voltage - time history and calculated by Equation (2.6).

$$\varepsilon(t) = \frac{2x\,V(t)}{V_e x G F x K_g (1+\nu)} \tag{2.6}$$

V_e, GF, K_g, and ν are the excitation voltage of the strain gage bridge, strain gage conditioner gain, strain gage factor, and Poisson's ratio of the bar material, respectively. The values of V_e, GF, K_g, and ν are 10 V, 200, 2.11 and 0.3 respectively.

Assuming the stress waves propagate in incident and transmitter bars without dispersion that pulses recorded from strain gage locations represent the bar/specimen interfaces. One dimensional stress wave theory relates the particle velocities at both ends of the specimen to the three measured strain pulses, Figure 2.7. u_1 and u_2 are the displacements, P_1 and P_2 are the forces on the bar/specimen interfaces and calculated by Equations (2.7), (2.8), (2.9), and (2.10). Stress, strain and strain rate can be calculated by Equations (2.11), (2.12), and (2.13) respectively.

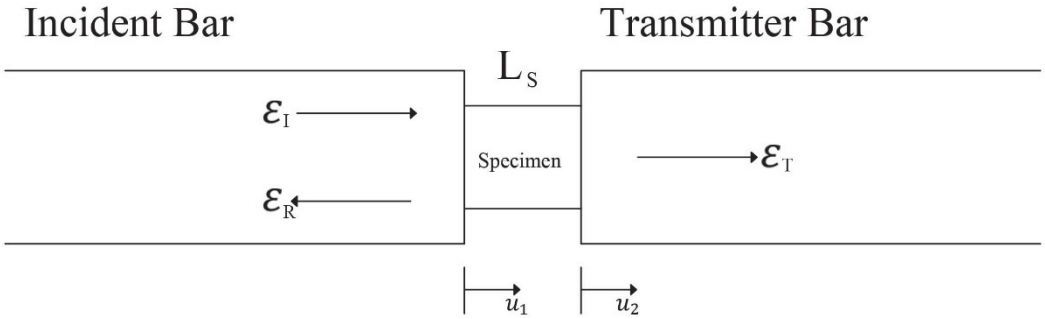

Figure 2.7. Schematic of specimen and waves

$$u_1(t) = C_B \int_0^t [\varepsilon_i(t) - \varepsilon_r(t)]dt \tag{2.7}$$

$$u_2(t) = C_B \int_0^t [\varepsilon_t(t)]dt \tag{2.8}$$

$$P_1(t) = E_B A_B [\varepsilon_i(t) + \varepsilon_r(t)] \tag{2.9}$$

$$P_2(t) = E_B A_B [\varepsilon_t(t)] \tag{2.10}$$

$$\sigma_s(t) = \frac{P_1+P_2}{2A_s} = \frac{E_B A_B}{A_s}[\varepsilon_i(t) + \varepsilon_r(t) + \varepsilon_t(t)]dt \tag{2.11}$$

$$\varepsilon_s(t) = \frac{u_1-u_2}{L_s} = \frac{C_B}{L_s}\int_0^t [\varepsilon_i(t) - \varepsilon_r(t) - \varepsilon_t(t)]dt \tag{2.12}$$

$$\dot{\varepsilon_s}(t) = \frac{C_B}{L_s}[\varepsilon_i(t) - \varepsilon_r(t) - \varepsilon_t(t)] \tag{2.13}$$

A_B, A_s, L_s, σ_s, ε_s and $\dot{\varepsilon_s}$ are represent cross section of the bar, cross section of the specimen, length of the specimen, stress, strain and strain rate of the specimen,

respectively. These are the average stress and strain of the specimen. The stresses at the both ends; front and back stresses of the specimen can be determined as Equations (2.14), (2.15).

$$\sigma_{s1} = \frac{A_B E_B}{A_s}(\varepsilon_i + \varepsilon_r) \tag{2.14}$$

$$\sigma_{s2} = \frac{A_B E_B}{A_s}(\varepsilon_t) \tag{2.15}$$

Where σ_{s1} and σ_{s2} are stress at the incident (front) face and transmitter (back) face end of the specimen, respectively. In SHPB experiment the specimen assumed to be in stress equilibrium, so the specimen deforms nearly uniform, Equations (2.16), (2.17). Therefore stress, strain and, strain rate become Equations (2.18), (2.19), and (2.20). (W. Chen & Song, 2010)

$$\sigma_{s1} = \sigma_{s2} \tag{2.16}$$

$$\varepsilon_i + \varepsilon_r = \varepsilon_t \tag{2.17}$$

$$\sigma_s(t) = \frac{P_1+P_2}{2A_s} = \frac{\sigma_{s1}+\sigma_{s2}}{2} = \frac{E_B A_B}{2A_s}[\varepsilon_t(t)]dt \tag{2.18}$$

$$\varepsilon_s(t) = \frac{u_1-u_2}{L_s} = -\frac{2C_B}{L_s}\int_0^t [\varepsilon_r(t)]dt \tag{2.19}$$

$$\dot{\varepsilon_s}(t) = -\frac{2C_B}{L_s}[\varepsilon_r(t)] \tag{2.20}$$

These equations in Equations (2.18), (2.19) are necessary to produce dynamic stress-strain curve of the specimen. Since it uses only transmitter strain pulse to calculate the stress in the specimen and only reflected strain pulse for strain measurement, it is termed as “1-wave” analysis. Thus, “1-wave” analysis assumes that stress equilibrium is attained in the specimen. On the contrary, the stress in the specimen is calculated in terms of the incident bar using momentum balance of incident and reflected strain pulses is termed as “2-wave” analysis, Equation (2.14). However, it is known that such condition cannot be correct at early stages of the test because of the transient effect that occurs when loading starts at the incident bar/specimen interface while transmitter bar/specimen interface remains at rest. So, time is required for the achievement of stress-state

equilibrium. (Biffi & Tuissi, 2017) After a ringing-up period, where the exact duration depends on the sound speed of specimen and length of the specimen, it is assumed that specimen is in the stress equilibrium, (Gama et al, 2004). The term "3-wave" stress analysis adopted from averages of stresses on both ends of specimen, front stress and back stress. In the case of "3-wave" stress analysis, incident and reflected strain pulses are used to calculate front stress and transmitter strain pulse is used to calculate back stress, then simply the average of the two stresses divided by combined interface areas Equation (2.11) is obtained.

Equations (2.18), (2.19), (2.20) are only valid if there is force equilibrium in the specimen. State of force equilibrium with the front and back faces can be checked with dimensionless R parameter, Equation (2.21).

$$R = 2\frac{(F_1 - F_2)}{(F_1 + F_2)} \tag{2.21}$$

, where F_1 and F_2 represent the front and back bar forces of the specimen, respectively.

While SHPB data reduction procedure, the main difficulty is that the three waves measured at the sections other than the bar/specimen interfaces, in time and distance. They have to be time shifted from strain gage points to bar/specimen interfaces. Shifted strain pulses can be seen in Figure 2.8 at the same time origin.

It is assumed that the incident, reflected and transmitter pulses propagate along the length of the bars with minimal dispersion. However, the propagation of stress pulses in bars has dispersive nature. This leads the development of oscillations. In SHPB tests to represent the concrete material behavior on the specimen, the diameter of the specimen has to be at least 10 times bigger that of the maximum aggregate size, so the diameter of the bars has to be at least specimen diameter. Large diameter, 40.02 mm bars are used via testing concrete specimen, which makes stress waves dispersion more critical.

As mentioned in Chapter 1, to eliminate the dispersion effects and to avoid premature failure within the concrete specimen pulse shaper (PS) usage is crucial. During the impact load of the striker bar, plastic deformation of pulse shaper filters out the high-frequency part of stress pulse. In this study, circular ethylene-propylene-diene monomer copolymer (EPDM) rubber was used to change the shape of incident stress wave propagating in the incident bar. EPDM rubber was punched out circular that has 3 mm thickness and 12.7 mm diameter, Figure 2.9. Pulse shaper was attached to the free end of the incident bar, Figure 2.10.

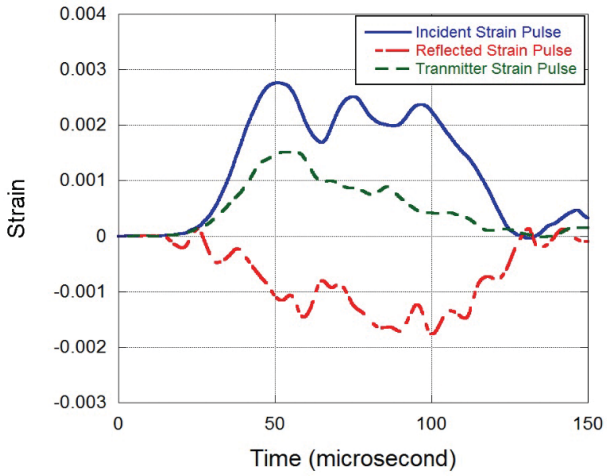

Figure 2.8. Time shifted strain pulses

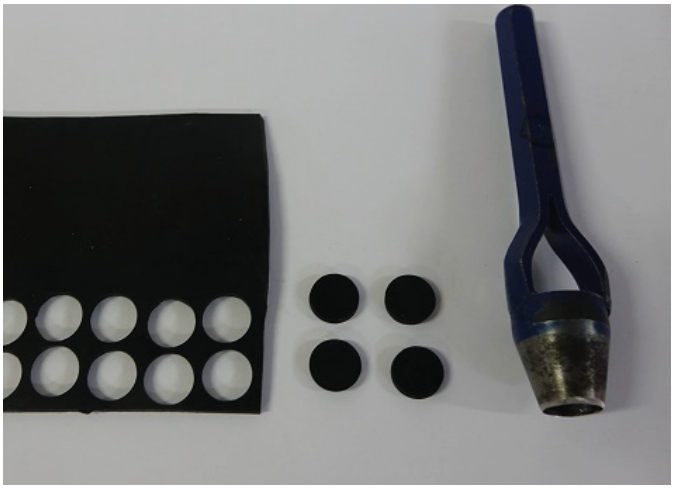

Figure 2.9. Punched EPDM Pulse Shaper

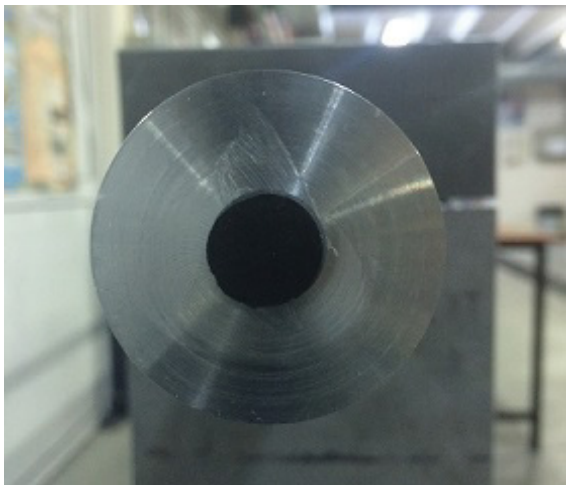

Figure 2.10. EPDM pulse shaper on the face of incident bar

Since signal measurement is monitored from some distance away from bar/specimen interface, the dispersion can affect the result of the SHPB tests that the

measured stress waves at strain gage location may not be representative of the stress wave at the bar/specimen interface, Figure 2.11. For precise results, direct force measurements from front and back interfaces of the specimen are critical. The highly sensitive circular piezoelectric quartz crystals are used. The mechanical impedance (ρC) values of quartz crystal and aluminum bars are very close to each other and these values are 1.51x10^7 kg/m^2s and 1.42x10^7 kg/m^2s, respectively. Boston Piezo-Optics piezoelectric quartz crystals have 0.254±0.01 mm thickness and 40.02 mm diameter as same diameter as aluminum bars. They have a piezoelectric constant of 2.3 pC/N. Quartz crystals added to incident and transmitter bar ends of the specimen and thin aluminum discs with 5 mm thickness were bonded via Circuit Works CW 2400 conductive epoxy to quartz crystals to cover them from the direct impact, Figure 2.11. Signals gathered from quartz crystals, Kistler 5010A charge amplifier is used. Kistler 5010A is also connected to the oscilloscope that measured voltage signals are displayed and monitored.

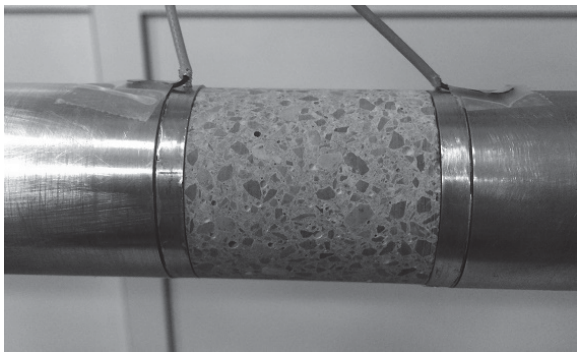

Figure 2.11. Quartz crystal embedded SHPB setup

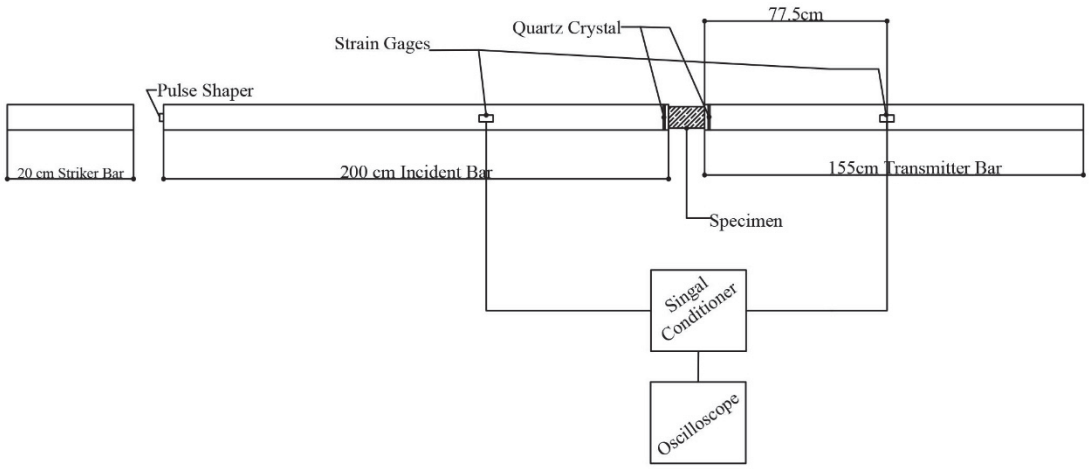

Figure 2.12. Schematic of modified SHPB used in dynamic testing of the concrete specimen.

2.5 Modeling Introduction

In this study, a program for nonlinear dynamic analysis of structures in three dimensions, the finite element software LS-DYNA 971 is used for both to verify SHPB experiments of the concrete and to investigate SHPB studies numerically, striker bar geometry, wave shaping, and so forth. (Hallquist, 2006). Since the simulations of the concrete specimens subjected, high strain rates and high pressures, Holmquist-Johnson Cook, HJC (MAT_111 *MAT_JOHNSON_HOLMQUIST_CONCRETE) constitutive model is selected. This model is based on work by Holmquits, Johnson, & Cook (1993).

2.6 Material Model

Holmquist-Johnson Cook concrete model can be used for concrete subjected to high pressures, large strains, and high strain rates. The equivalent strength is expressed as a function of the pressure, strain rate, and damage. The pressure is expressed as a function of the volumetric strain and includes the effect of permanent crushing. The damage is accumulated as a function of the plastic volumetric strain, equivalent plastic strain, and pressure. (Holmquits et al. 1993) The HJC model consists of three parts: equivalent strength, accumulated damage, and the equation of state (EOS). The equivalent strength part of the model is nonlinear and illustrated in Figure 2.13(a). The expression is given by Equation (2.22) and defined by normalized equivalent stress, σ^* vs. normalized pressure, P^* where $\sigma^* = {\sigma}/{f'_c}$ and $P^* = {P}/{f'_c}$ represent equivalent stress, and hydrostatic pressure, respectively and both are normalized by the quasi-static uniaxial compressive strength, $f'c$.

$$\sigma^* = [A(1-D) + BP^{*N}][1 + C ln\dot{\varepsilon}^*] \tag{2.22}$$

Where D is a damage parameter ($0 \leq D \leq 1$) which is applied to the cohesive strength, A. The difference between undamaged and fractured strength is represented by A constant. B and N are also strength constants that B is the normalized pressure hardening coefficient and N is the normalized pressure hardening exponent. C and $S_{f\max}$ are the strain rate constant and the maximum dimensionless strength, respectively and $\sigma^* \leq S_{f\max}$. $\dot{\varepsilon}^*$ denotes the dimensionless equivalent strain rate, shown as $\dot{\varepsilon}^* = \dot{\varepsilon}/\dot{\varepsilon}_0$

where $\dot{\varepsilon}$ is the actual strain rate and $\dot{\varepsilon}_0$ represents the reference strain rate. Additionally, T^* is normalized tensile strength constant, shown as $T^* = T/f'c$ where T is maximum tensile hydrostatic pressure.

HJC model includes the accumulated damage model for concrete is seen in Figure 2.13(b) to calculate the value of damage variable between zero and one. The damage, D, is accumulated as a function of the plastic volumetric strain, $\Delta\mu_P$ and equivalent plastic strain, $\Delta\varepsilon_P$, Equation (2.23).

$$D = \sum \frac{\Delta\varepsilon_P + \Delta\mu_P}{\varepsilon_p^f + \mu_p^f} \tag{2.23}$$

Where $\varepsilon_p^f + \mu_p^f = D_1(P^* + T^*)^{D_2}$ represents the plastic strain to fracture at constant pressure and D_1 and D_2 are the damage material constants. Minimal damage constant, $\varepsilon_{f\min}$ is defined, when $P^* = -T^*$ that concrete cannot bear the plastic strain.

The equation of state (EOS) part of the model describes the hydrostatic pressure and volume relation, Figure 2.13(c). The loading and unloading process of concrete is divided into three regions that segmented by the crushing and locking points. The first region is a linear elastic region at $P \leq P_{crush}$ and the material is an elastic state in this area. $P_{crush} = K\mu_{crush}$ where P_{crush}, K, μ_{crush} are pressure, elastic bulk modulus and volumetric strain, respectively. The second region is crushable transition region at $P_{crush} \leq P \leq P_{lock}$ and material is plastic transition state in this area. Plastic volumetric strain and pressure increase while the size of interior voids of the concrete the decreases. The third region is locked region which is normalized polynomial, defines the relationship for fully dens material. (Y.-S. Tai & Tang, 2006) The pressure and the volumetric strain relationship is given in Equation (2.24).

$$P = K_1\bar{\mu} + K_2\bar{\mu}^2 + K_3\bar{\mu}^3 \tag{2.24}$$

Where K_1, K_2, and K_3 are constants and corrected volumetric strain is $\bar{\mu} = \frac{\mu - \mu_{lock}}{1 + \mu_{lock}}$ that μ_{lock} is locking volumetric strain. $T(1 - D)$ part is the tensile pressure area.

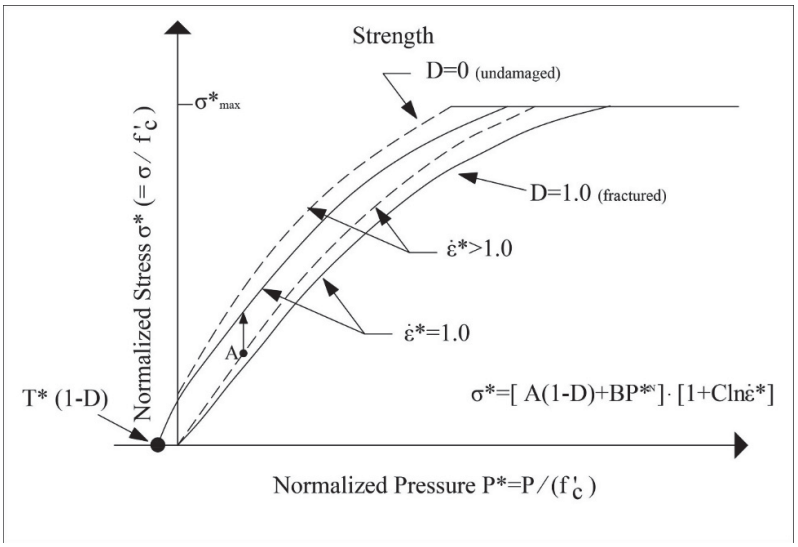

(a)

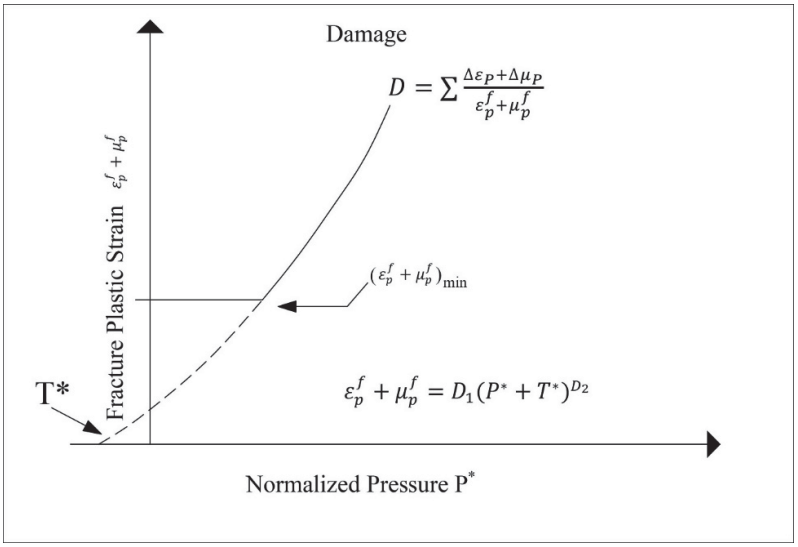

(b)

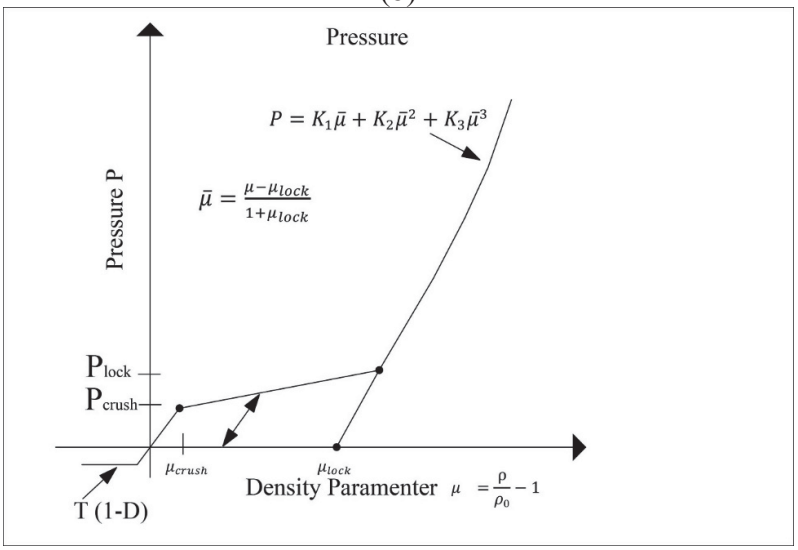

(c)

Figure 2.13. The Material model of the concrete (a) Equivalent strength model, (b) damage failure model, (c) Equation of State

To determine the parameters of the material model, the work to be done is primarily started with the physical properties of the concrete. For this purpose, the density was determined. For density calculations, cylindrical concrete specimens weighed and measured in volume were used and the average density value was obtained as 2183 kg/m^3. As previously mentioned, the lowest strain rate of deformation of the concrete material in accordance with the quasi-static tests 10^{-4} 1/s at an average compressive strength value was determined to be 62 MPa. As a result of calculations made in accordance with ACI 318-08 regulation, by the slope of the line in a stress-strain curve, 0.45 f′c, concrete elastic modulus of concrete material was found to be 32 GPa. The shear modulus, G, is calculated to be 13.32 GPa by $E/2(1+\upsilon)$ formulation. Since, confined tests were not conducted, strength equation parameters A and N were taken as literature values 0.79, 0.61, respectively. (Holmquits et al. 1993) B is gathered from the numerical analysis that the value well suited with transmitter bar data is selected, 0.90. Then, the pressure parameters are calculated using Equations (2.25), (2.26), and (2.27).

$$P_{crush} = \frac{\mathrm{f'c}}{3} \tag{2.25}$$

$$\mu_{crush} = \frac{P_{crush}}{K_{elastic}} \tag{2.26}$$

$$\mu_{lock} = \frac{\rho}{\rho_0} - 1 \tag{2.27}$$

In equation 2.27, where ρ represents current density, ρ_0 denotes the reference density and their values are 2560 kg/m^3, 2183 kg/m^3, respectively. $K_{elastic}$ and P_{crush} are calculated as the directions through Holmquits et al. (1993) and found out to be 17.76 MPa and 21 MPa, respectively. μ_{lock} and μ_{crush} are found by equations above 0.173 and 0.001, respectively. Locking pressure, P_{lock} all the air voids are extracted from concrete due to compaction taken from Holmquits et al. (1993). The constants at compact region, K_1, K_2, and K_3 are also taken from literature Holmquits et al. (1993). Split tensile tests were performed to find tensile strength of concrete, T, as 6.3 MPa. $S_{f\max}$ is calculated through the directions in Y. S. Tai, (2009)

Determination of the C, strain rate sensitivity constant, SHPB and quasi-static tests were conducted. In the Holmquist-Johnson Cook concrete material model, the effect of the strain rate to the normalized compression strength is defined by the expression $1 + C\ ln(\dot{\varepsilon}/\dot{\varepsilon}_0)$. Reference strain rate, $\dot{\varepsilon}_0$ is selected as the lowest strain rate in the uniaxial

compression tests, $3.55x10^{-5}$ which is obtained from the lowest strain rate during quasi-static tests. There are two types of C stain rate sensitivity parameter results conducted. One of them is C_{static}, which have found from only quasi-static tests at 10^{-2}, 10^{-3}, and 10^{-4} as seen in Figure 2.14. a). Another one is the $C_{dynamic}$, in which dynamic results from SHPB test also gathered to get this constant, Figure 2.14. b). So, all the parameters used for concrete material can be seen in the Table 2.2.

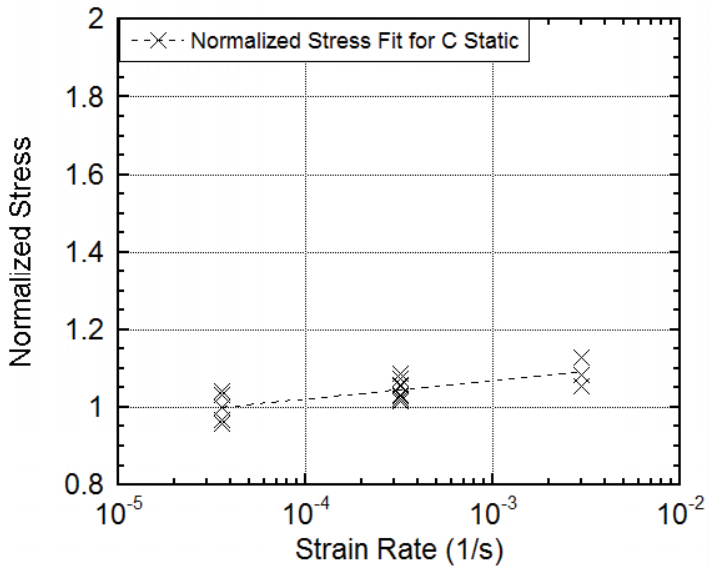

(a)

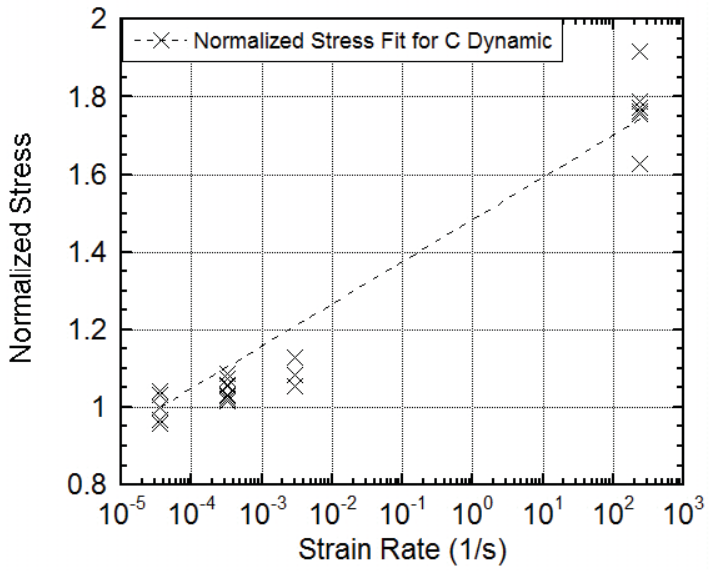

(b)

Figure 2.14. (a) Normalized Stress Fit for C_{Static} (b) Normalized Stress Fit for $C_{Dynamic}$

The transmitter waves obtained using the values were compared with the experimental results, strain rate sensitivity parameter C equals to zero, strain rate sensitivity parameter value C_{static}, found with static test results and strain rate sensitivity parameter value

$C_{dynamic}$, found with both static and dynamic test results for the determination of the effectiveness of the strain rate sensitivity parameter in Figure 2.14. It has been found that the stress waves are obtained by C_{static}, the closest result to the with pulse shaper and without pulse shaper experiments. This situation is consistent with the existing results in the literature (Bischoff & Perry, 1991). In this point, it has been determined that the increase in strength at high strain rates increases both by the strain rate sensitivity of the material and by the effect of the unloaded pressure, as well as the inertia.

Table 2.2. Parameters of HJC Model for Concrete
(*Source: Holmquist et al., 1993)

Strength Constants	**Values**
A	0.79*
B	0.90
N	0.61*
C	0.0205
f′c (GPa)	0.062
$S_{f\max}$	5.7
G (GPa)	13.32
Damage Constants	Values
D1	0.04*
D2	1.0*
$\varepsilon_{f\min}$	0.01
Pressure Constants	Values
P_{crush} (GPa)	0.021
μ_{crush}	0.001
K_1 (GPa)	85*
K_2 (GPa)	-171*
K_3 (GPa)	208*
P_{lock} (GPa)	0.80*
μ_{lock}	0.173
T (GPa)	0.0063

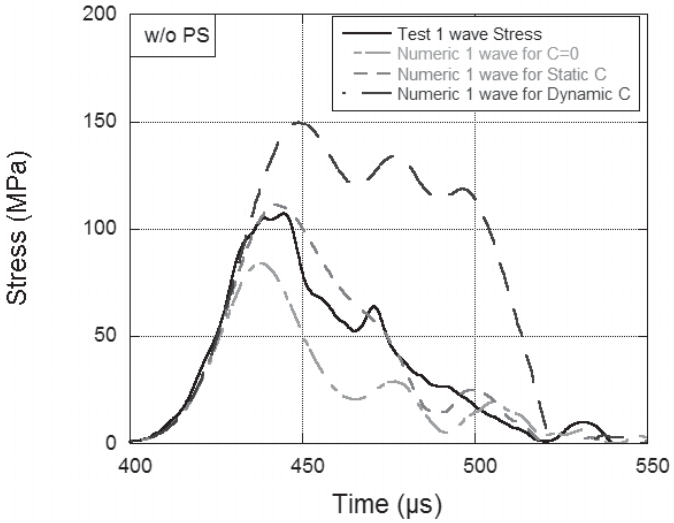

(a)

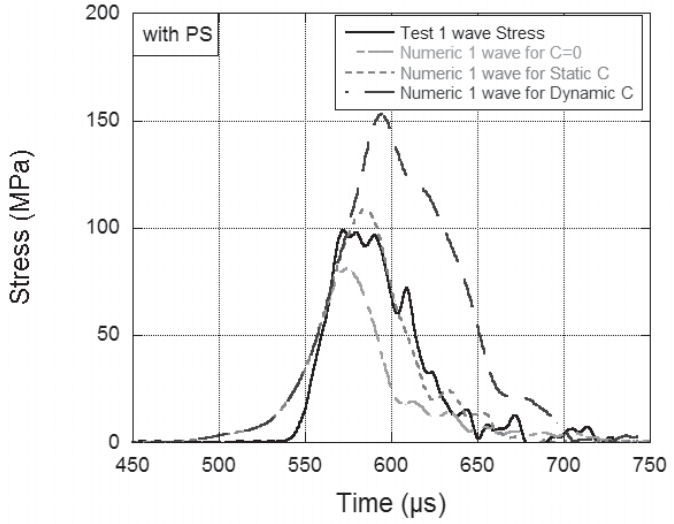

(b)

Figure 2.15. Effectiveness C strain rate sensitivity for (a) without Pulse Shaper Case, (b) with Pulse Shaper

2.7 Numerical Modelling

Split Hopkinson Pressure Bar experimental studies were modeled to study damage and stress propagation in a three-dimensional SHPB finite element model. The results of the numerical simulations were compared with the SHPB experiments. The numerical analysis was performed using a commercially available explicit finite element code LS-DYNA 971 at Dynamic Testing and Modelling Laboratory. Model and meshes were generated in LS-PREPOST 4.3. (Manual, 2007) The output data was obtained from strain gage points on the incident and transmitter bars of SHPB apparatus model. In the ideal case, bar stress measurements from the model, the output data is expected to be matches

the data measured by strain gages on the incident and transmitter bars in SHPB experiments. This indicates that the wave propagation behavior in the bar is captured accurately in the model.

In the current study, all the 3D models for the Split Hopkinson Pressure Bar test setup; striker, incident and transmitter bars, aluminum disks, and concrete specimen were created in the LS-Prepost V4.5.1. There are 317950 elements and 339999 nodes total for 8 solid parts. The 8-node hexahedron type elements, which has six faces, eight corners and twelve edges are used for meshing in the LS-Prepost as seen in the Figure 2.16. Three different element sizes were used during the meshing of three-dimensional models. Striker, incident and transmitter bars were meshed with 3 mm size elements, while aluminum disks and concrete specimen meshed with 2 mm and 1.5 mm size elements, respectively. The numerical model of SHPB testing setup is also seen in Figure 2.17. The incident and transmitter bars each consist of two parts, which is the location of the strain gage in the middle of these parts. As the mesh parts approach the sample, the size of the elements decreases. The models of striker, incident, transmitter bars and aluminum disks were modeled using MAT_ELASTIC_01 material model while specimen was modeled using MAT_JOHNSON_HOLMQUIST_CONCRETE_111 material model. The axial movement was allowed only in the z-direction that INITIAL_VELOCITY_GENERATION is defined in striker bar to initiate the numerical test for without pulse shaper case, while with a pulse shaper case incident pulse was defined by DEFINE_CURVE to the incident front face to the striker bar way. The contact between striker bar and the incident bar was defined by CONTACT_SURFACE_TO_SURFACE where slave segment and master segment were striker and incident bars, respectively. The static coefficient of friction (FS) and dynamic coefficient of friction (FD) was set to 0.3 and 0.2 in contact definition. In this section, the surfaces where the incident and striker bars look at each other were defined by the segment set. The contact definition of the specimen with incident and transmitter bars was defined by CONTACT_NODES_TO_SURFACE where slave part was the specimen which was defined by NODE_LIST and consist of 33976 nodes in total. The static coefficient of friction (FS) and dynamic coefficient of friction (FD) was set to 0.1 and 0.05 in this contact definition. In CONTROL_CONTACT section ENMASS was selected as 1 which means treatment of the mass of eroding nodes of solid elements are retained and continue to be active in contact. In CONTROL_ENERGY section HGEN, SLNTEN, and RYLEN were selected as EQ2 that hourglass energy and energy dissipation were

computed and included in the energy balance. There were also ELOUT, NODOUT, RCFORC options were activated in DATABASE_OPTION that stress history from strain gage points, displacement and force history of the front and rear faces of the specimen were obtained.

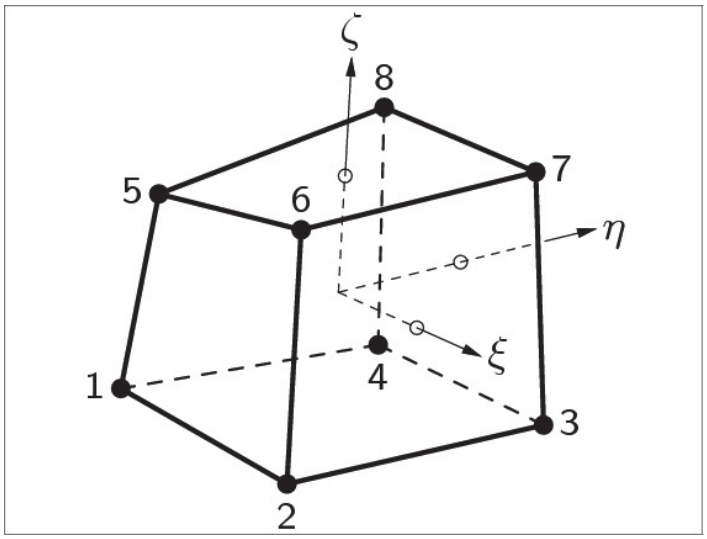

Figure 2.16. Representation of the 8-node hexahedron solid element

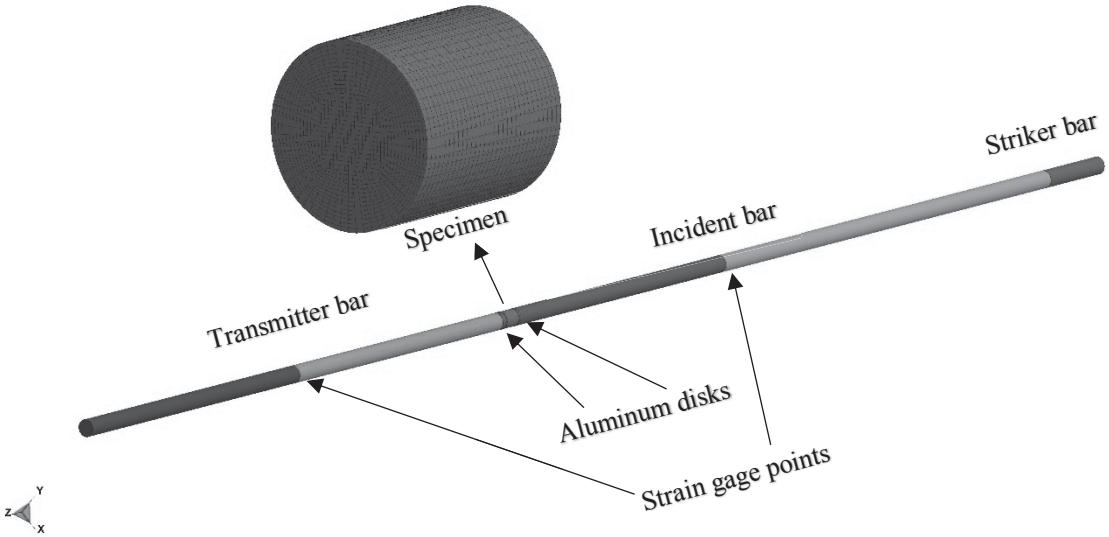

Figure 2.17. SHPB test setup for the numerical simulations model

CHAPTER 3

RESULTS AND DISCUSSION

3.1 Experimental Results

3.1.1 Quasi-static Test

For the characterization of the concrete material, tests were carried out at both static and dynamic strain rates. Static tests at low strain rates were performed using a Shimadzu AG-X 300kN static compression and tension device. When static tests were applied, two different types of test methods were applied to obtain the material model parameters. These are the uniaxial compression test and the split tensile test. Tests were performed at the desired strain rates by controlling the cross-head speed of the testing device using Equation (3.1) in the uni-axial compression tests.

$$v_{cr} = \dot{\varepsilon} L \tag{3.1}$$

Due to the brittle nature of the concrete material, the fracture strain value is quite small. Because of this small strain value, the displacement values of the compression heads cannot be used in strain measurements and this is called machine compliance, Figure 3.1, Figure 3.2. An average of 160 seconds was needed to reach the max force value, as seen in the force-time curve, Figure 3.1.

Static tests started with 10^{-4} s^{-1} tests, and the cross-head speed was 0.0045 mm/sec. Two sample stress-strain curves for these tests are given below. 60 MPa peak stress and 0.003 failure strain were observed.

The onset and progress of the damage were examined by recording the test with the video camera. Deformations of specimen #1 corresponding to the four different points on the stress-strain curves are given in Figure 3.3. Especially at point D the damage progresses to the surface, the occurrence of damage in the axial and radial directions is observed on the sample surface in Figure 3.4. With the progress of deformation, catastrophic damage occurs in the sample and the sample is disintegrated and spall.

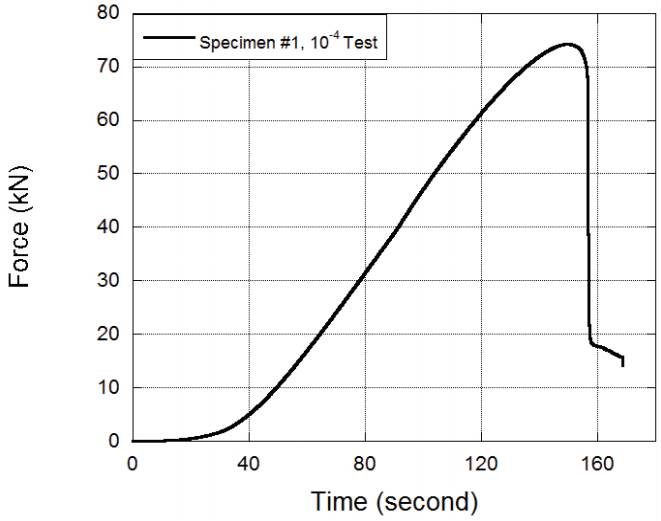

Figure 3.1. Force – Time history of 10^{-4} s^{-1} test

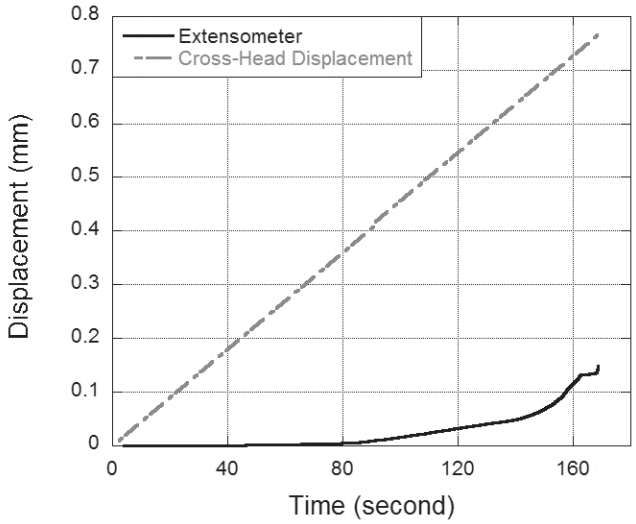

Figure 3.2. Displacement – Time history of 10^{-4} s^{-1} test

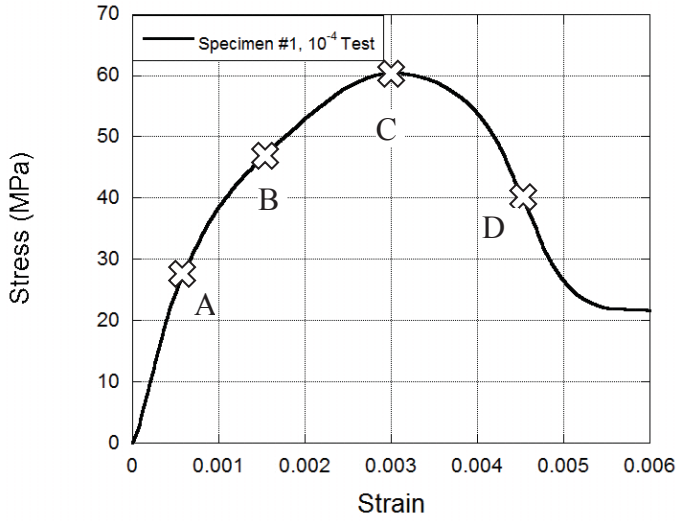

Figure 3.3. Stress-Strain Curve of the 10^{-4} s^{-1} Quasi-Static Test

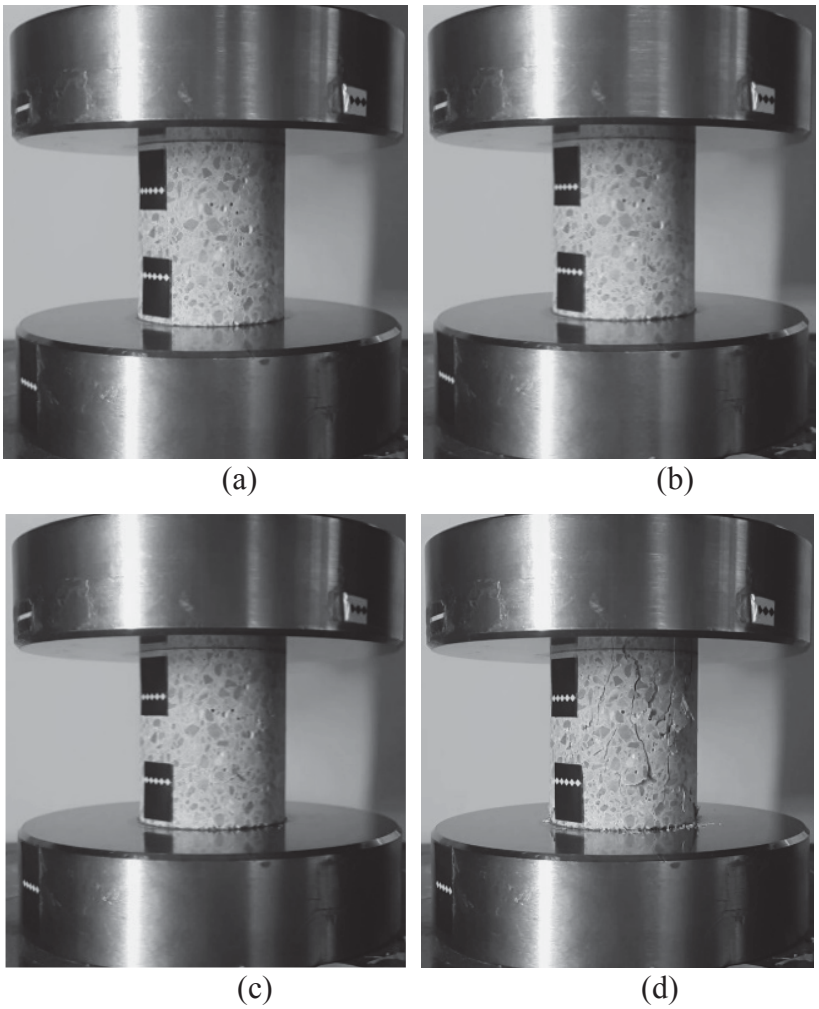

Figure 3.4. 10^{-4} s^{-1} Quasi-Static Test deformation history.

The proportions of the deformation values coming from the vertical and horizontal strain gages are taken and the Poisson's ratio is calculated as mentioned in Chapter 2. This measured value was found to be very close to the Poisson's ratio value of 0.22 in the literature. In this test, the sample was fractured at a compressive strength of about 62 MPa and a strain value of ~ 0.0037. Strain rate value of the test was calculated from Strain-Time history and is 3.5538×10^{-5} s^{-1} as seen in Figure 3.5

Quasi-static tests were carried on with tests at 10^{-3} s^{-1} strain rate. In these tests, cross-head speed was 0.045 mm/sec. An average of 16 seconds was needed to reach the max force value in this strain rate, as seen in the force-time curve in Figure 3.6 (a). In Figure 3.6(b) the stress-strain curve for these tests are presented. The failure stress and strain were obtained as 65.5 MPa and 0.0038 on the stress-strain curve of Specimen #1 is given in Figure 3.6 (b).

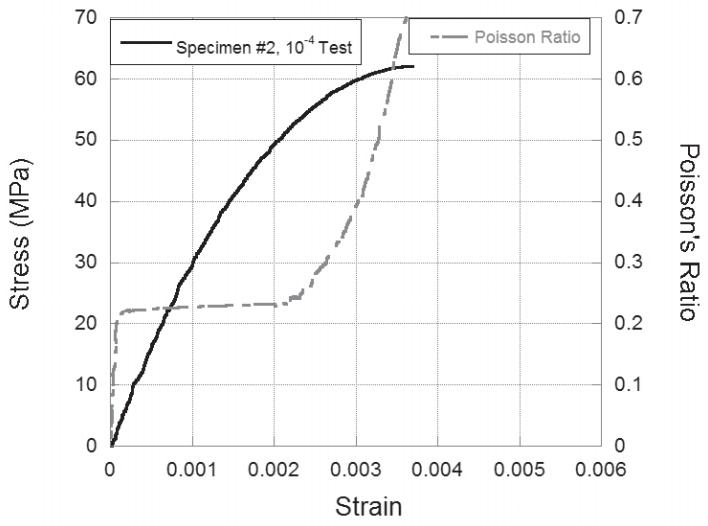

(a)

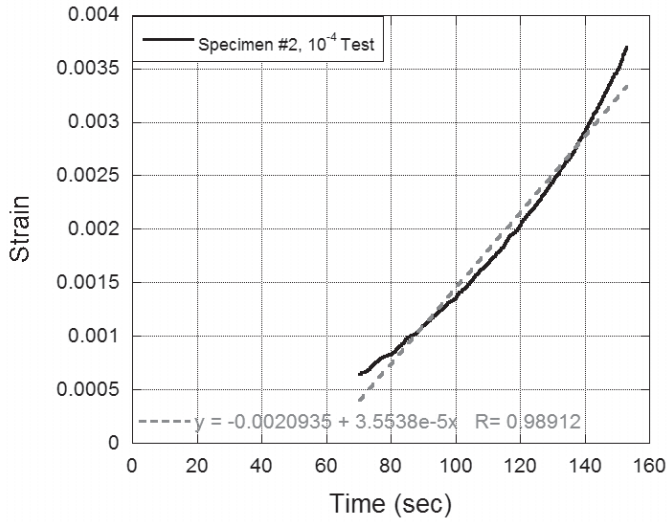

(b)

Figure 3.5. Strain Gage Placed Stress (MPa) & Poisson's Ratio & Strain and Strain & Time Curves of the 10^{-4} s^{-1} Quasi-Static Test

In addition to the tests using video extensometer, tests at the 10^{-3} s^{-1} strain rate were performed by placing strain gauges in different orientations on the surface of the specimen, as detailed previously. The stress-strain curve of a test in which the strain value from the strain gages is used is given in Figure 3.7. This test result is consistent with the previous test results and 3.2303×10^{-4} s^{-1} strain rate was found. As seen in Figure 3.7 the stress-strain curves for these tests are presented. The failure stress and strain were obtained as 65.4 MPa and 0.0034 on the stress-strain curve of Specimen #2 is given in Figure 3.7.

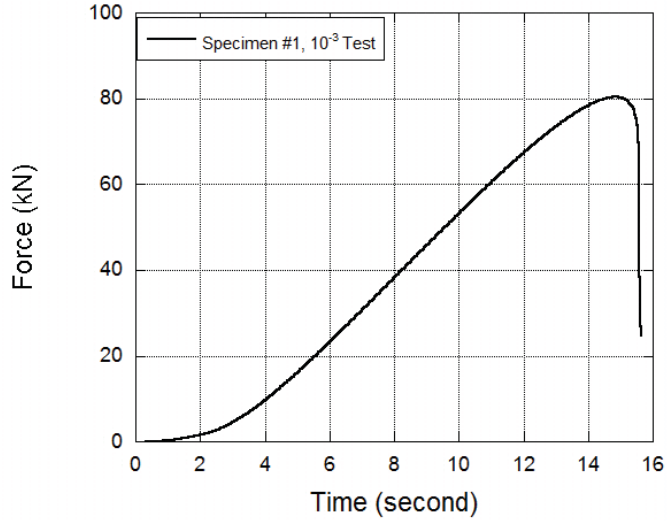

(a)

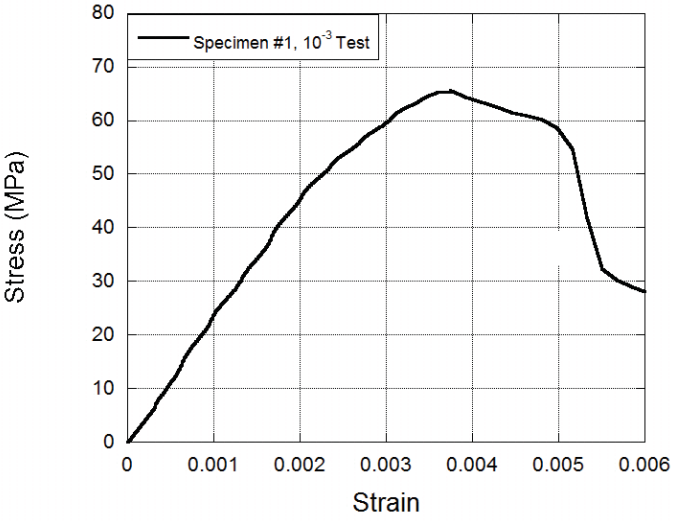

(b)

Figure 3.6. Force-Time and Stress-Strain Curves of the 10^{-3} s^{-1} Quasi-Static Test

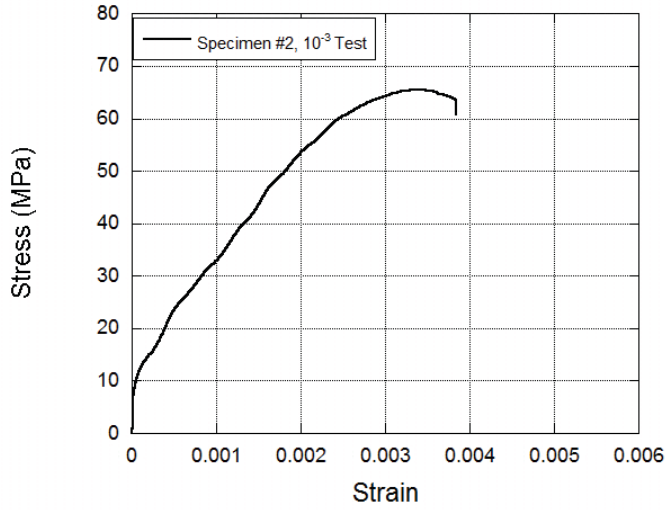

Figure 3.7. Stress (MPa) - Strain Curve of the 10^{-3} s^{-1} Quasi-Static Test

Quasi-static tests were continued with the last 10^{-2} s^{-1} strain rate tests. One sample test result is presented in Figure 3.8 below. From the tests, it was determined that the concrete has an average compressive strength of 66.35 MPa at 10^{-2} s^{-1} strain rate. Failure strain values were obtained at ~ 0.0025 levels. The onset and progress of the damage were investigated by recording the test with a video camera. Specimen #1 which was exposed to 10^{-2} s^{-1} strain rate quasi-static test on the strain-strain curves are given in Figure 3.8. With the increase of the strain rate in the formation of the damage, it is observed that the effect of expansion especially in the radial direction increases considerably and the radial deformation in the region near the fixed head of the sample is obviously seen. An average of 1.6 seconds was needed to reach the max force value in this strain rate, as seen in the force-time curve in Figure 3.8(a).

In addition to the tests using video extensometer for this strain rate, the quasi-tests were also carried out by placing strain gauges in different orientations on the specimen surface as described in detail above. The stress-strain curves for the test in which the strain value measured from the strain gages is used are given in Figure 3.8 and this result is consistent with the previous results and 2.971×10^{-3} s^{-1} strain rate was found. The failure stress and strain were obtained as 65.3 MPa and 0.0024 on the stress-strain curve of Specimen #2 is given in Figure 3.9.

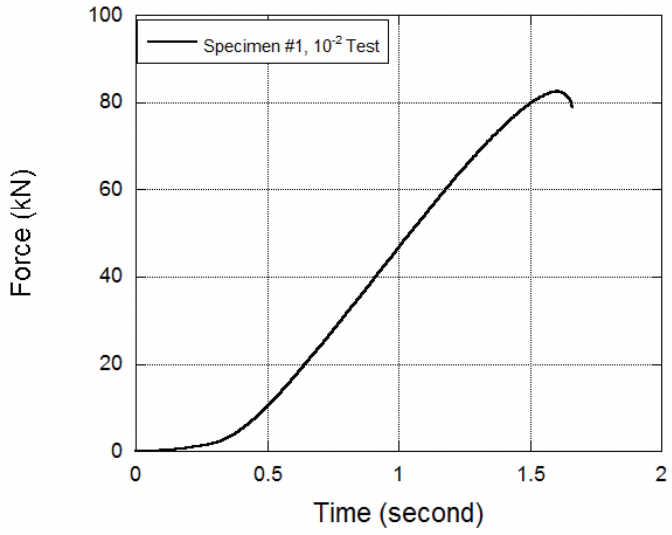

(a)

Figure 3.8. Force-Time and Stress-Strain Curves of the 10^{-2} s^{-1} Quasi-Static Test

(cont. on next page)

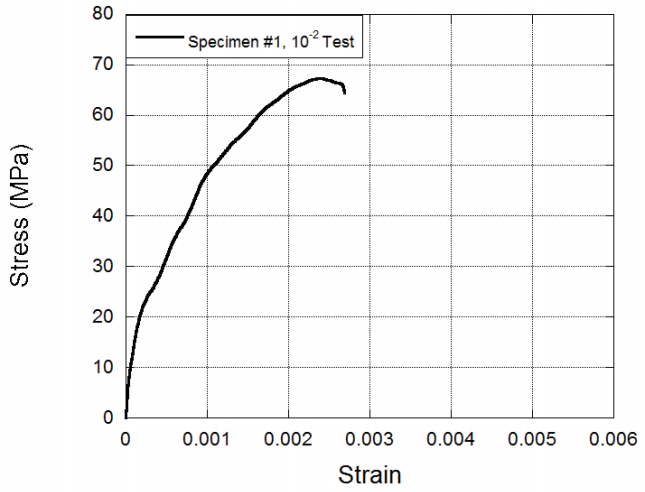

(b)

Figure 3.8. (cont.)

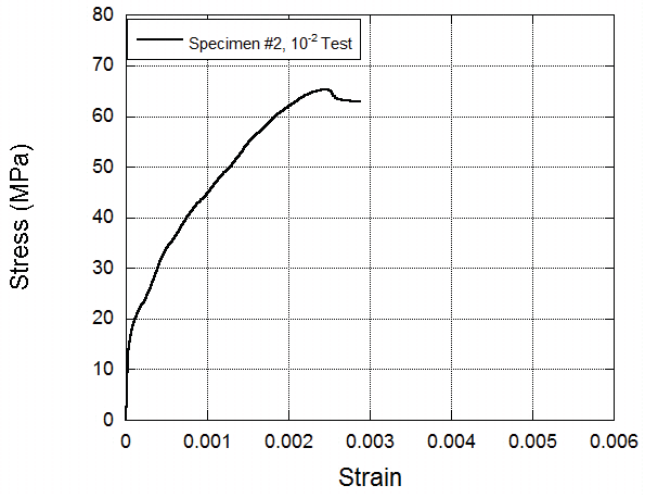

Figure 3.9. Stress (MPa) - Strain Curve of the 10^{-2} s^{-1} Quasi-Static Test

The compressive strength increases with the increase of strain rate. The average stress-strain curves for different strain rates are shown in Figure 3.10 is presented. From all the quasi-static test, the average failure strain values were about 0.003, 0.0033, and 0,0035 for 10^{-2} s^{-1}, 10^{-3} s^{-1} and 10^{-4} s^{-1} strain rates. However, as it was mentioned above, some of tests' s strain measurements were taken directly from the strain gages that were placed on the surface of the concrete specimens that those results are more reliable than that the strain measurements, calculated from video extensometer results. Those compressive stress values gathered from strain gages tests are 70, 64, and 62 MPa for 10^{-2}, 10^{-3}, and 10^{-4} s^{-1} strain rates, respectively. The failure strain value was about 0,0036 and it was almost the same for 10^{-2} s^{-1}, 10^{-3} s^{-1}, and 10^{-4} s^{-1} strain rates. Calculated average strain rates from those tests are $2.97x10^{-3}$, $3,23x10^{-4}$, and $3,55x10^{-5}$ s^{-1} respectively.

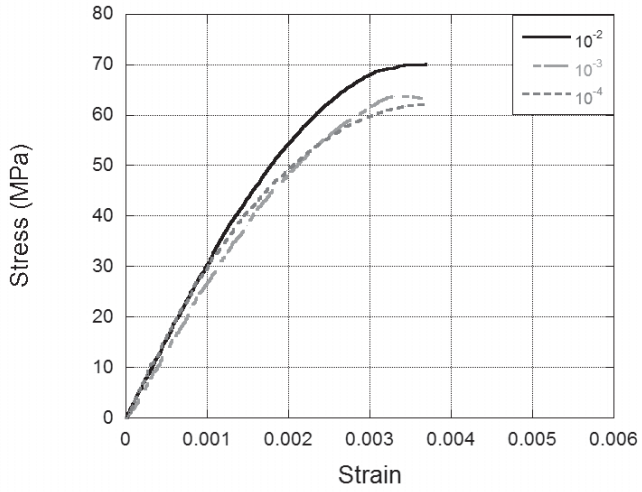

Figure 3.10. Strain-strain curves at 10^{-2}, 10^{-3}, 10^{-4} s^{-1} strain rates.

In order to measure the tensile strength of the concrete material, tests on the strength of the split-tensile strength tests were carried out. The ASTM C 496 standard was followed to carry out these tests. During the tests, 3 mm thick and 25 mm wide plywood slats were prepared to support the upper and lower lateral surfaces of the concrete sample. These slats were used in the test of specimens with 24 mm length, 39.5 mm diameter. Typical stress-time (sec) curves and damage profiles obtained from the concrete sample during the test are shown in Figure 3.11. The tensile stress calculation was also performed using Equation (3.2). The loading speed of the specimen was selected as 1000 kPa / min according to the standard and as can be seen in Figure 3.11 that, the tensile strength value of the concrete specimens was determined as 6 MPa.

$$T = \frac{2P}{\pi LD} \tag{3.2}$$

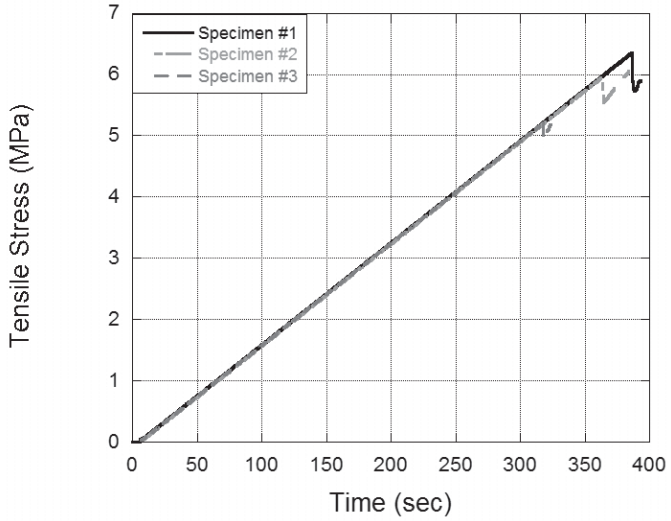

Figure 3.11. Tensile Stress (MPa) – Time (sec) curve of split tensile tests

3.1.2 High Strain Rate Test

Typical SHPB strain measurements of a tested concrete specimen, incident and transmitter waves are shown in Figure 3.12.

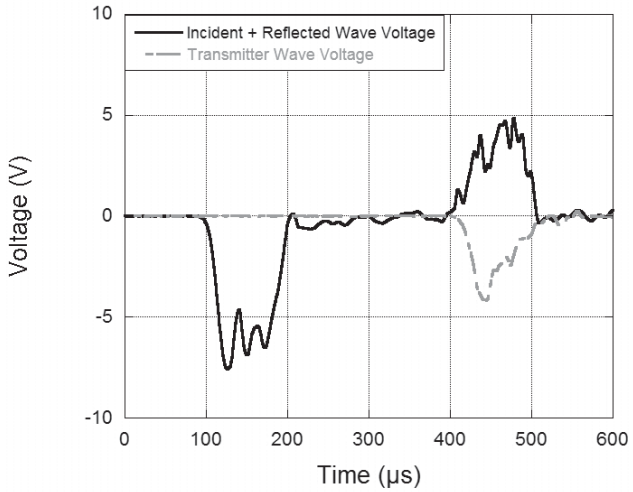

Figure 3.12. Typical SHPB strain gages measurements as a function of time for the tested concretes.

As previously described, an example of signaling histories obtained from strain gages placed on bars in a conventional SHPB (without pulse shaper) test graph is presented in Figure 3.12. From these voltage – time signals, the strain history is calculated using Equation (2.6). The strain history is multiplied by the modulus of elasticity modulus values to obtain the history of stress propagating in the bars.

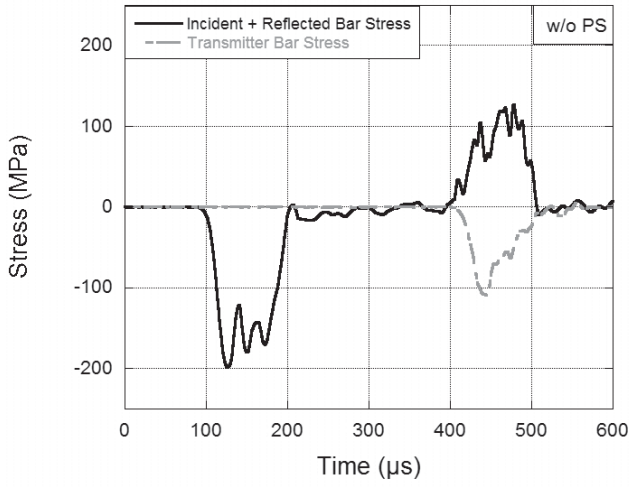

(a)

Figure 3.13. Classical SHPB tests (a-c) stress- time histories.

(cont. on next page)

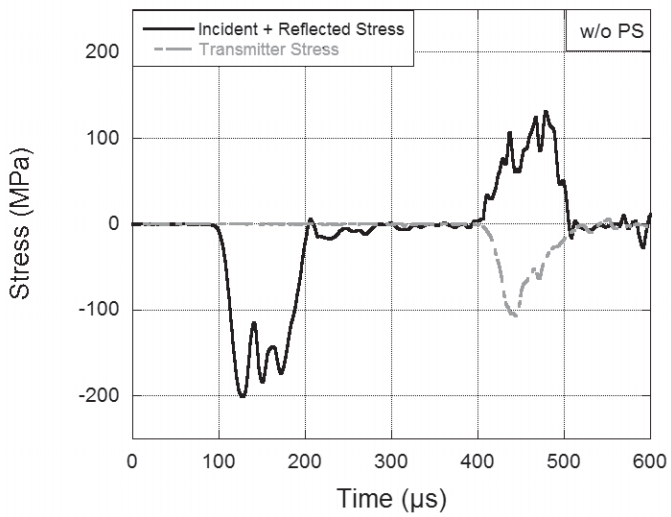

(b)

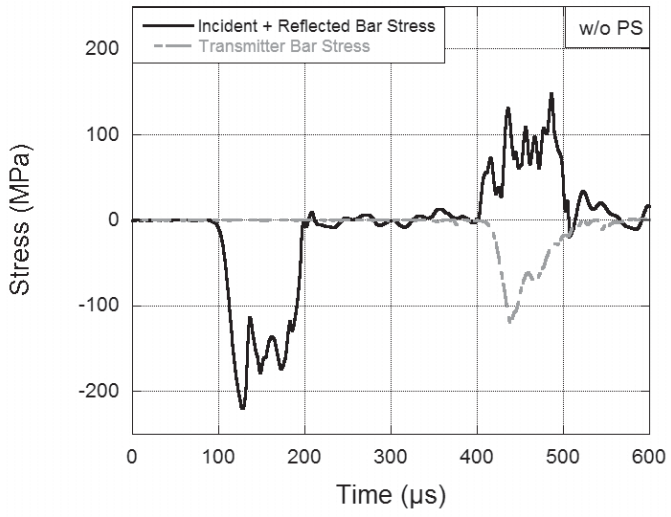

(c)

Figure 3.13. (cont.)

It is possible to obtain the dynamic stress-strain curves of the material by considering the one-dimensional wave progress theory in the SHPB test results in the strain history. For this purpose, using the Equations (2.11), (2.14), and (2.15), the average, the front and back of the sample the stresses on the surface and the strain values of the sample can be calculated. If the results from Equation (2.15) are used and a single transmitter (transmitter) is used, this analysis is called 1-wave analysis. If Equations (2.14) and (2.15) are to be used, the analysis, in this case, are called 2-wave and 3-wave analysis, respectively as seen in the Figure 3.14.

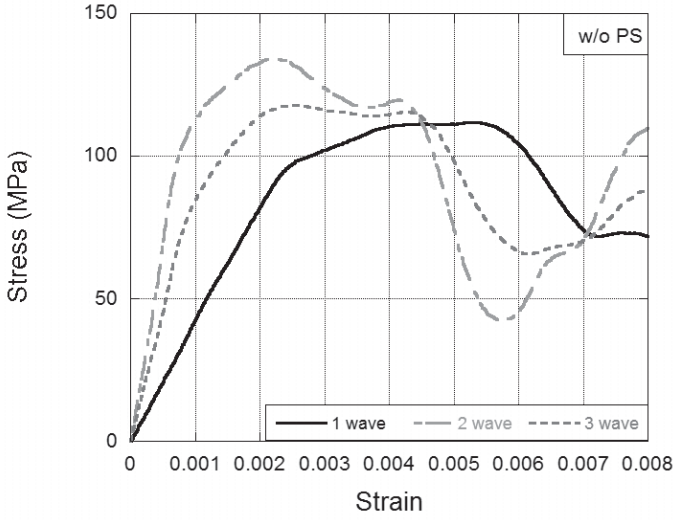

(a)

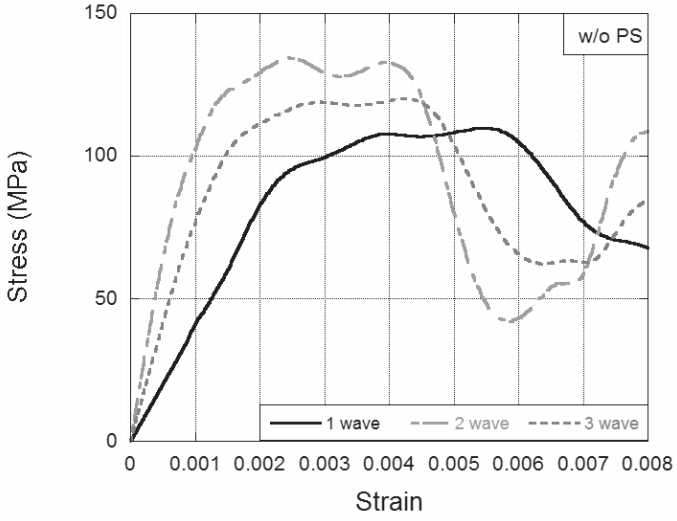

(b)

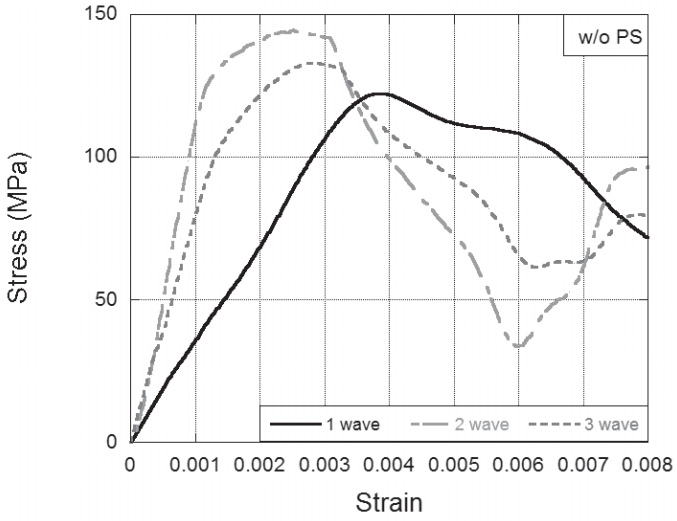

(c)

Figure 3.14. 1-wave, 2-wave, 3-wave Stress - Strain Curves for without Pulse Shaper Tests

In Figure 3.14 above, SHPB test results without pulse shaper are presented. 1-wave analysis basically assumes that the stresses on the front and back sides of the sample are equal to each other, that is, there is a stress equilibrium in the concrete specimen. For this reason, only the back-surface force is taken into consideration in the calculation of stress. By considering the momentum balance of incident and reflected waves, the stress on the front surface of the sample can be calculated and this is called 2-wave analysis. In particular, at the beginning of the loading, the stress equilibrium is not immediately reachable within the sample. This is because the loading starts at the front surface of the sample and the back surface remains stable. For this reason, to get the stress equilibrium, the stress wave has to travel within in the sample. In addition, the incident and reflected waves contain significant amounts of oscillations, and the stress levels obtained in this case varies more than just considering the transmitter wave that basically the 3-wave analysis using the mean of the stress on both surfaces of the sample can be applied. As can be seen in Figure 3.14, the average of the 1-wave and 2-wave analysis is a 3-wave analysis. The results of 1, 2 and 3-wave analysis are quite different in these tests where pulse shaper is not used.

In Figure 3.15, high-speed camera records of the concrete test without pulse shaper was presented. In high-speed camera recordings, the bar on the right of the sample, the incident bar, and the compression stress wave is transmitted to the sample through this bar. In other words, the stress wave is moving from right to left. As the stress wave begins to propagate in the sample, axial and radial crack formation occurs in the sample together with the deformation and the progress of the time together with the fracture of the concrete specimen.

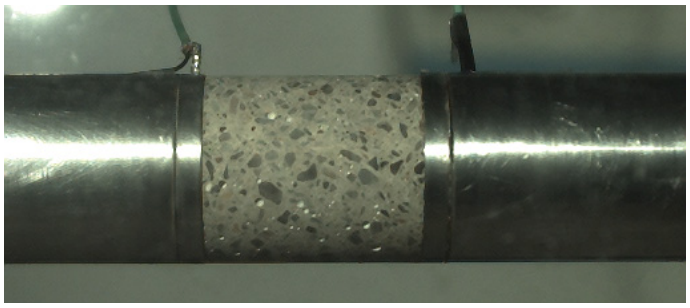

0 microsecond

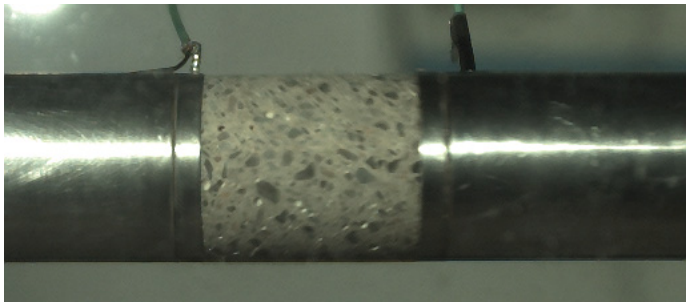

60 microseconds

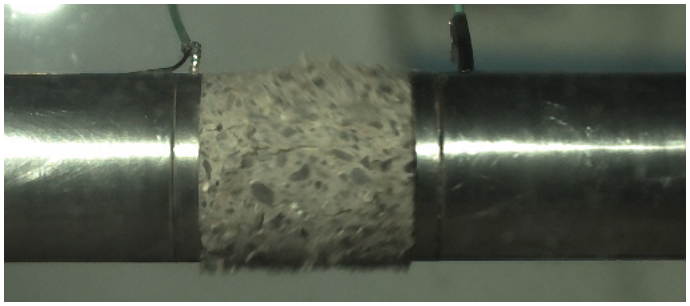

135 microseconds

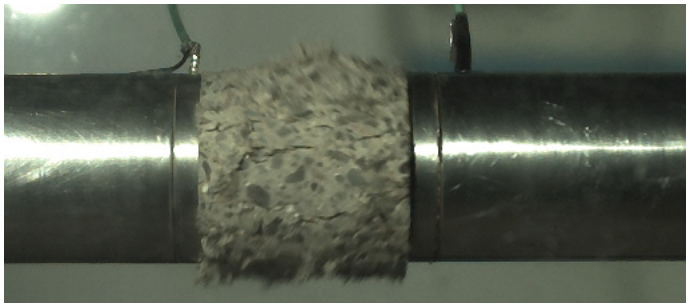

200 microseconds

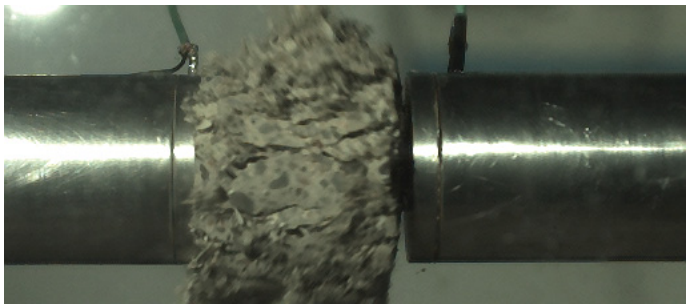

600 microseconds

Figure 3.15. Damage History from SHPB test from High-Speed Camera (15000fps)
R Parameter

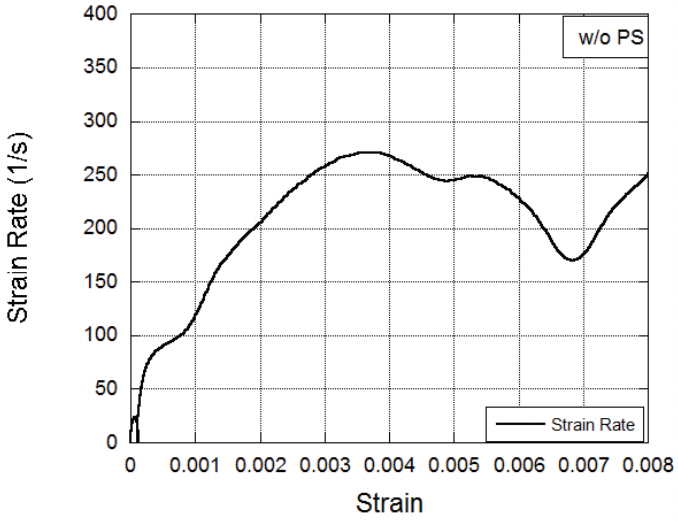

(a)

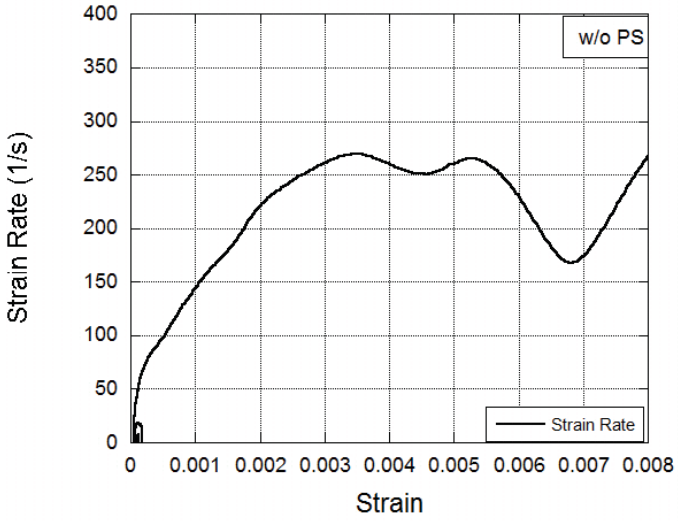

(b)

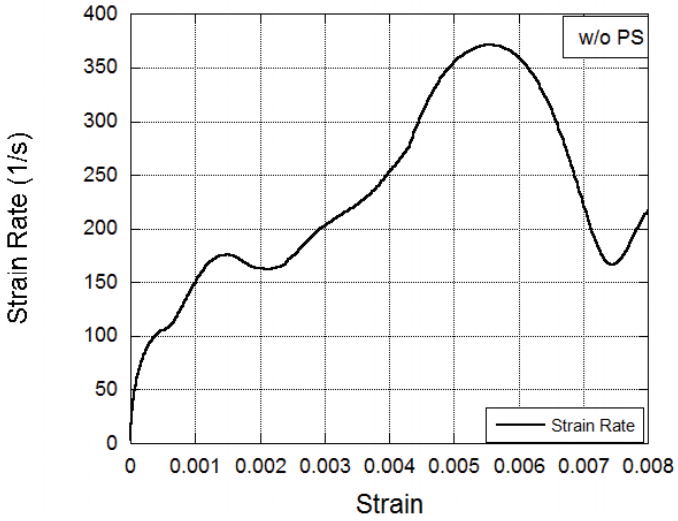

(c)

Figure 3.16. Strain Rate – Strain Curves for without Pulse Shaper Tests

Strain rate shows a sudden increase with the beginning of deformation as can be seen in Figure 3.16. Such sudden increases in strain rate for a brittle material such as concrete increase the likelihood of premature fracture of the samples without stress equilibrium. In experiments, the rate of increase of the strain rate is maintained at constant and lower levels, increasing the success in the tests of brittle materials. The use of the pulse shaper will be used to reduce the rate of strain rate increase and to keep it at fixed levels.

SHPB tests were continued with pulse shaper (with PS) tests using EPDM rubber pulse shaper as mentioned in Chapter 2. A typical signal history obtained from the strain gauges placed on the bars is shown in Figure 3.17.

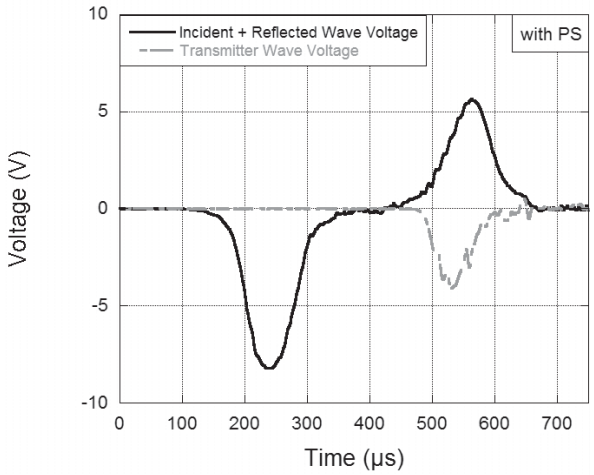

Figure 3.17. Typical SHPB strain gages measurements as a function of time for with Pulse shaper tests

Similar calculations have been made as above to obtain the stress history in the bars, Figure 3.18.

As described in detail earlier, the 1, 2 and 3-wave analysis are given in Figure 3. when using a pulse shaper in SHPB tests. When Figure 3.14 and Figure 3. are compared, it was found that the stress-strain curves obtained as a result of 1, 2 and 3-wave analysis are very close to each other and give similar results in with pulse shaper tests. This again confirms that the stress equilibrium in the sample is more quickly reached and that this condition is preserved throughout the deformation.

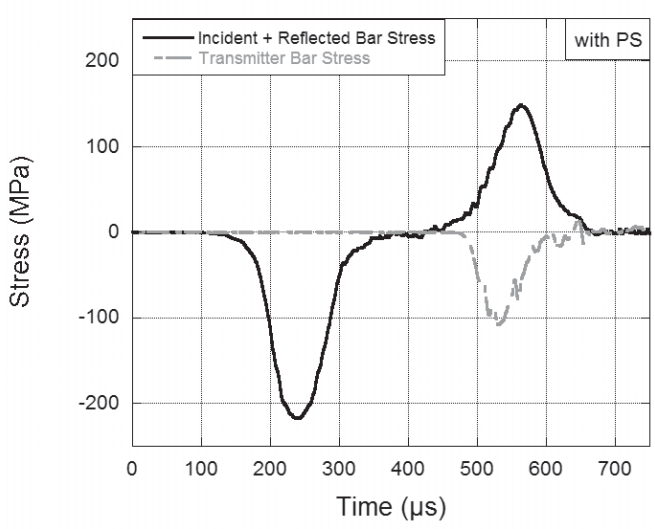

(a)

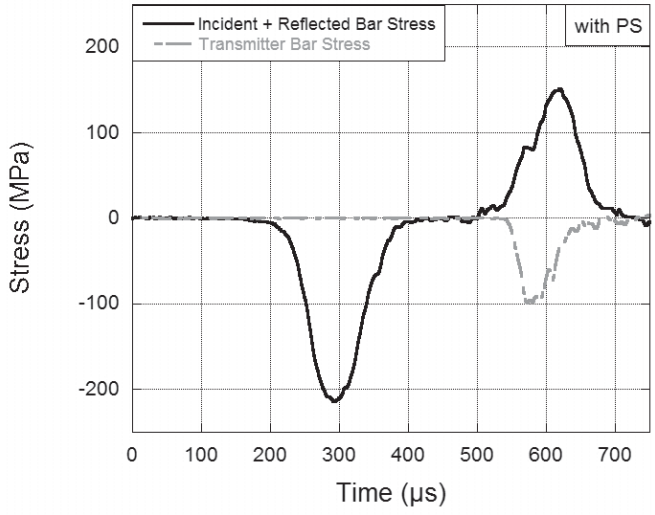

(b)

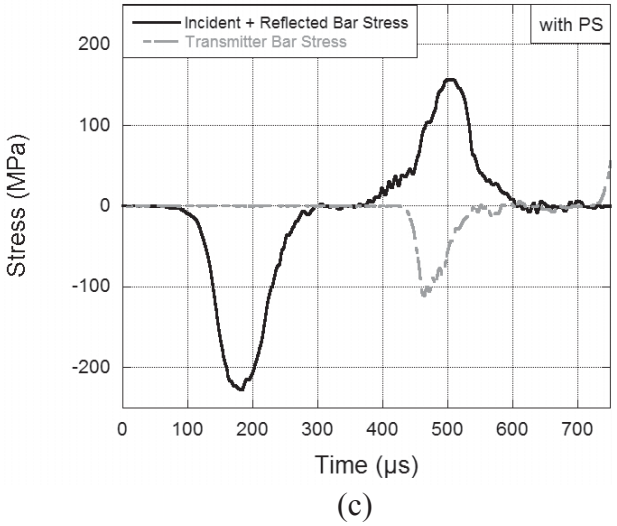

(c)

Figure 3.18. With Pulse Shaper SHPB tests (a-e) Bar stress - time histories.

(cont. on next page)

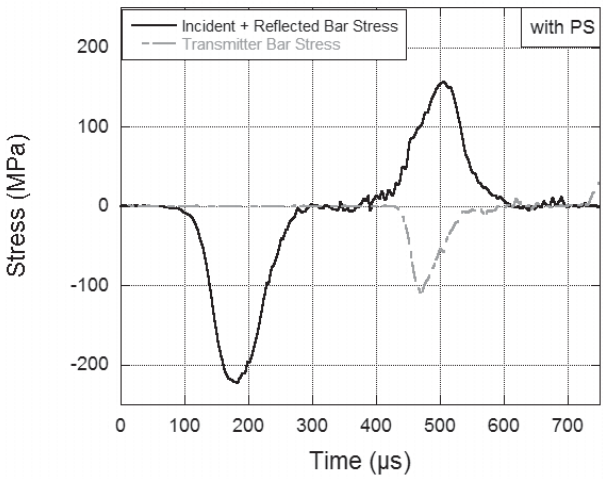

(d)

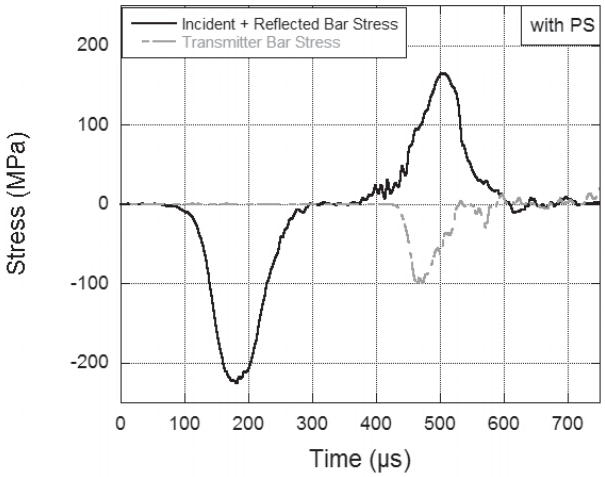

(e)

Figure 3.18. (cont.)

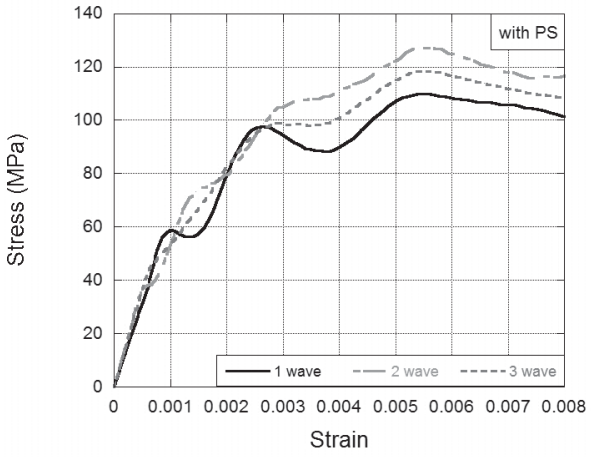

(a)

Figure 3.19. 1-wave, 2-wave, 3-wave Stress - Strain Curves for with Pulse Shaper Tests

(cont. on next page)

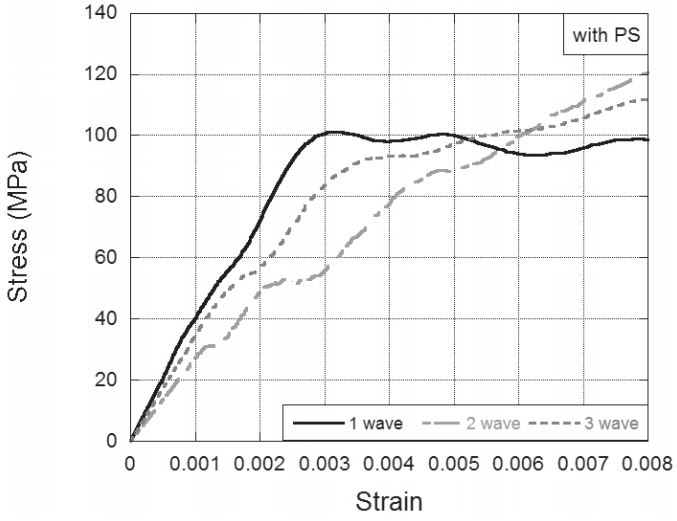

(b)

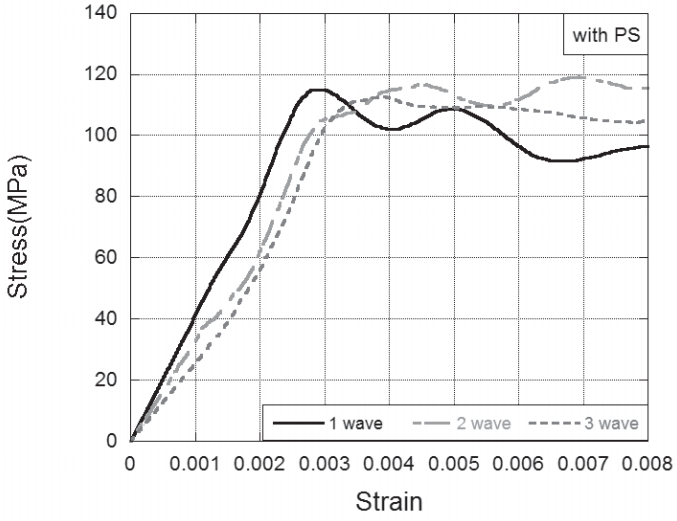

(c)

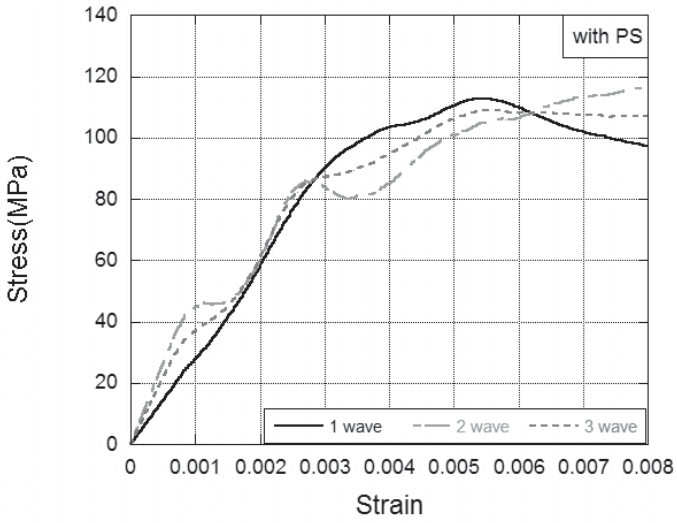

(d)

Figure 3.19. (cont.)

(cont. on next page)

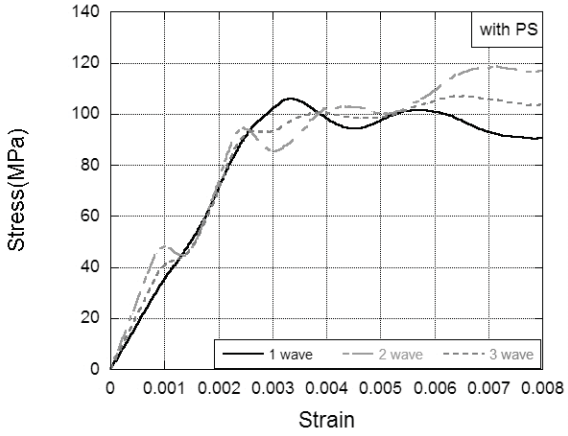

(e)

Figure 3.19. (cont.)

In Figure 3.20, strain rate versus strain is plotted. the rate of strain rate increase decreases and remains almost constant during deformation. This helps to provide stress equilibrium and prevent premature failure in brittle concrete specimens.

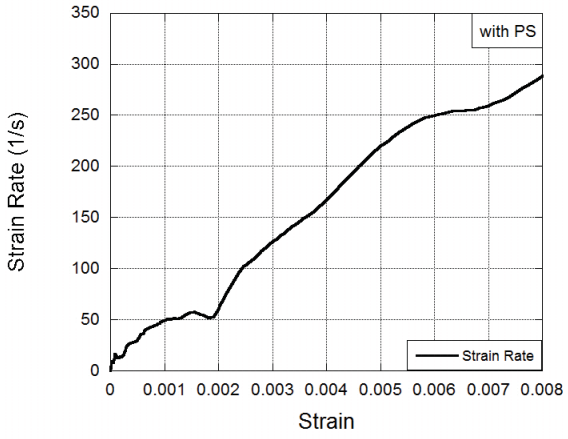

(a)

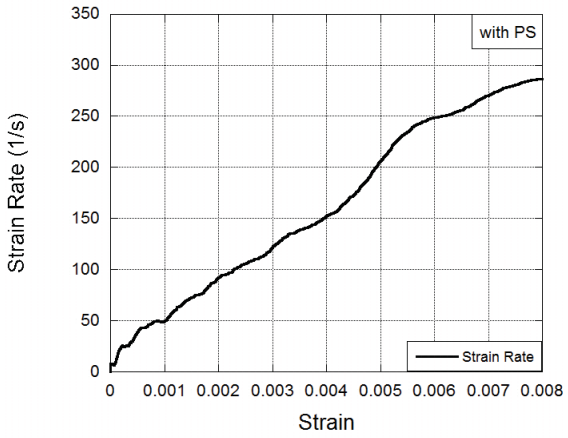

(b)

Figure 3.20. Strain Rate – Strain Curves for with Pulse Shaper Tests (a-e)

(cont. on next page)

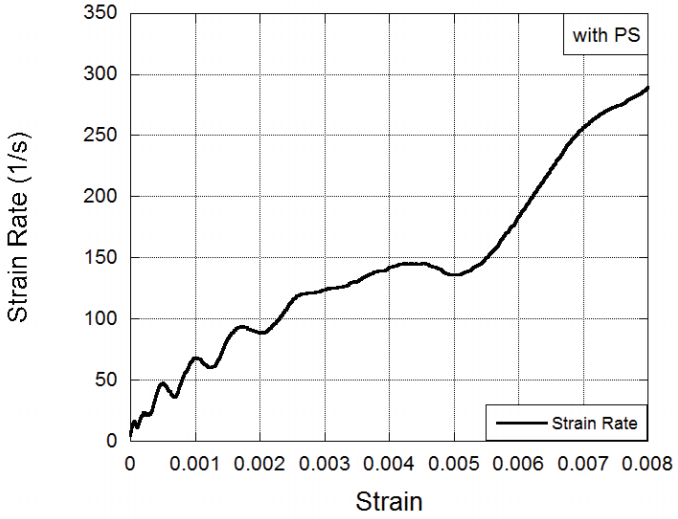

(c)

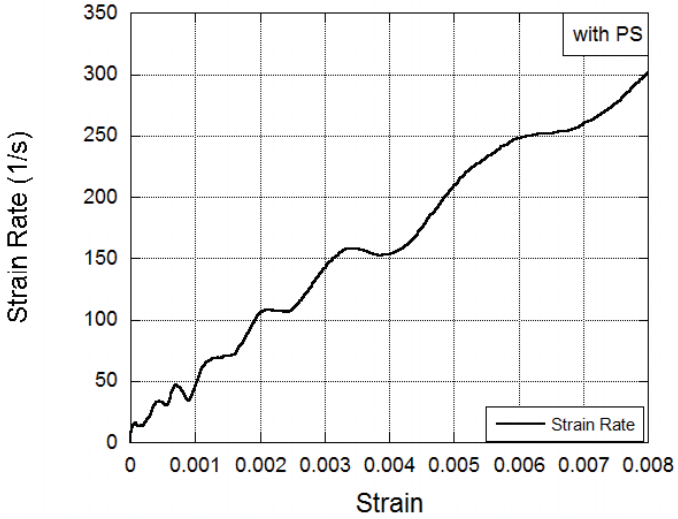

(d)

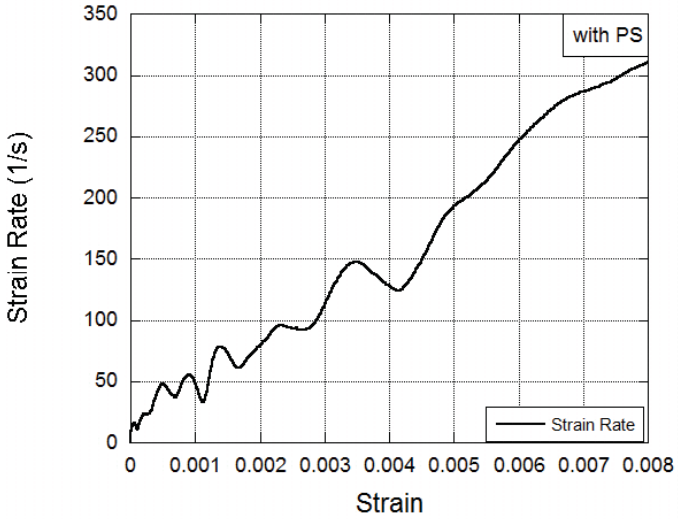

(e)

Figure 3.20. (cont.)

In the case of using the pulse shaper, it is seen that the oscillation in the incident stress wave is greatly reduced in comparison with the oscillation in the case of not being used and a very clean (noiseless) signal is transmitted to the sample, Figure 3.21. Similarly, the amount of oscillations in the reflected and transmitted signals is also considerably reduced. In case of using a pulse shaper, the decrease in the rate of increase of tension is seen in Figure 3.21. As mentioned earlier, reduces the tendency of premature failure in brittle character materials and accelerates the formation of stress equilibrium in the sample. Thus, it is possible to make accurate and precise measurements.

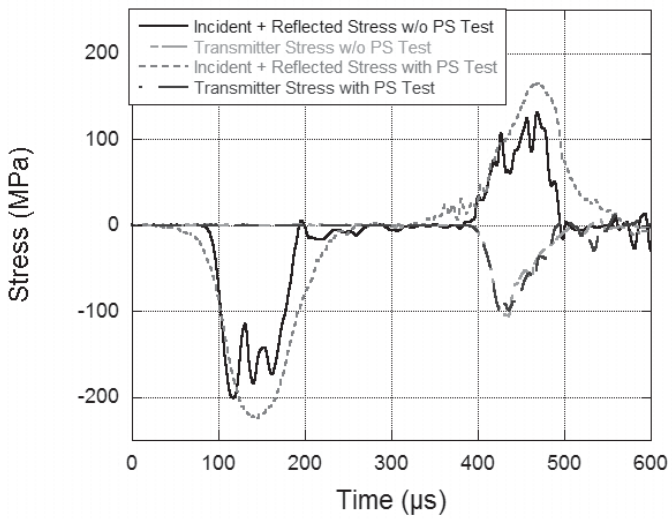

Figure 3.21. Bar Stress – Time history for comparison of with and w/o pulse shaper tests

When 1, 2, and 3-wave analysis are examined separately, along with Pulse Shaper tests and without Pulse Shaper tests; In the 1-wave analysis, the difference is small in the peak stress values, and in the 2-wave analysis, the difference in stress and strain values are clearly observed because of the force value in the front surface of the sample and due to the loading rate of the incident stress. In the 3-wave analysis, the sample gives the mean of the front and back surface, and the effect of the difference in 2-wave analysis is clearly observed in Figure 3.22.

In Figure 3.23 strain rate – strain values of with PS and without PS tests are compared. By the help of pulse shaper, increasing rate of the strain rate value is decreased that dramatically increasing strain rate may cause premature failure in the concrete specimen.

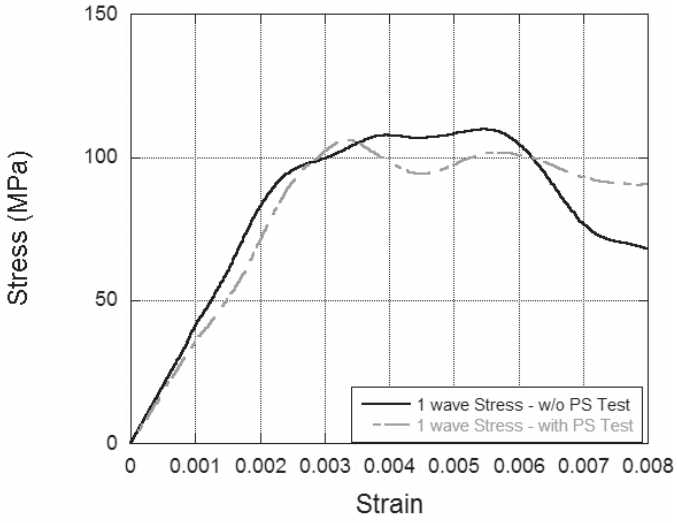

(a)

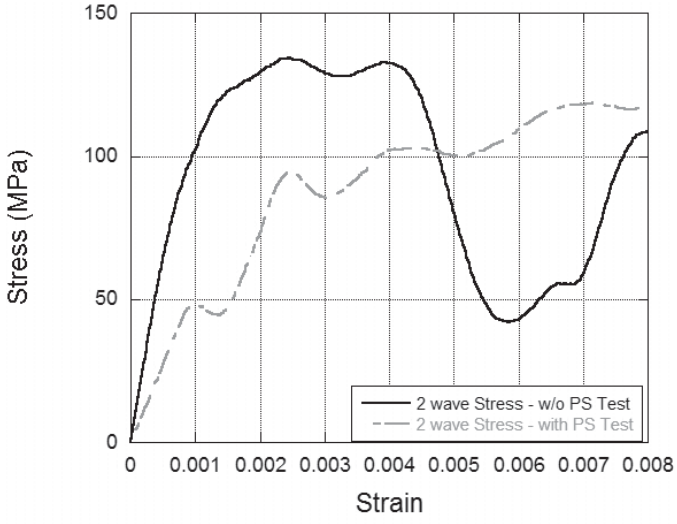

(b)

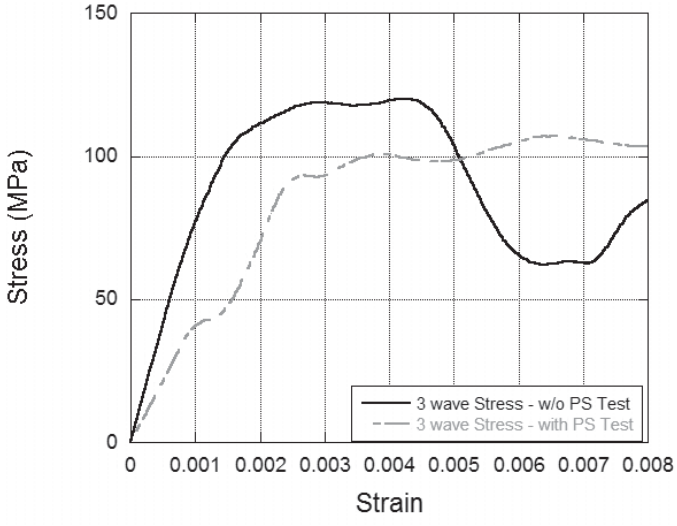

(c)

Figure 3.22. 1, 2, 3-wave stress – strain comparison of with and w/o pulse shaper tests (a-c)

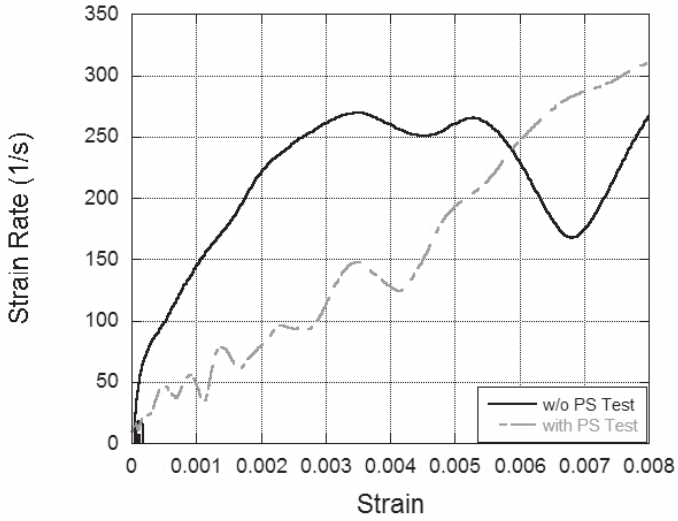

Figure 3.23. Comparison of the strain rate results of tests with PS tests and without PS tests

The effect of pulse shaper on the stress equilibrium parameter, R is presented in Figure 3.24. Stress equilibrium can be obtained from R parameter, which value reaches zero. It can be seen in the figure that "R parameter with PS test" indicates better stress equilibrium result.

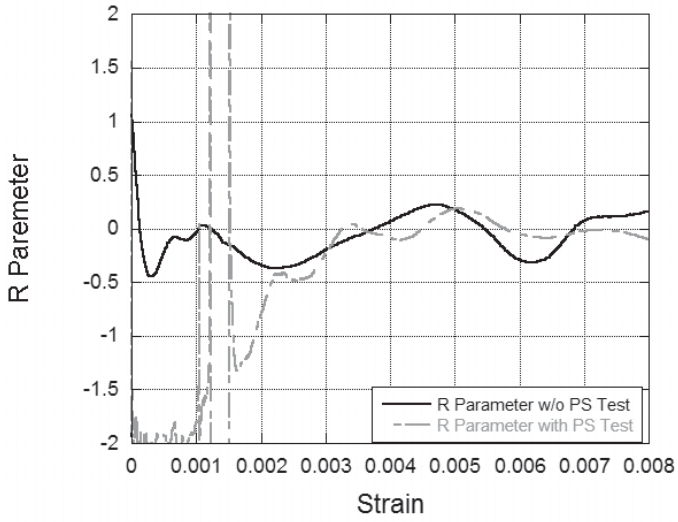

Figure 3.24. Comparison of the R parameter results of tests with PS tests and without PS tests

Overall the high strain rate test results are shown in Table 3.1. High strain rate tests without pulse shaper are conducted at 20 m/s average striker bar velocity, while with pulse shaper tests are attended at 28 m/s average bar velocity. Striker bar velocity is adjusted considering the plastic deformation of the EPDM pulse shaper material that allows close strain rate value to be achieved. Failure stress values without pulse shaper tests are 110 MPa average, while with the pulse shaper tests average result is 101 MPa.

Table 3.1. High Strain Test Results

Test Number #	*Failure Strain*	*Failure Stress (MPa)*	*Strain Rate (s-1)*	*Elastic Modulus (MPa)*
w/o PS Test – 1	0.0048	111	244	40.9
w/o PS Test – 2	0.0045	106	250	42.9
w/o PS Test – 3	0.0038	122	248	36.14
with PS Test – 1	0.0045	99	192	39.6
with PS Test – 2	0.0045	99.2	175	36.8
with PS Test – 3	0.0048	105	141	41.2
with PS Test – 4	0.0042	104	155	32
with PS Test – 5	0.0044	95	140	37

3.2 Numerical Results

3.2.1 High Strain Rate Validation Results

In this section, the validation of the dynamic tests described in the previous section with the numerical model is investigated. A numerical model of the SHPB test setup was constructed and the desired curves were gathered with the obtained data. Two different models were created for cases where pulse shaper was used, and pulse shaper was not used as mentioned earlier.

Figure 3.25 shows experimental and numerical SHPB test results for without pulse shaper and with pulse shaper cases. The numerical model was able to capture experimental results quite successfully. It is seen that the intensity and amplitude of experimental and numerical incident, reflected and transmitter signals are highly consistent with each other. The ability of the numerical model to reproduce the experimental results in a very sensitive way reveals both the validity of the material model parameters and the validity of the model. From this point, it is understood that the material model and the numerical model can be used safely for different strain rates and loading conditions.

In Figure 3.26, graphs of experimental and numerical 1,2 and 3-wave stresses for both the PS state and the w / o state are observed.

Figure shows the comparison of the strain rate values obtained from the numerical model with experimental strain rate histories. As can be seen from the results, the numerical model was able to repeat the experimental results with high precision.

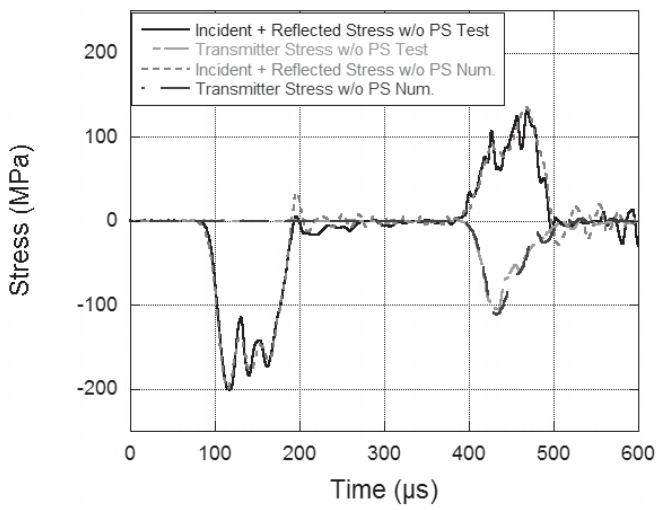

(a)

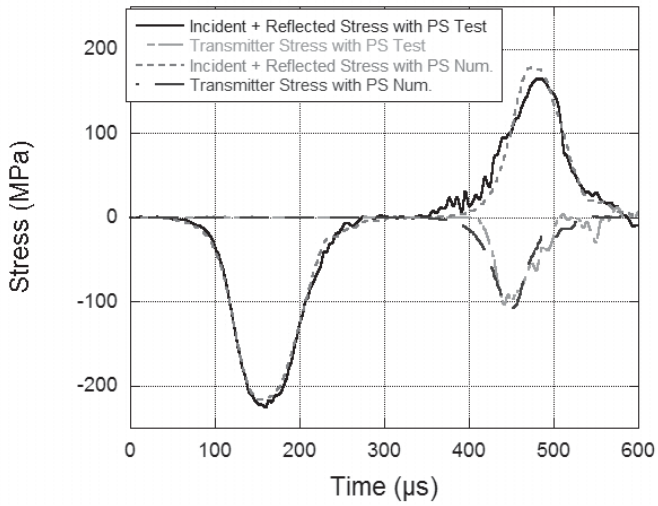

(b)

Figure 3.25. Experimental and numerical bar stress comparisons for w/o PS and with PS (a,b)

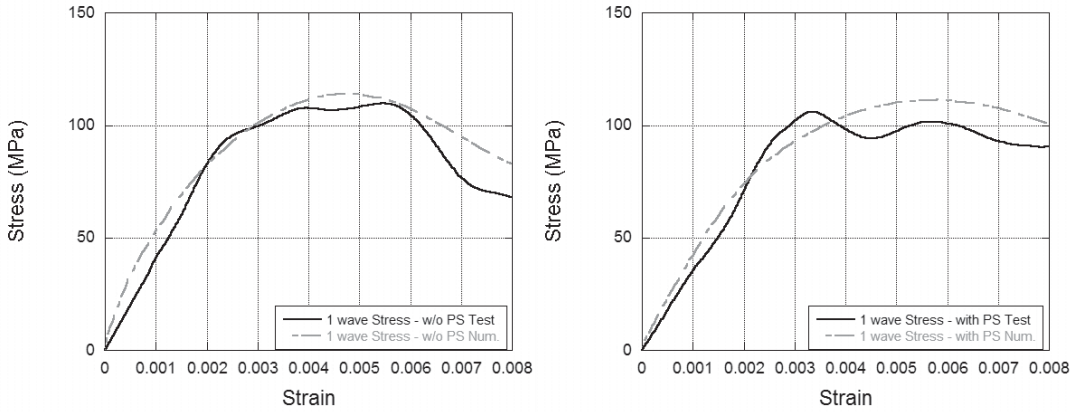

(a)

Figure 3.26. Comparison of the numerical analysis results with test results for 1, 2, 3-wave stress-strain analysis (a) 1-wave stress comparisons for w/o PS and with PS, (b) 2-wave stress comparisons for w/o PS and with PS, (c) 3-wave stress comparisons for w/o PS and with PS

(cont. on next page)

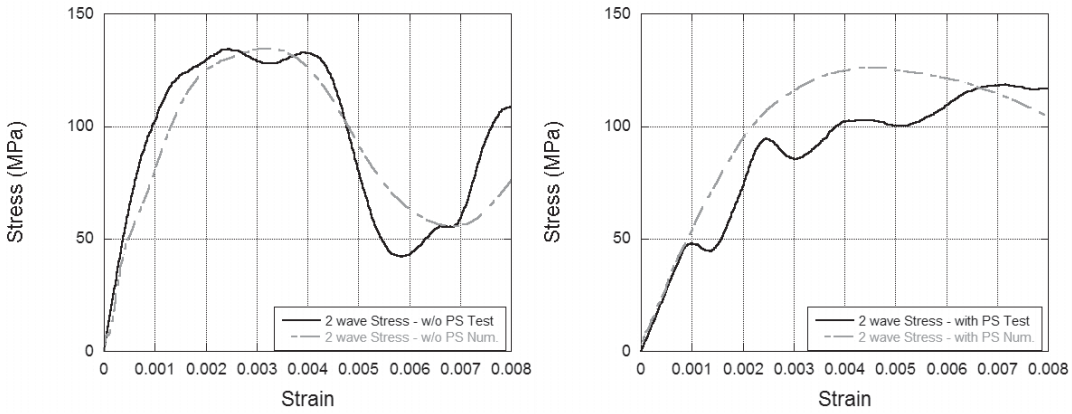

(b)

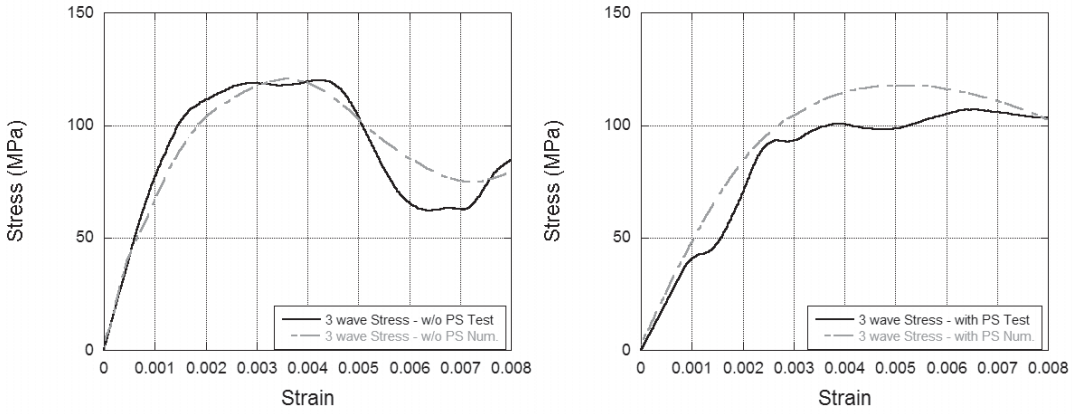

(c)

Figure 3.26. (cont.)

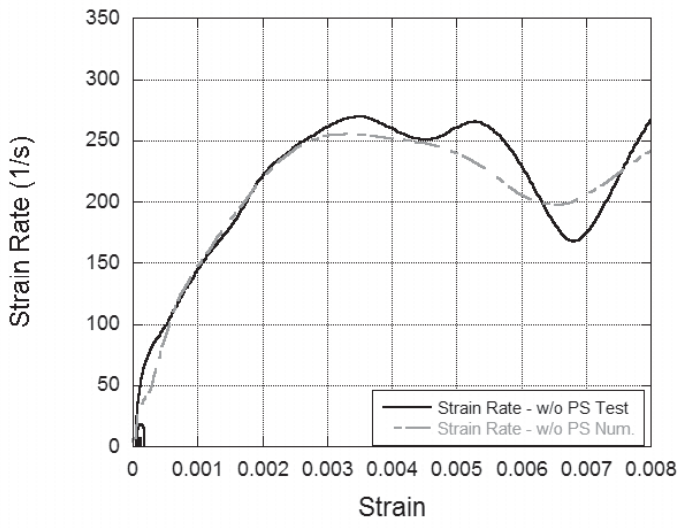

(a)

Figure 3.27. Comparison of numerical analysis results in w/o PS and with PS tests (a) Strain rate comparison for w/o PS tests, (b) Strain rate comparison for with PS tests.

(cont. on next page)

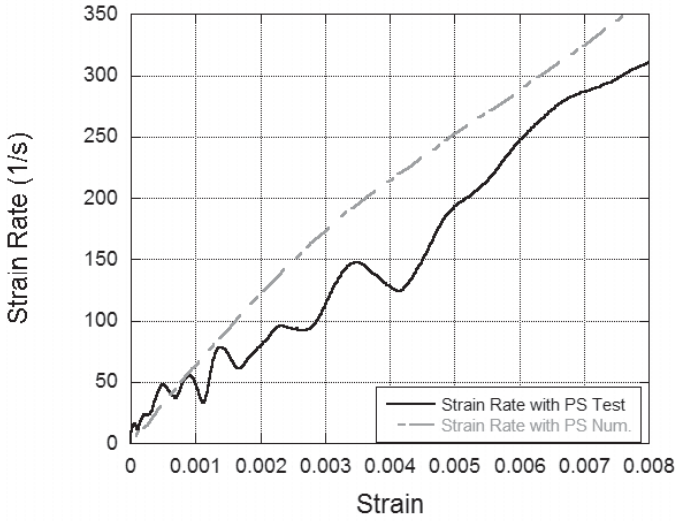

(b)

Figure 3.27. (cont.)

Cracks propagate through interfaces under static load and pass through mortar, Figure 3.28(a). For high strain rates, cracks move in a more direct way and result in the smoother path. This unsteady fracture surface contains more fractured aggregate particles than static loading, Figure 3.28(b). This has been referred to the fact that stress rapidly increased. The crack had not enough time to pass through the aggregate, on least resistance path that the stress increased sufficiently to fracture an aggregate material. As the strain rate value increases, the number of cracks will increase, so the concrete is divided into small pieces to distribute the energy. (X. Chen et al. 2013) In high strain rates, the progress of the cracks over the aggregates caused the concrete's compressive strength value to increase. Concrete is known to be a porous material with micro-cracks. Although microcracks, oriented in the axial direction are affected by tensile stress while the uniaxial quasi-static loading. Inertial effects reduced the time requirement of microcrack propagation in a rapid loading that during the high strain rate tests, concrete material’s response may have affected by the strain rate dependent behavior of microcracks. The presence of free water in micropores and its viscosity, Stefan effect, let the dynamic strength enhancement happens in concrete. (D. Zheng & Li, 2004)

The strain rate sensitivity and inertia effect acting on the sample, both experimental and numerical results were analyzed together to investigate the increase in strength depending on the strain rate of concrete samples and the reasons for this increase are presented in Figure 3.29 and Figure 3.30. When the effect of strain rate sensitivity was investigated, the numerical model analysis results show that the strain rate sensitivity parameter, C parameter, C = 0.0205 was found by subtracting the stress values against

the strain values of the analysis result where C = 0, where model does not count the strain rate sensitivity of concrete. The inertia effect was calculated by subtracting the static test stress from the stress resulting from the analysis of the C = 0 numerical model. The stress difference between quasi-static test stress and C=0 stress comes from confinement effect from the lateral inertia that may be seen as inertia effect in Figure 3.29. Figure 3.29 shows the SHPB test without pulse shaper, numerical analysis, and static test results together with the effect of strain sensitivity and inertia effect. When the inertia effect is 20 MPa at the time of static fracture, the strain rate sensitivity effect at dynamic fracture stress is about 30 MPa. The sum of strain rate effects and radial inertia effects is given as the total strength increase, shown in Figure 3.29.

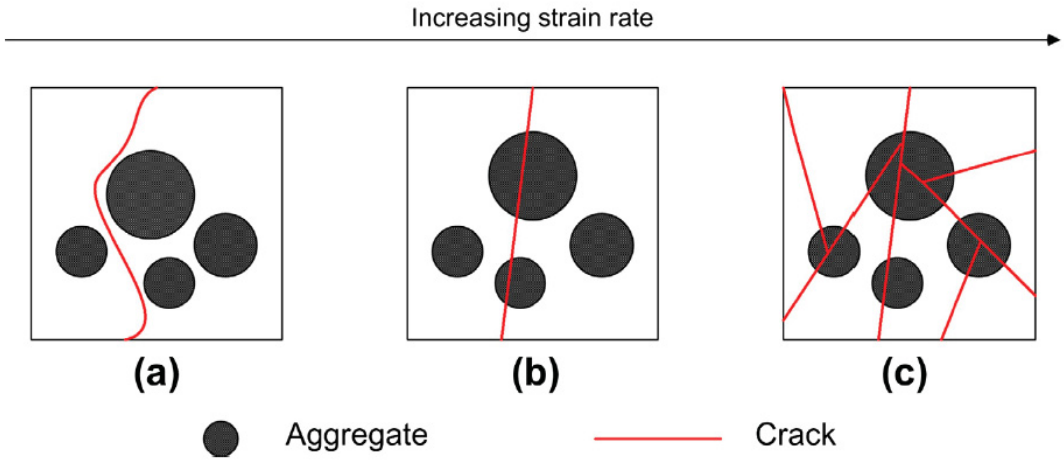

Figure 3.28. Failure pattern of concrete at different strain rates.
(X. Chen et al., 2013)

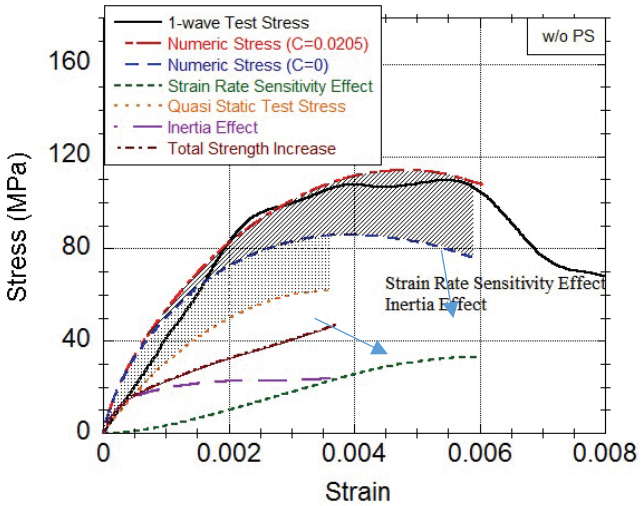

Figure 3.29. Effect of strain rate sensitivity and inertia for without pulse shaper.

In Figure 3.30, SHPB test with pulse shaper, numerical analysis and static test results together with strain rate sensitivity effect and inertia effect are presented. When the inertia effect is 20 MPa at the time of static fracture, the strain rate sensitivity effect at dynamic fracture stress is about 40 MPa.

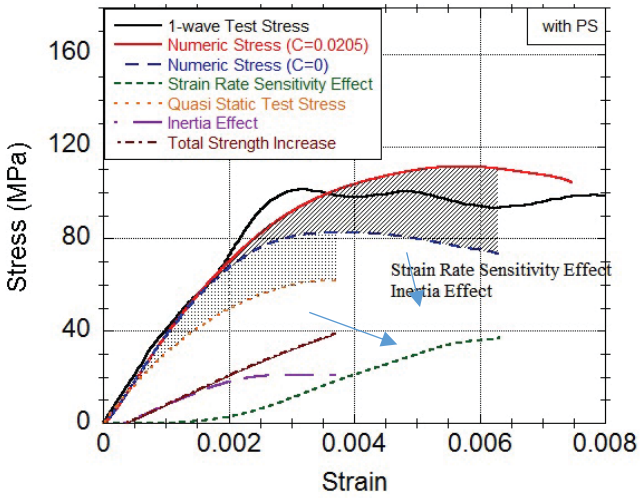

Figure 3.30. Effect of strain rate sensitivity and inertia for with pulse shaper.

The percentage increase in inertia effect and strain rate sensitivity effect on total strength increase is presented in Figure 3.31. As can be seen, when the inertia effect is dominant at low strain values, the strain rate sensitivity effect increases as the strain values increase. Moreover, as the strain value on the sample increases, the effect of inertia effect and strain rate sensitivity is balanced.

Numerical analysis of radial stress distribution is also presented in Figure 3.32. It is seen that the maximum stress on the specimen and the maximum radial stress on the specimen. It was seen that the lateral stress on the specimen was the maximum, and the maximum of the radial stress was on the specimen. At the same time, the radial stress effect of the pulse shaper was observed; as we will see in the with pulse shaper graph, the radial stress distribution difference is less than that of the without pulse shaper test.

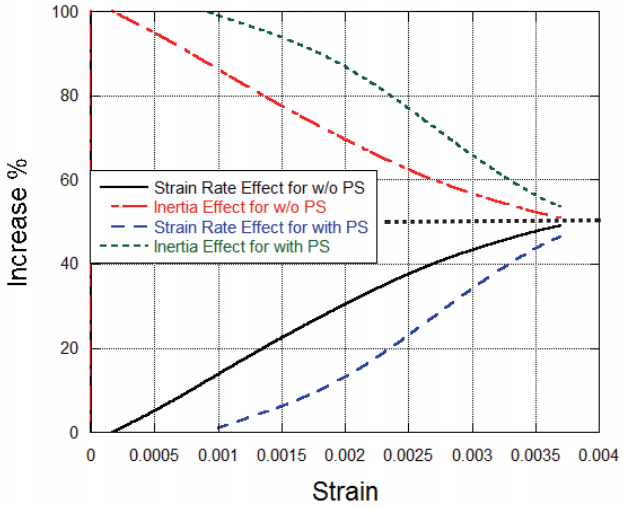

Figure 3.31. Percentage effect on total strength increase.

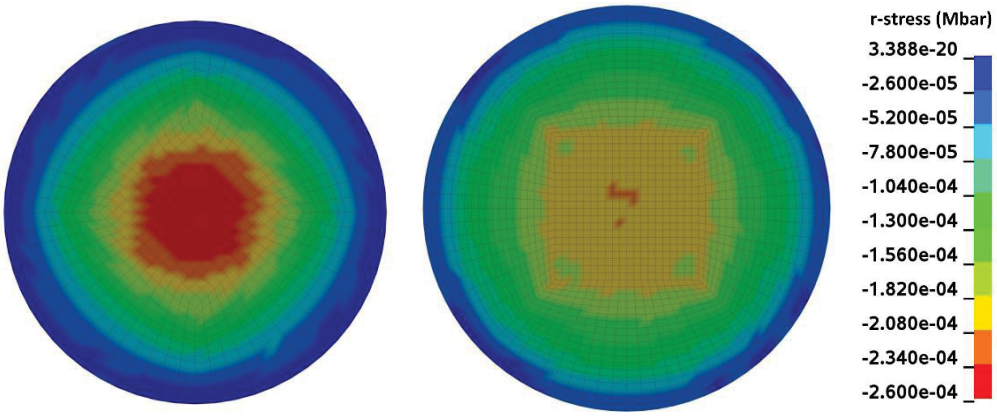

(a) (b)

Figure 3.32. Numerical analysis radial stress distribution at the bottom face of specimen: (a) w/o pulse shaper and (b) with pulse shaper.

3.2.2 Pulse Shaping at SHPB

A work that can be carried out to provide homogeneity of the stress distribution in the sample and prevent premature failure tendency in brittle materials such as concrete is to control the loading duration and shape of the incident stress wave. For this purpose, in SHPB tests, a pulse shaper was inserted on the striker bar surface of the incident bar and the plastic deformation of the pulse shaper and the loading duration of the incident stress wave were reduced. In order to investigate the efficiency of this effect, numerical stress waves in different numerical characters are defined as numerical model inputs and

the effects of these waves on specimen strain rate and R stress equilibrium parameters are investigated.

Since the bars in the test are close to the stress values and the comparison is made easier, the tensile peak value in the numerical study is also chosen as 200 MPa. In order to produce the subsequent stress wave alternatives two more parameters have been determined; these are the loading rate angle value and peak stress value time. In Figure 3.33, for example, a peak time of 40 microseconds and a loading velocity of $\theta = 40^{o}$ degrees are shown.

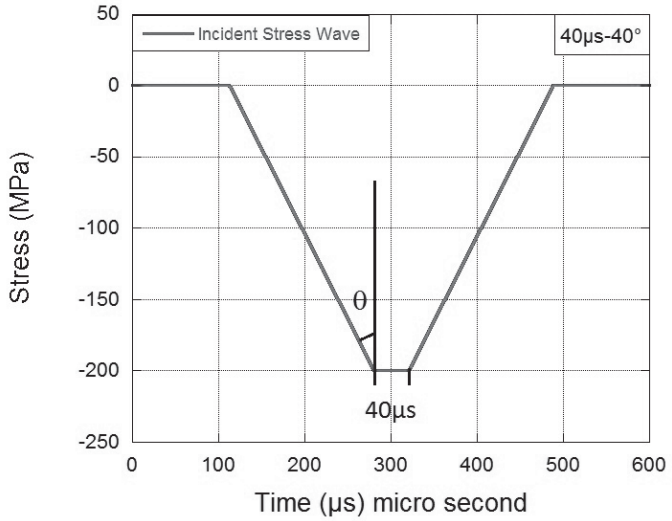

Figure 3.33. Example Incident stress - Time Graph.

Numerically generated tensile stress functions are defined as time dependent on the incident bar front surface area. The progression of these defined stress waves is gathered through the corresponding elements of the points of the strain gauges in the SHPB test setup, Figure 3.34. It should be noted that a correct SHPB test data can be obtained with the values given in this section, and no complete stress pulse formation can be observed in the stress-time graph underneath. Therefore, some graphs will not be considered because they are not valid.

The results of the modalities of the incident bar stress with loading speeds of 20, 30 and 40 ° with a peak amplitude of 0 µs is examined first. Stress waves generated on SHPB bars were observed as follows. It is seen from the Figure 3.35, elongated forms of the duration of the influence of the tensile wave which influences the sample with the growth of the incident stress loading time angle.

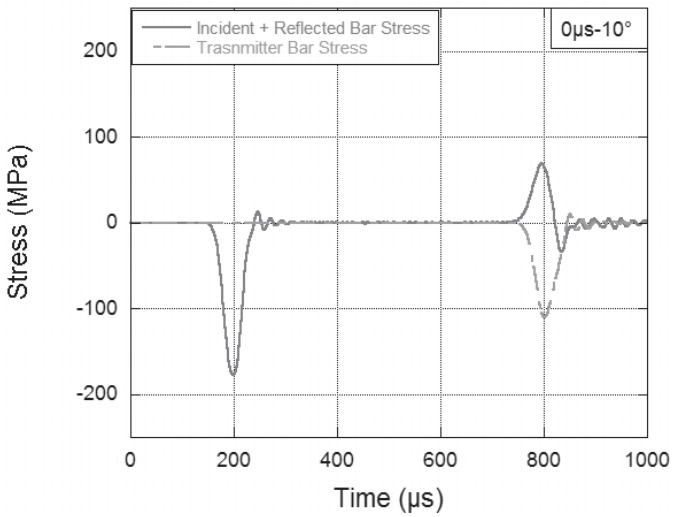

Figure 3.34. 0µs-10° Stress – Time Curve

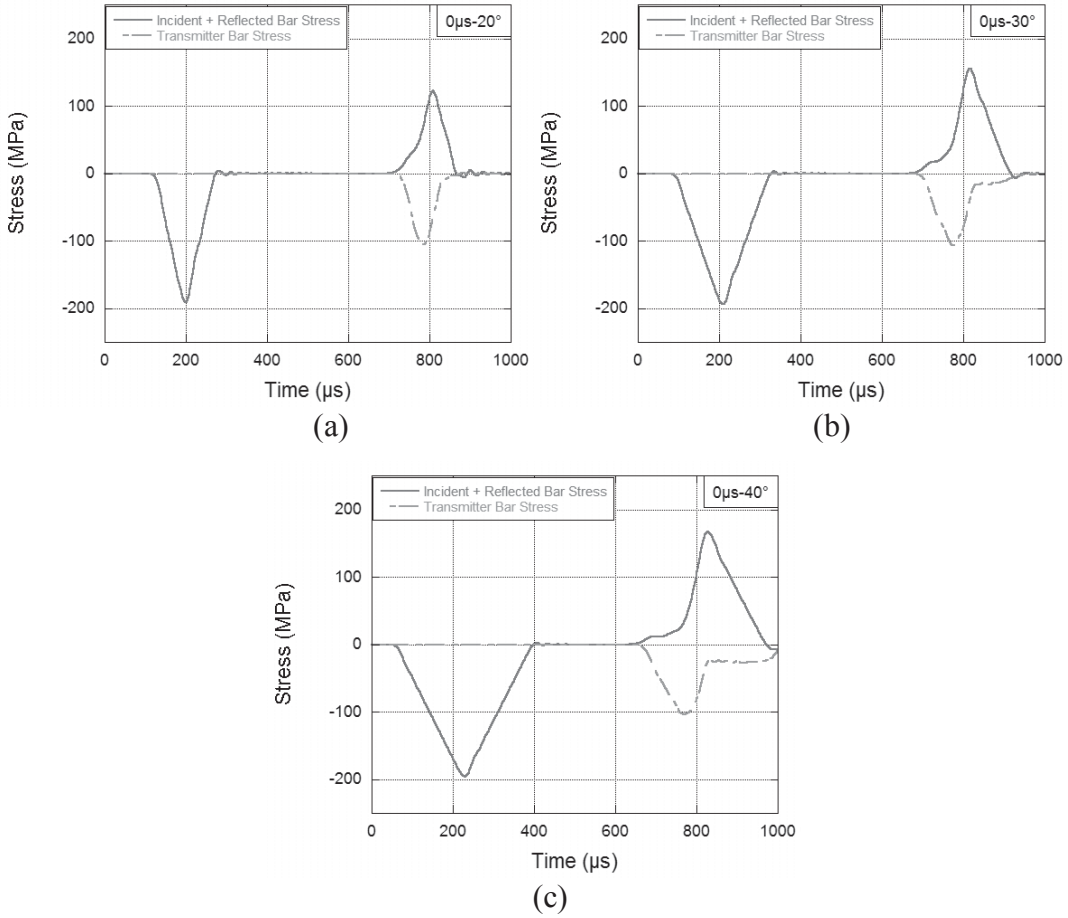

Figure 3.35. Bar Stress - Time Graphs (a) 0µs-20 ° (b) 0µs-30 ° (c) 0µs-40 °.

The 1-wave, 2-wave, and 3-wave stress-strain analysis were investigated for three different elevation angle velocities and it was observed that the 1, 2 and 3-wave stresses became closer to each other and the stress balance became more homogeneous with decreasing loading speed Figure 3.36.

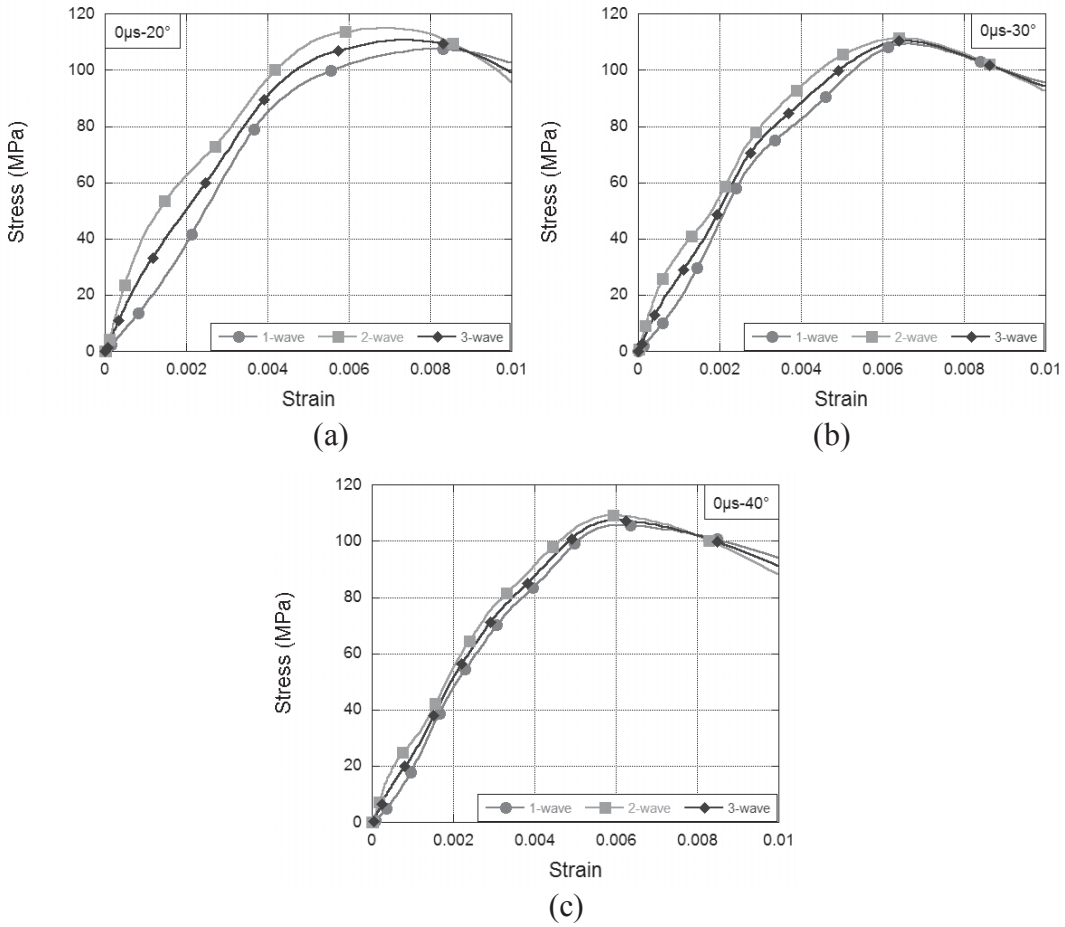

Figure 3.36. 1, 2, 3-wave Stress – Strain Curves (a) 0µs-20 ° (b) 0µs-30 ° (c) 0µs-40 °.

R stress equilibrium parameter – Strain curve shows the comparison of the R parameter obtained from the incident and transmitter bar face forces. When the offset effect of the change in angle is examined, as the angle increases, the sample is in equilibrium at lower strain values, Figure 3.37.

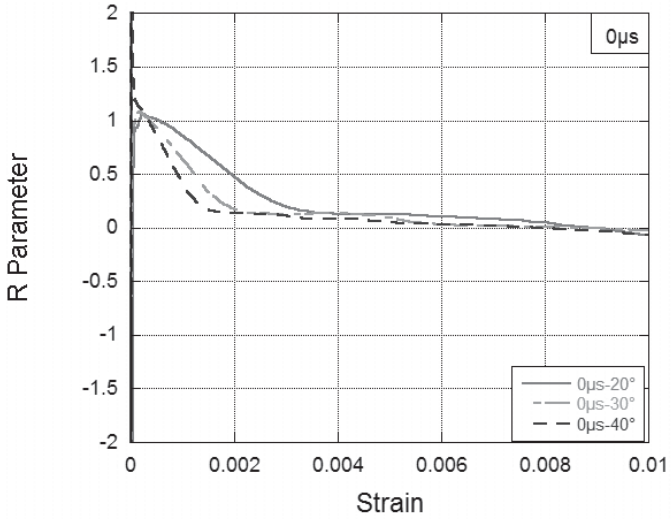

Figure 3.37. R Parameter – Strain Curve of 0µs results.

Also, as the loading angle increases, that is, as the loading speed decreases, the rate of deformation naturally decreases Figure 3.38.

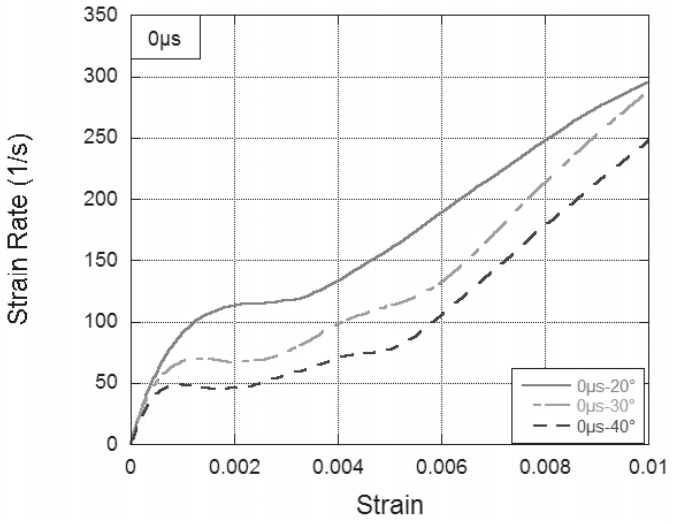

Figure 3.38. Strain Rate – Strain Curve of 0µs results.

The results of models with 20µs peak amplitude and 10 °, 20 °, 30 ° and 40 ° degrees of loading angles were then investigated. Stress history on SHPB incident and transmitter bars are observed as follows, Figure 3.39.

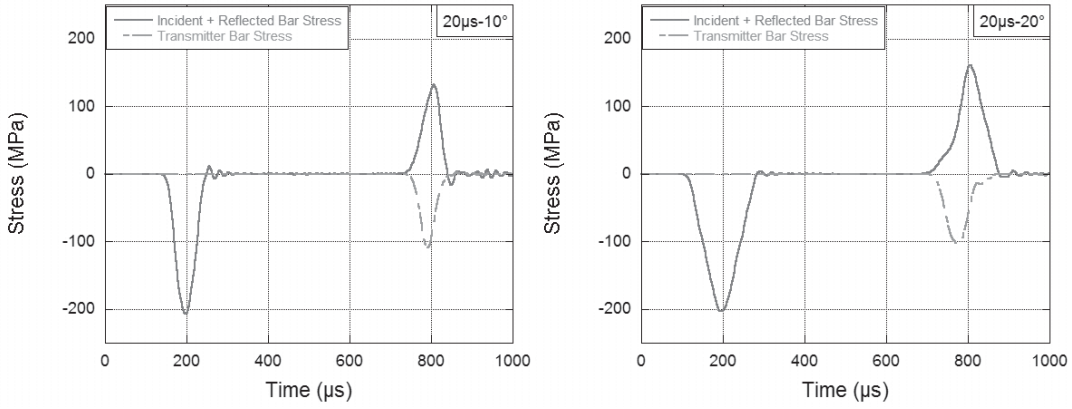

Figure 3.39. Bar Stress – Time curves (a) 20µs-10° (b) 20µs-20° (c) 20µs-30° (d) 20µs-40°.

(cont. on next page)

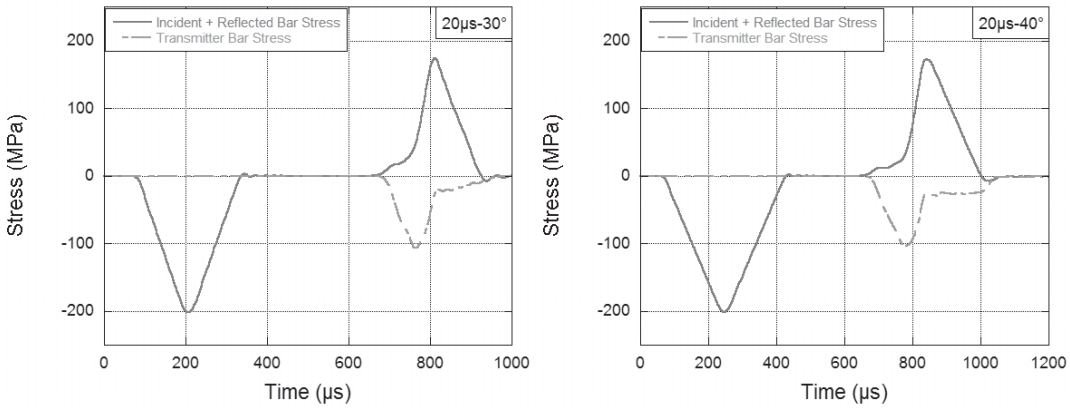

(b) (d)

Figure 3.39. (cont.)

The 1-wave, 2-wave, 3-wave Stress-Strain charts for four different elevation angles are examined below. It is seen that the increase in the angle, when reducing the rate of rising of the incident stress wave is similar to the strain values of 1,2 and 3-wave stresses. The strain value at the peak stress point towards 20µs-10° to 20µs-40° decreased from 0.0085 to 0.006 strains as seen in Figure 3.40.

R stress equilibrium parameter - strain curve shows the comparison of R parameter obtained from incident and transmitter bar forces. The influence of the changes made at the angle has been investigated. Accordingly, as the angle increases from 10° to 40°, the concrete specimen approaches the stress equilibrium at smaller strain values, Figure 3.41.

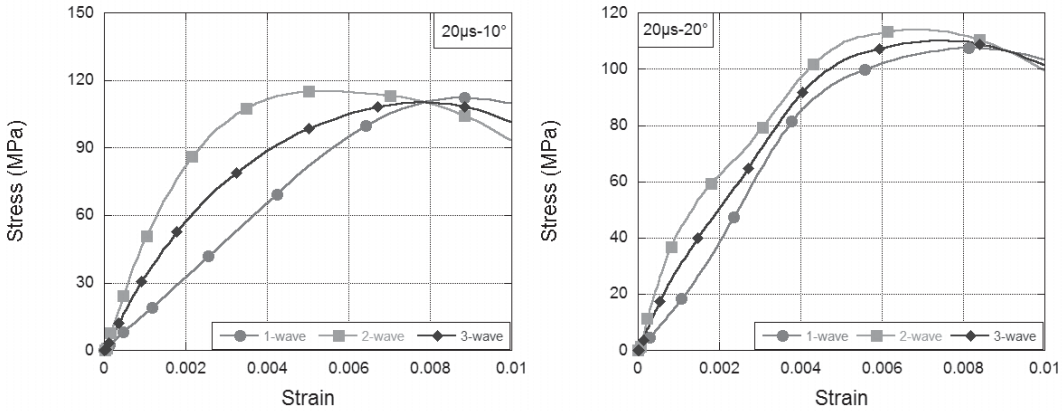

(a) (b)

Figure 3.40. 1, 2, 3-wave Stress – Strain Curves (a) 20µs-0 ° (b) 20µs-10 ° (c) 20µs-30 °, (d) 20µs-40 °.

(cont. on next page)

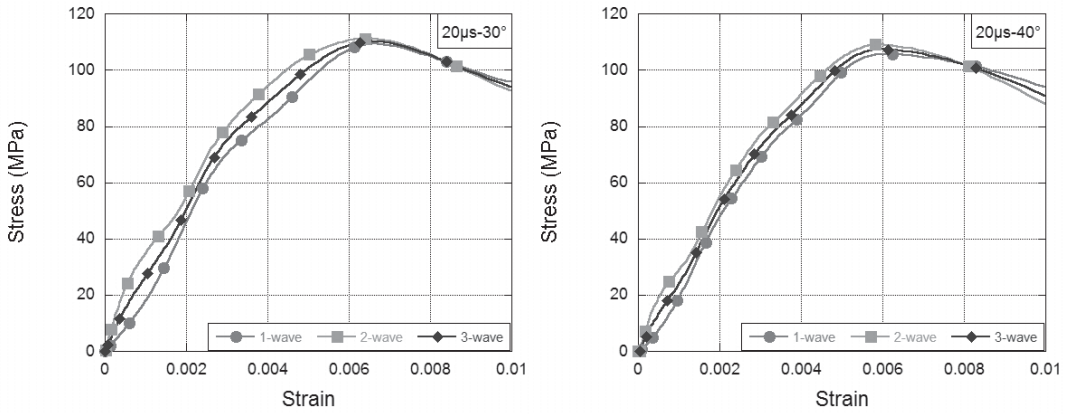

(b) (d)

Figure 3.40. (cont.)

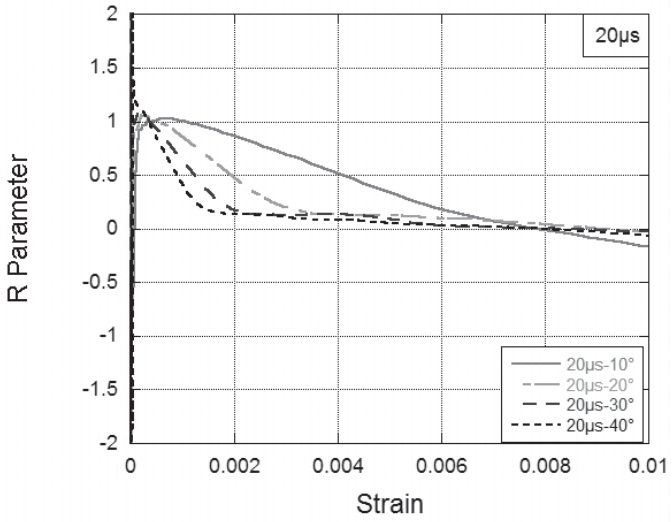

Figure 3.41. R Parameter – Strain Curve of 20µs results.

As can be seen in the Strain Rate - Strain curve that the effect of the change in the rate of rising independently of the peak amplitude at the incident stress wave is observed. So, there is a direct relationship between the rate of incident loading rise and the strain rate. As the angle increases, the strain rate decreases, Figure 3.42. Comparing these values with the strain value at the peak stress point, numerical studies have been carried out at strain rates of 310, 260, 150 and 100 1/s.

Finally, the incident stress peak amplitude is 40µs and the angle values are examined as 10, 20, 30 and 40° degrees. The stress waves on the SHPB bars are observed as follows. It is seen that the wave distribution in the bars decreases as the incident stress angle grows.

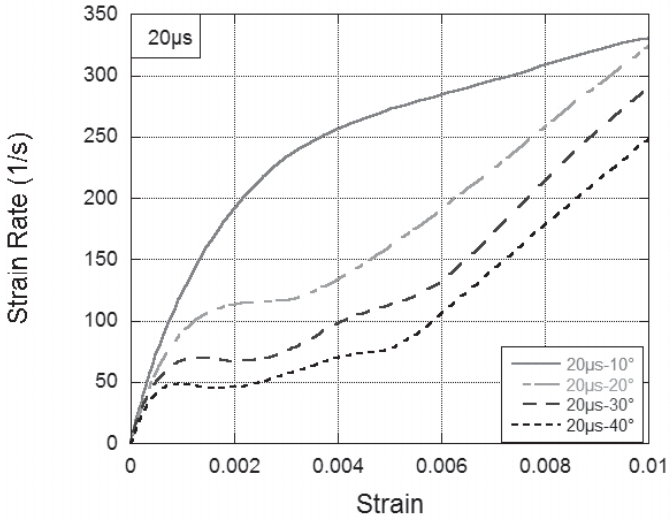

Figure 3.42. Strain Rate – Strain Curve of 20µs results.

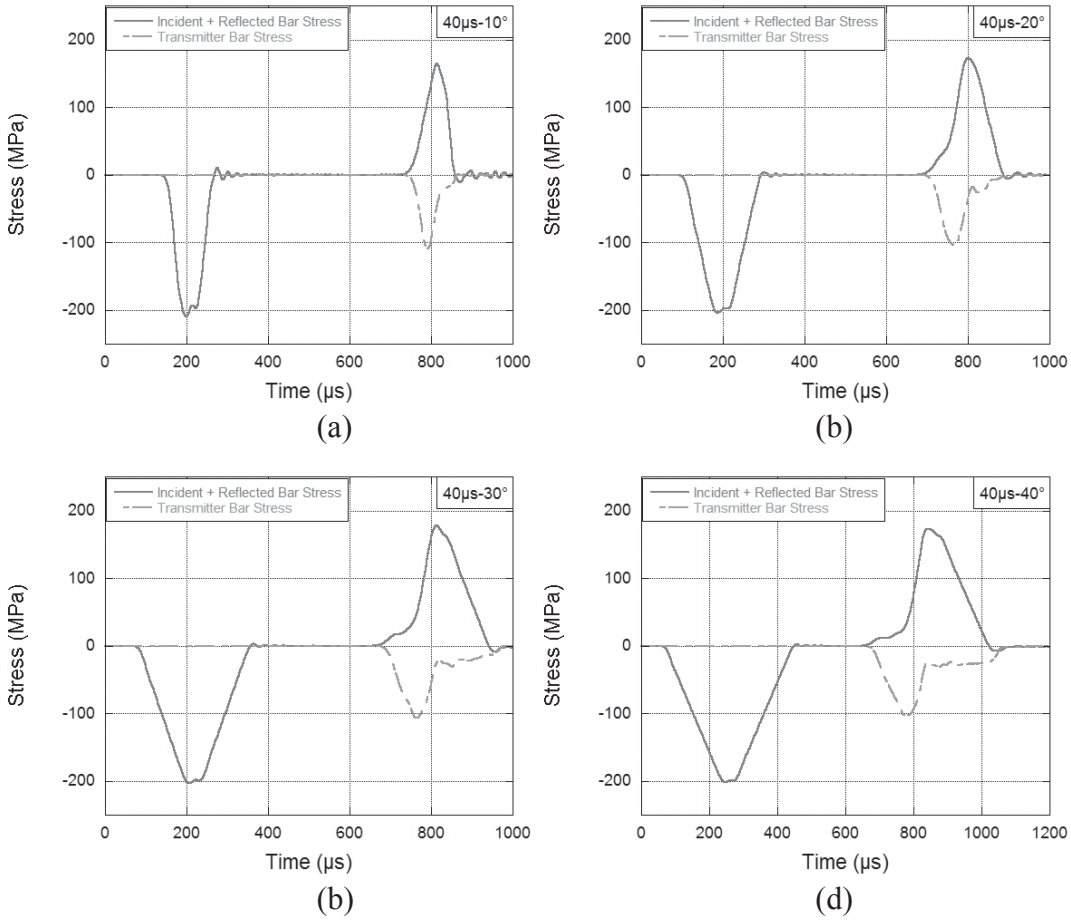

Figure 3.43. Bar Stress – Time curves (a) 40µs-10° (b) 40µs-20° (c) 40µs-30° (d) 40µs-40°.

For 40µs pulse amplitude, 1-wave, 2-wave, 3-wave Stress-strain graphs for 4 different elevation angles are examined below in Figure 3.44. Reducing the rate of incident wave rise, increase in the angle, it is seen that the 1,2 and 3-wave stresses are

similar to each other. The strain value at the peak stress point towards 20μs-10° to 20μs-40° decreased from 0.0085 to 0.006 strains, for peak stress values from 112 MPa to 105 MPa.

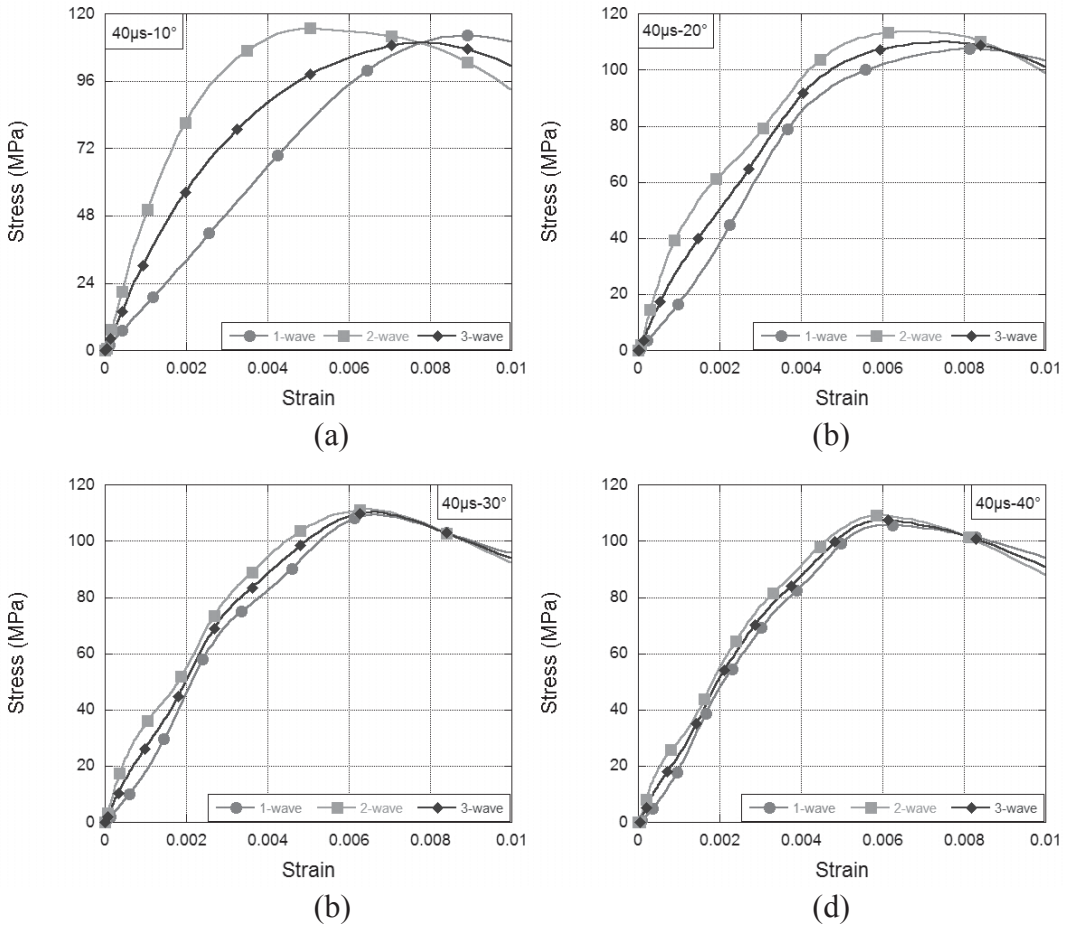

Figure 3.44. 1, 2, 3-wave Stress – Strain Curves (a) 40μs-10 ° (b) 40μs-20 ° (c) 40μs-30 °, (d) 40μs-40 °.

R stress equilibrium parameter – strain curve shows the comparison of R parameter obtained from incident and transmitter bar forces for 40μs pulse amplitude tests. As the angle increases, the concrete specimen approaches the stress equilibrium at smaller strain values, Figure 3.45.

In addition to these studies, the effect of the peak amplitude 0μs, 20μs, and 40μs of incident stress independently of angle was investigated. The effect of the change in peak amplitude on the stress, strain rate, R parameter was not observed.

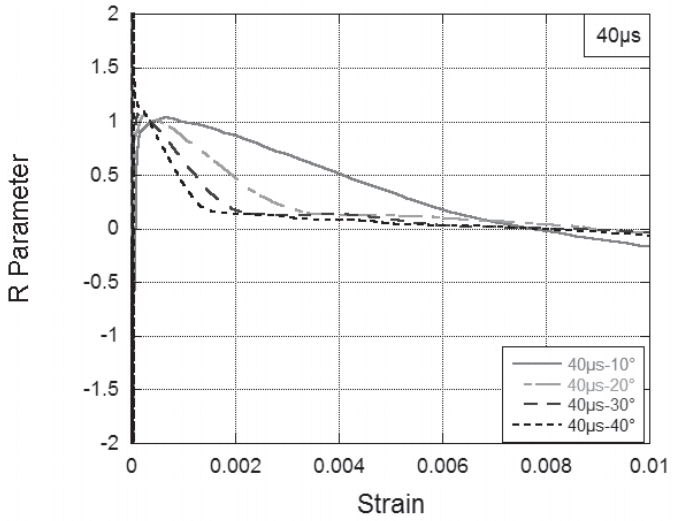

Figure 3.45. R Parameter – Strain Curve of 40µs results.

CHAPTER 4

CONCLUSION

In the current study, the effect of strain rate on the dynamic mechanical behavior of concrete was investigated through experiments and numerical simulations. Concrete material with 39.52 mm radius and 1.14 L / D ratio was produced. Experimental and numerical studies were carried out, and the following conclusions were found.

- High strain rate tests were conducted at SHPB and nearly constant strain rate was reached at these tests.

- The effect pulse shaper was examined at high strain rate test. EPDM pulse shaper was used at SHPB apparatus. Premature failure from non-equilibrated loading was avoided that the test using the pulse shaper had reached the stress-equilibrium earlier. Nearly constant strain rate was reached by the help of pulse shaper use. Repeated experiments for the effect of statistical behavior and flows have been followed more easily that more consistency was seen in the results of the tests using pulse shaper. Because of the limitations of minimum aggregate size, large bar diameter was used that the use of pulse shaper has allowed us to avoid wave dispersions. In with pulse shaper (w/ PS) tests, loading duration of incident wave increased twice as much in the without pulse shaper (w/o PS) tests was noticed.

- Some challenges were existed in using SHPB to determine material properties of the concrete material that bar end faces have to remain flat and parallel and this was achieved using inserts in the same material as the bar as seen in Figure 2.11.

- Experimental studies reveal that the compressive strength, elastic modulus and failure strain increase with increasing strain rate. The strain rate effect is more effective on the compressive stress than failure strain and elastic modulus. - -

- The average uniaxial compressive strength was 62 MPa at the lowest quasi-static strain rate and the average of dynamic compressive strength was 105.1 MPa. An average strain rate of 192 s-1 is applied to the static compressive strength of concrete specimens and shows rate sensitive behavior and strength increased almost 1.7 times. In dynamic tests, modulus of elasticity of concrete increased 1.3 times than that of the modulus of elasticity of quasi-static tests. Strain values at peak stress raised from 0.0036 at quasi-static tests to 0.0044 at high strain rate tests.

- The validation of SHPB tests performed in Ls-Dyna was presented that not only bar responses but also the 1,2 and 3-wave stress analysis, strain rate – strain curves in experimental tests and numerical simulations match up with each other.

- In numerical simulations, the positive contribution of pulse shaper to radial stress distribution was detected, more uniform distribution along the radial axis is observed.

- The percentage increase in inertia effect and strain rate sensitivity effect on total strength increase was examined and it has emerged that the inertia effect is more dominant at lower strain values, where the strain rate sensitivity effect increases as the strain values increase.

- In numerical simulations, the shape of the incident pulse was investigated by controlling the loading duration and loading velocity of the incident wave. It was found that the shape of incident wave was directly influenced by the strain rate and stress equilibrium obtained from the specimen.

REFERENCES

Abrams, D. A. (1917). Effect of rate of application of load on the compressive strength of concrete. *20Th Annual Meeting*, *17*(2), 364–377.

Bagher Shemirani, A., Naghdabadi, R., & Ashrafi, M. J. (2016). Experimental and numerical study on choosing proper pulse shapers for testing concrete specimens by split Hopkinson pressure bar apparatus. *Construction and Building Materials*, *125*, 326–336. https://doi.org/10.1016/j.conbuildmat.2016.08.045

Biffi, C. A., & Tuissi, A. (2017). Stato dell'arte sulle tecniche di produzione additiva per metalli. *Metallurgia Italiana*, *109*(1), 5–10. https://doi.org/10.1017/CBO9781107415324.004

Bischoff, P. H., & Perry, S. H. (1991). Compressive behaviour of concrete at high strain rates. *Materials and Structures*, *24*(6), 425–450. https://doi.org/10.1007/BF02472016

C. Allen Ross. (1989). Split-Hopkinson pressure bar tests, 88.

Chen, W. W., & Song, B. (2010). *Split Hopkinson*. *Springer New York Dordrecht Heidelberg London* (Vol. 1). https://doi.org/10.1007/978-1-4419-7982-7

Chen, X., Wu, S., & Zhou, J. (2013). Experimental and modeling study of dynamic mechanical properties of cement paste, mortar and concrete. *Construction and Building Materials*, *47*, 419–430. https://doi.org/10.1016/j.conbuildmat.2013.05.063

Christensen, R. J., Swanson, S. R., & Brown, W. S. (1972). Split-hopkinson-bar tests on rock under confining pressure. *Experimental Mechanics*, *12*(11), 508–513. https://doi.org/10.1007/BF02320747

Davies, R. M. (1948). A Critical Study of the Hopkinson Pressure Bar. *Philosophical Transactions of the Royal Society of London. Series A, Mathematical and Physical Sciences*, *240*(821), 375–457. https://doi.org/10.2307/91440

Ellwood, S., Griffiths, L. J., & Parry, D. J. (1982). Materials testing at high constant strain rates. *Journal of Physics E: Scientific Instruments*, *15*(3), 280. https://doi.org/10.1088/0022-3735/15/3/009

Erdogan, T. Y. (2013). *Beton* (2nd Editio). ODTU Gelistirme Vakfi.

Follansbee, P. (1995). The Hopkinson bar, Mechanical Testing. In *ASM Handbook, ASM Int* (pp. 198–203).

Frantz, C., & Bar, H. P. (2014). Wave Propagation in the Split, *105*(January 1983), 61–66.

Frew, D. J., Forrestal, M. J., & Chen, W. (2002). Pulse shaping techniques for testing brittle materials with a split Hopkinson pressure bar. *Experimental Mechanics*,

42(1), 93–106. https://doi.org/10.1007/BF02428192

Gama, B. A., Lopatnikov, S. L., & Gillespie, J. W. (2004). Hopkinson bar experimental technique: A critical review. *Applied Mechanics Reviews*, *57*(4), 223. https://doi.org/10.1115/1.1704626

Gama, B. a, Lopatnikov, S. L., & Gillespie, J. W. (2004). Hopkinson bar experimental technique: A critical review. *Applied Mechanics Reviews*, *57*(4), 223. https://doi.org/10.1115/1.1704626

Gary, G., & Bailly, P. (1998). Behaviour of quasi-brittle material at high strain rate. Experiment and modelling. *European Journal of Mechanics - A/Solids*, *17*(3), 403–420. https://doi.org/10.1016/S0997-7538(98)80052-1

Gerlach, R., Sathianathan, S. K., Siviour, C., & Petrinic, N. (2011). A novel method for pulse shaping of Split Hopkinson tensile bar signals. *International Journal of Impact Engineering*, *38*(12), 976–980. https://doi.org/10.1016/j.ijimpeng.2011.08.007

Gray, G. (2000). Classic Split-Hopkinson Pressure Bar Testing. *Materials Park, OH: ASM International, 2000.*, *8*, 462–476. https://doi.org/10.1361/asmhba0003296

Grote, D. L., Park, S. W., & Zhou, M. (2001). Dynamic behavior of concrete at high strain rates and pressures: I. experimental characterization. *International Journal of Impact Engineering*, *25*(9), 869–886. https://doi.org/10.1016/S0734-743X(01)00020-3

Hallquist, J. O. (2006). *Theory manual*. *Livermore Software Technology Corporation*.

Holmquits, T. J., Johnson, G. R., & Cook, W. H. (1993). A Computational Constitutive Model for Concrete Subjected to Large Strains, High Strain Rates, and High Pressures. In *14th International Symposium on Ballsitics*. Quebec City.

Hopkinson, B. (1914). A method of measuring the pressure produced in the detonation of high explosives or by the impact of bullets. *Philos. Trans. R. Soc. London, Ser. A*, (213), 437–456.

Hopkinson, J. (1872). On the rupture of an iron wire by a blow. *J. Proc. Manchest. Liter. Philos. Soc*, *11*.

Kolsky, H. (1949). An investigation of the mechanical properties of materials at very high rates of loading. *Proceedings of the Physical Society. Section B*, *62*(11), 676–700. https://doi.org/10.1088/0370-1301/62/11/302

Krafft, J. M., Sullivan, A. M., & Tipper, C. F. (1954). The effect of static and dynamic loading and temperature on the yield stress of iron and mild steel in compression. *Proc. Roy. Soc, London*, *A221*, 114–127.

Li, W., & Xu, J. (2009). Impact characterization of basalt fiber reinforced geopolymeric concrete using a 100-mm-diameter split Hopkinson pressure bar. *Materials Science and Engineering A*, *513–514*(C), 145–153. https://doi.org/10.1016/j.msea.2009.02.033

Li, X. B., Lok, T. S., Zhao, J., & Zhao, P. J. (2000). Oscillation elimination in the Hopkinson bar apparatus and resultant complete dynamic stress-strain curves for rocks. *International Journal of Rock Mechanics and Mining Sciences*, *37*(7), 1055–1060. https://doi.org/10.1016/S1365-1609(00)00037-X

Lindholm, U. S. (1964). Some experiments with the split hopkinson pressure bar∗. *Journal of the Mechanics and Physics of Solids*, *12*, 317–335. https://doi.org/10.1016/0022-5096(64)90028-6

Lv, T. H., Chen, X. W., & Chen, G. (2017). Analysis on the Waveform Features of the Split Hopkinson Pressure Bar Tests of Plain Concrete Specimen. *International Journal of Impact Engineering*, *103*, 107–123. https://doi.org/10.1016/j.ijimpeng.2017.01.004

Malvern, L. E., Jenkins, D. A., Tang, T., & Ross, C. A. (1985). DYNAMIC COMPRESSIVE TESTING OF CONCRETE Lawrence E. Malvern, David A. Jenkins, Tianxi Tang, and C. Allen Ross Engineering Sciences Department, University of Florida Gainesville, Florida 32611. In *Proceedings of Second Symposium on the Interaction of Non-Nuclear Munitions with Structures* (pp. 194–199). Retrieved from www.dtic.mil/dtic/tr/fulltext/u2/a160778.pdf

Manual, K. U. S. (2007). *Keyword User ' S Manual* (Vol. I).

Nemat-Nasser, S., Isaacs, J. B., & Starrett, J. E. (1991). Hopkinson Techniques for Dynamic Recovery Experiments. *Proceedings of the Royal Society A: Mathematical, Physical and Engineering Sciences*, *435*(1894), 371–391. https://doi.org/10.1098/rspa.1991.0150

Parry, D. J., & Walker, a G. (1995). Hopkinson bar pulse smoothing. *Measurement Science and Technology*, *6*, 443–446.

Su, H., Xu, J., & Ren, W. (2014). Mechanical properties of ceramic fiber-reinforced concrete under quasi-static and dynamic compression. *Materials & Design*, *57*, 426–434. https://doi.org/10.1016/j.matdes.2013.12.061

Subhash, G., & Ravichandran, G. (2000). Split-Hopkinson Pressure Bar Testing of Ceramics. *ASM Handbook, Volume 8: Mechanical Testing and Evaluation*, *8*, 497–504. https://doi.org/10.1361/asmhba0003299

Tai, Y.-S., & Tang, C.-C. (2006). Numerical simulation: The dynamic behavior of reinforced concrete plates under normal impact. *Theoretical and Applied Fracture Mechanics*, *45*(2). https://doi.org/10.1016/j.tafmec.2006.02.007

Tai, Y. S. (2009). Flat ended projectile penetrating ultra-high strength concrete plate target. *Theoretical and Applied Fracture Mechanics*, *51*(2), 117–128. https://doi.org/10.1016/j.tafmec.2009.04.005

Tang, T., Malvern, L. E., & Jenkins, D. A. (1992). Rate Effects Uniaxial Dynamic Compression of Concrete. *ASCE Journal of Engineering Mechanics*, *118*(1), 108–124. https://doi.org/10.1061/(ASCE)0733-9399(1992)118:1(108)

Tedesco, J. W., & Ross, C. A. (1998). Strain-Rate Dependent Constitutive Equations for Concrete. *Journal of Pressure Vessel Technology*, *120*, 398–405.

Xia, K. (2013). Status of characterization of strength and fracture properties of rocks under dynamic loading. *FRAGBLAST 10 - International Symposium on Rock Fragmentation by Blasting*, 41–51.

Yang, H., Song, H., & Zhang, S. (2015). Experimental investigation of the behavior of aramid fiber reinforced polymer confined concrete subjected to high strain-rate compression. *Construction and Building Materials*, *95*, 143–151. https://doi.org/10.1016/j.conbuildmat.2015.07.084

Zhao, P., & Lok, T. S. (2005). Adaptation of impactor for the split Hopkinson pressure bar in characterizing concrete at medium strain rate. *Structural Engineering and Mechanics*, *19*(6), 603–618.

Zheng, D., & Li, Q. (2004). An explanation for rate effect of concrete strength based on fracture toughness including free water viscosity. *Engineering Fracture Mechanics*, *71*(16–17), 2319–2327. https://doi.org/10.1016/j.engfracmech.2004.01.012

Zheng, S., Haussler-Combe, U., & Eibl, J. (1999). New Approach to strain rate sensitivity of concrete in compression. *Journal of Engineering Mechanics*, *125*(12), 1403–1410.